Effect of powder characteristics and layer thickness on the densification of Selective Laser Melted CoCrMo

SJ Papworth

orcid.org/0000-0002-3038-3431

Dissertation accepted in fulfilment of the requirements for the degree *Master of Engineering in Mechanical Engineering* at the North-West University

Supervisor:	Dr A Bayode
Co-supervisor:	Mr CP KLoppers
Assistant-supervisor:	Ms J Fourie

Graduation:	June 2023
Student number:	28718089

ACKNOWLEDGEMENTS

Firstly, I would like to thank the Collaborative Program for Additive Manufacturing (CPAM) and the National Research Foundation (NRF) for funding this study and providing a bursary. A special thanks to Mr. CP Kloppers, Dr. Abey Bayode, and Dr. Jaundrie Fourie for their unwavering support and guidance throughout the study. The input from Mr. Kloppers was invaluable; thank you for aiding in sample preparation and helping overcome challenges faced throughout the study. I will always appreciate your open-door policy to bounce research ideas about and for providing me with research direction. I would also like to thank the NWU for providing the resources and facilities to conduct the research, I look forward to the future studies published through the research group.

To my parents, thank you for providing me with the opportunity to study my passion. Without your support, understanding, and encouragement, this study would not have been possible. I will always be grateful for your unconditional care and love.

Disclaimer: This work is based on the research supported in part by the National Research Foundation of South Africa (Grant number 141533). Opinions, findings, conclusions, and recommendations expressed in this dissertation is that of the author.

ABSTRACT

Selective laser melting (SLM) is a metal additive manufacturing (AM) process that fabricates parts according to a CAD design in a layer-by-layer fashion by melting metal powder. There are a vast number of powder-related parameters in SLM, including the powder size, shape, distribution, and layer thickness. These parameters have a direct impact on the laser-powder interaction during melting and can have an influence on the final part quality. The aim of the study is to investigate the effect of extrinsic powder characteristics and layer thickness on selective laser melted CoCrMo parts. The research investigates the effect on final part density by firstly, using two CoCrMo powders with different particle size distributions, secondly, varying layer thickness with constant laser energy densities and lastly, measuring the consistency of part density at different locations on the build plate.

In this study, the laser processing parameters were kept constant (laser power (LP), hatch distance (HD), and scan speed (SS)) whilst two layer thicknesses were used. The two CoCrMo powders used were comprehensively studied in terms of their extrinsic powder characteristics and their influence on final part density. The powder was measured across the build plate at various locations for each build to investigate the consistency of the powder across the build plate. The powder consistency was evaluated through powder bed density (PBD) samples at each build location, and from the samples, the particle packing efficiency and extrinsic powder characteristics were identified. The part density consistency was investigated through positioning cuboid samples at various locations on the build plate. From determining the consistency of the powder characteristics and part density across the entire build plate, correlations between the two results were identified.

The results show that there is a difference in final part density when different powder grades were used at consistent SLM processing parameters. Potential reasons for the effect of build location on part density were discussed. The powder with a wider particle size distribution due to having more fine particles showed an increased packing efficiency. It was found that the finer powder deposited a more consistent powder layer across the build plate, which led to a more consistent part density. Spatter was found to have an influence on the powder characteristics and part density at various build locations. When the layer thickness increased, the influence of the powder characteristics on the final part density was exaggerated, and an increase in porosity within the final parts was identified. The findings of this study highlight the importance of powder-related parameters in SLM on the final part density. A valuable understanding of how powder at specific locations on the build plate can influence the part density was established. Based on the findings it is recommended to investigate multiple test samples at various build locations to accurately determine the part quality per build.

KEYWORDS

Additive manufacturing, selective laser melting, Cobalt Chrome, powder characteristics, layer thickness, part density, powder bed density

TABLE OF CONTENTS

LIST OF TABLES

LIST OF FIGURES

NOMENCLATURE

AM	Additive Manufacturing
ASTM	American Society for Testing and Materials
CAD	Computer Aided Design
CoCrMo	Cobalt Chrome Molybdenum
D_{10}	Volume-based size which 10 % of the particle size distribution lies below
D_{50}	Volume-based size which 50 % of the particle size distribution lies below
D_{90}	Volume-based size which 90 % of the particle size distribution lies below
DMLS	Direct Metal Laser Sintering
EBM	Electron Beam Melting
EDM	Electrical Discharge Machining
HD	Hatching Distance
LP	Laser Power
LPBF	Laser-Powder Bed Fusion
LT	Layer Thickness
PBD	Powder Bed Density
PBF	Powder Bed Fusion
PSD	Particle Size Distribution
RSD	Relative Standard Deviation
SEM	Scanning Electron Microscope
SHS	Selective Heat Sintering
SLM	Selective Laser Melting
SLS	Selective Laser Sintering

SS	Scan Speed
t_{eff}	Effective Layer Thickness
UTS	Ultimate Tensile Strength
VED	Volumetric Energy Density
YS	Yield Strength

CHAPTER 1 - INTRODUCTION

1.1 Background

Metal Additive Manufacturing has gained popularity in both academia and industry. The ability of the technology to manufacture complex parts with shortened lead-times with less waste material has led to sectors such as the medical, aerospace, and automotive industries adopting the technology. These industries require parts that conform to strict quality standards, for example, meeting the mechanical strength properties required for the application. Studies have shown that part density has an influence on the mechanical properties of additively manufactured parts and selective laser melting (SLM) can produce parts with a relative density greater than 99 % [1], [2]. Porosities are defects that negatively impact the density; these defects can result from poor layer adhesion, partially melted powder, contaminated powder and uneven spreading of each layer [3]. Density measurements quantify defects such as porosity within manufactured SLM parts [4]–[6]. The shape, distribution, and amount of porosity present within a part directly influence mechanical properties such as ultimate tensile strength, elongation at break and hardness [7]. A reduction in relative density negatively impacts the mechanical properties of SLM parts. Therefore, controlling the density of parts allows for the control and prediction of mechanical properties. The ability to manage and predict density is attractive for applications of SLM parts, as the aerospace industry requires completely dense parts to avoid premature failure. On the other hand, in specific cases, the medical sector desires porous structures to allow for better integration with human bone [7].

The SLM powder performance has a complex relationship with the processing parameters, such as layer height, laser power, and scan speed. The final part properties, such as density, are a function of the complex relationship between powder and processing parameters. Within the SLM process, as depicted Figure 2-1, the interaction between the laser beam and powder generates a melt pool, with the scan speed determining the interaction time between the powder particles and the laser [8]. Ideally, the interaction time must be sufficient to produce a molten pool for a long enough period to allow the powder particles to reshape from their initial random packing and form a uniform single track. Therefore, the energy brought into the powder layer should be sufficient to completely melt the powder particles [1]. The powder bed density (PBD) in SLM is typically around 60 % of the material density and is affected by powder characteristics such as the particle size distribution (PSD), particle morphology and the coating system [1]. Hence, a higher PBD will reduce the number of voids between the particles in the powder deposited on the build platform, requiring less reshaping of the particles within the molten pool and resulting in uniform tracks [8], [9]. The powder characteristics play a significant role in the manufacturing and part performance of SLM, with a micro-macro relationship between powder characteristics and

the final part properties. However, the micro-macro relationship varies from powder to powder due to varying powder characteristics in PSD and morphology [1].

1.2 Problem statement

With AM technologies growing in popularity for end-use applications, a lack of confidence in final part quality and material behaviour has limited manufacturers from adopting the technology. The quality and repeatability of SLM components are hindered by the presence of porosity. An interaction between the powder characteristics and SLM processing parameters occurs across the entire build platform, and variations in this interaction influence the shape and distribution of the porosity. Therefore, the effect of extrinsic powder characteristics and layer thickness on the porosity formation and resulting part density in parts during the SLM process needs to be established.

1.3 Aim

This study investigates the effect of extrinsic powder characteristics and layer thickness on selective laser melted CoCrMo alloy parts.

1.4 Objectives

The objectives of this study are to:

1. Determine the effect of PSD and powder morphology on powder bed density and part density at various locations on the build platform.
2. Establish the effect of layer thickness on powder bed density and part density at various locations on the build platform.
3. Measure the consistency in relative part density across the build platform.

1.5 Delimitations

Intrinsic powder characteristics such as chemical composition was not considered during the study and only extrinsic powder characteristics were analysed. This is because the extrinsic characteristics were considered to have more of an effect on the densification of SLM parts as opposed to the intrinsic characteristics. Although it is well known that the process used to make the powder affects extrinsic powder characteristics, only gas atomised CoCrMo powders were examined due to their accessibility. The laser energy density (LED) was maintained constant at both layer thicknesses to emphasize the impact that the two powders' different extrinsic powder characteristics had on part densification. Since Archimedes' concept was frequently cited in the literature and was easily accessible for the number of density tests needed for the study, it was utilized to measure the relative part density. Due to the associated costs, relative part density was

not measured using micro CT scanning, and metallographic microscopy was not used to assess relative density because the technique by its very nature only takes into account the density on a planar level of the part, as opposed to Archimedes' principle, which takes the entire part into account.

1.6 Outline of the dissertation

The problem statement, aim, objectives and delimitations of this study are stated in Chapter 1 along with an introduction to AM. In Chapter 2, the literature on the impact of layer thickness and powder characteristics on the densification of selective laser melted parts is critically reviewed. The materials and methods used to accomplish the research's aims and objectives are described in Chapter 3. Details about the CoCrMo powders, test specimen design, and printing parameters utilized to manufacture the test specimens are included. The findings on the extrinsic powder characteristics, resulting PBD, and final part density are presented in Chapter 4. Furthermore, the results are discussed with the two powders and two layer thicknesses compared to find correlations between the powder characteristics and part density. Finally, Chapter 5 brings the study to a close by outlining how the research addressed the problem statement and provides future recommendations.

CHAPTER 2 – LITERATURE REVIEW

2.1 Introduction

This chapter reviews the SLM process and powder feedstock. The effect of powder-related parameters on SLM components is discussed specifically on part density along with common sources of porosity.

2.2 Additive manufacturing

AM is an advanced manufacturing process that transforms three-dimensional (3D) computer-aided designs (CAD) into physical parts by building the geometry in a layer-by-layer fashion [10]. Therefore, the layer-by-layer manufacturing process made possible through AM allows for complex-shaped geometry manufacturing as single objects with minimal material wastage [11]. The ASTM International Committee F42 has standardized AM technologies into seven classes: vat photopolymerization, material jetting, binder jetting, material extrusion, sheet lamination, directed energy deposition, and powder bed fusion (PBF) [12]. For this study, the focus is on PBF, and Dev Singh et al. [13] classified PBF into five types: selective laser sintering (SLS), direct metal laser sintering (DMLS), selective heat sintering (SHS), electron beam melting (EBM), and selective laser melting (SLM). All PBF processes require thermal sources to induce fusion between the powder particles, a method to control powder fusion according to a prescribed contour at each layer, and a mechanism for smoothing and adding powder layers [14]. Materials available for AM are limited but are growing year by year with increased popularity and research.

Biomedical applications adopt the use of Cobalt Chrome (CoCr) alloys. According to Monroy et al. [15], CoCr alloys are the hardest biocompatible alloy and present good fatigue and tensile properties, thus making them highly suitable for biomedical applications. Dental applications utilise the alloy primarily for crowns and bridge structure restorations [16]; however, it has also been employed for prosthetic applications [15]. Traditional manufacturing of CoCr alloy components for biomedical applications is investment casting and forging. However, additive manufacturing is now gaining popularity in the manufacturing of customised biomedical implants [17].

2.3 Selective laser melting process

SLM, which forms part of the PBF class of AM, is the manufacturing process used in this study. SLM is used to manufacture metal components directly from metal powder by fusing successive layers of metal powder. The process can be illustrated in Figure 2-1:

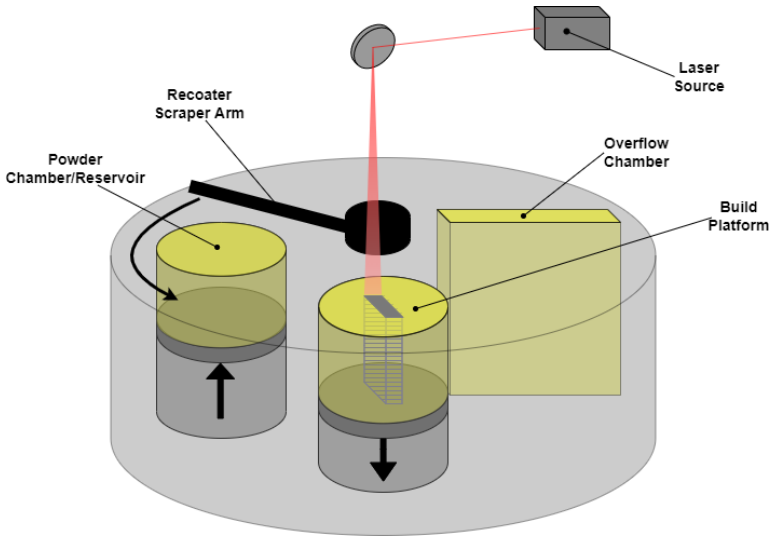

Figure 2-1: Schematic diagram of the SLM process

The following main steps can describe the SLM process: firstly, by spreading a layer of powder with the recoater scraper arm from the powder chamber across the build platform with the excess powder being deposited into the overflow chamber, secondly the powder is selectively laser melted by a laser according to a predefined pattern through a galvanometer and lastly, the build platform is lowered. These steps are repeated until the part is completed according to the sliced CAD file at predefined processing parameters. The SLM processing parameters are defined during the slicing of the CAD profile. The main processing parameters of SLM are illustrated in Figure 2-2:

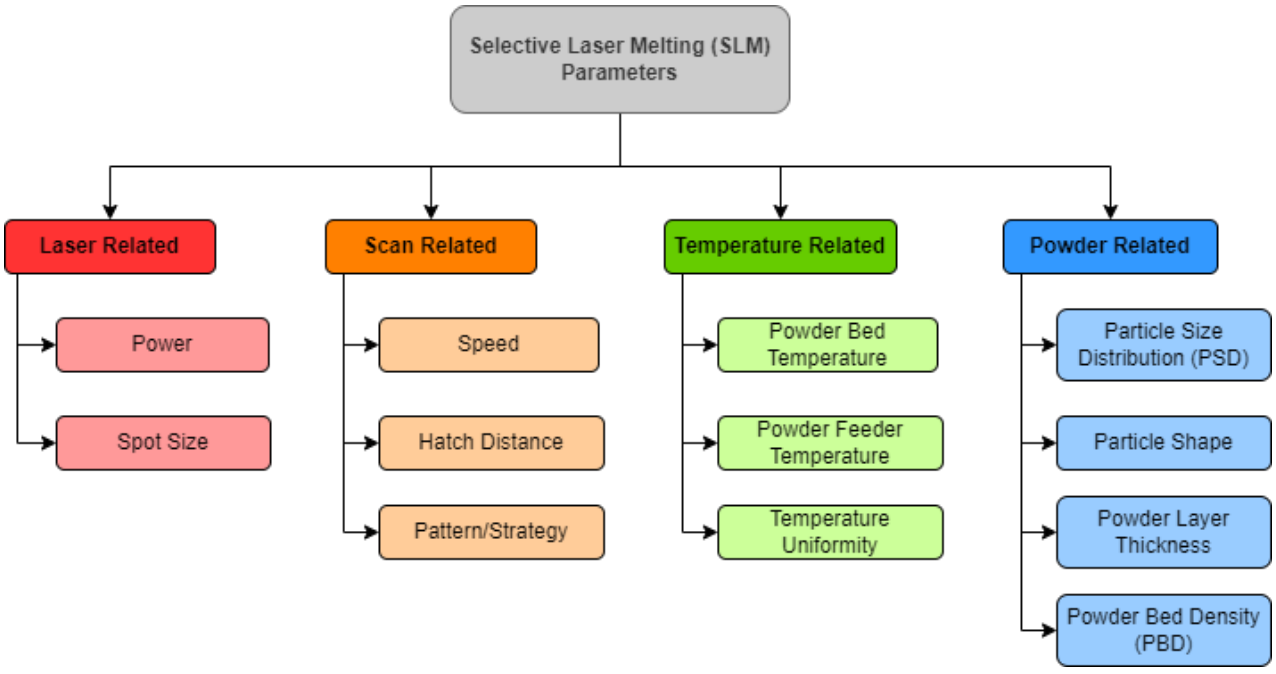

Figure 2-2: SLM laser, scan, temperature, and powder-related parameters. Adapted from Aboulkhair et al. [18]

The SLM process parameters are laser, scan, temperature, and powder-related. Laser and scan-related parameters work closely together as the laser melts the powder particles at the defined scan parameters. The powder-related parameters include the powder PSD, particle shape, powder layer thickness and PBD. The parameters illustrated in Figure 2-2 are discussed further in the following subsections.

2.3.1 Laser and scan related parameters

Laser power is the main processing parameter within SLM. Generally, when optimising process parameters for SLM, the other process parameters are typically tuned according to the laser power. A galvanometer directs the laser, and the laser beam is projected onto the powder bed to manufacture components [19]. The projected laser beam diameter is known as the spot size.

Scan speed is the processing parameter that controls the length of time the laser beam interacts with the powder bed. A reduction in scan speed allows the laser to interact with the powder for an extended period and can lead to extreme heating if low speeds and high laser powers are used. A poor melt pool will form, resulting in evaporation and material loss [7].

Hatch distance (HD) is the distance between the two adjacent melt pools, as seen in Figure 2-3. The hatch distance is described as a percentage overlap or as a physical dimension. When there is a small hatch distance, the overlapping of adjacent melt tracks is larger, and vice versa. If the hatch distance is too small, overheating can result in the evaporation of molten material; however, when a large hatch distance is employed, a lack-of-fusion porosity may be seen between adjacent melt tracks.

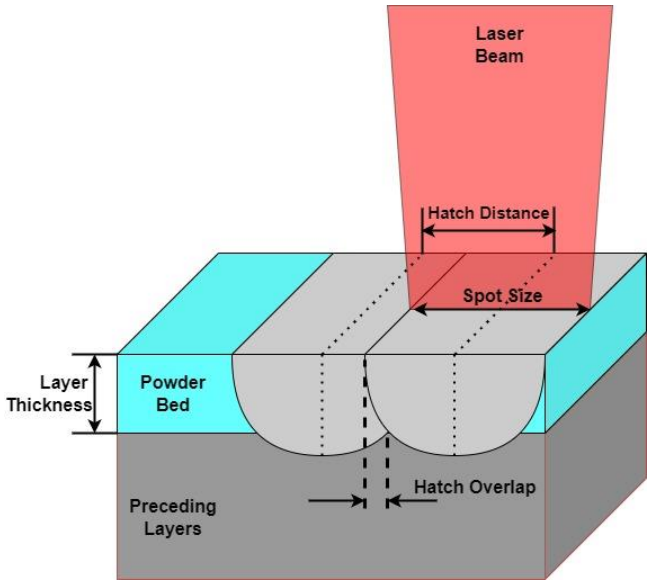

Figure 2-3: Schematic of SLM process parameters. Adapted from Yap et al. [20]

2.3.2 Powder related parameters

As illustrated in Figure 2-2, the powder related parameters include the PSD, particle shape, powder layer thickness and PBD. Particle shape and PSD are general parameters resulting from the powder manufacturing technique. The PBD and the thickness of the powder layer are powder-related parameters associated with the powder during the SLM manufacturing process.

2.3.2.1 Particle size distribution and shape

AM powders are described extrinsically by their morphological characteristics, including particle size, shape, and surface roughness. Understanding the powder characteristics provides information on the flowability and particle packing behaviour during the SLM manufacturing process. The shape of metal powders can be challenging to characterise since they can be highly irregular. Dimensionless ratios, known as shape factors, have been formulated to quantify particle shapes. Table 2-1 represents a few of the shape factors commonly used:

Table 2-1: Particle shape characterisation factors

Shape Factor	Equation	Reference
Circularity	$\frac{4\pi A}{P^2}$	[21]
Aspect ratio	$\frac{L_{minor}}{L_{major}}$	[22]
Elongation	$\log_2\left(\frac{a}{b}\right)$	[23]
Roundness	$\frac{r}{R}$	[24]

Notes:
A – Particle projected area
P – Particle perimeter
L_{major} – Major axis length of two points from projected area A.
L_{minor} – Minor axis length perpendicular to the major axis
a – Major axis length of Legendre ellipse of particle
b – Minor axis length of Legendre ellipse of particle perpendicular to a
r – Radius of the sharpest edge of particle
R – Mean radius of the particle

The shape of the powder particles is generally a result of the manufacturing process. Atomisation is one of the most common metal powder production methods. Sutton et al. [25] describe the atomisation process as a material that is liquefied and then extruded through an orifice where gas or water is imposed on the extrusion of molten metal to separate into tiny droplets that subsequently solidify whilst free falling. During the free fall, the molten droplets solidify into spherical-shaped particles to minimise surface tension. The first, water atomisation, uses water to separate the molten metal into droplets and is the most cost-effective technique. Water-atomised powders generally result in more irregularly shaped particles with satellites because the

high cooling rate does not allow enough time for particles to shape into spheres from the surface tension forces imposed during free fall. For gas atomised powders, the inert gas used to separate the molten metal allows for more time during free fall for the surface tension forces to shape particles with higher sphericity. Both water and gas atomisation processes produce powders with satellites and a wide PSD. Plasma atomisation may be employed to produce powders with minimal satellites and a narrower PSD. Due to plasma atomisation being costly, water and gas atomisation techniques are used to produce AM powders.

Most commercial powders used in SLM represent a *Gaussian* distribution [26]. The removal and addition of powder particles affects the distribution curve and results in different distribution curves, as illustrated in Figure 2-4.

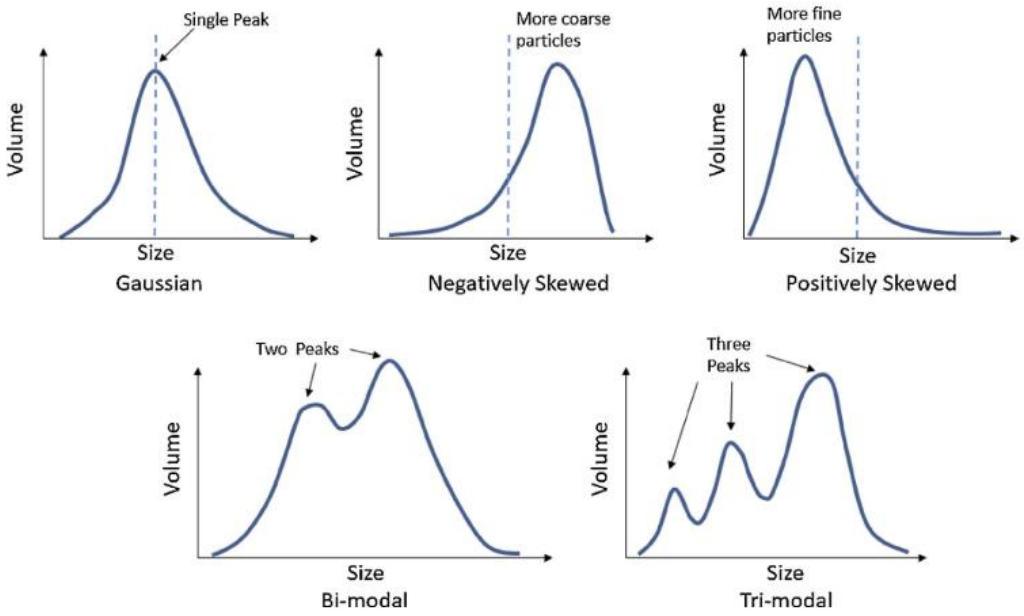

Figure 2-4: Variations of particle size distributions [26]

The particle size distribution curve can provide qualitative indications of powder behaviour. Therefore, techniques such as laser diffraction, sieving, and image analysis are available to characterise the powder's size and distribution. PSD is generally identified by the volume content in terms of size gauges (D_{10}, D_{50}, and D_{90}) [26]. The D_x indicates that X % of the powder sample is less than the D_x particle size. For example, if D_{90} = 40 µm, then 90 % of the powder sample is less than 40 µm.

2.3.2.2 Powder bed density

The deposition of a new powder layer in SLM is essential; therefore, it is imperative to understand the flowability and packing density of the powder since a powder layer consists of multiple powder particles packed close to each other. The PBD is related to the packing efficiency of the powder particles during the SLM process. The PSD and particle shape influence the packing efficiency

and, therefore, the PBD [27]. One way of understanding how particles pack and flow is to determine the flowability of the powder. Multiple methods are used to understand the flowability and physical properties of metal powders. An example is using a Hall funnel meter to determine the flowability of the powder. This method measures flowability by determining the time it takes for a fixed powder mass to flow through a funnel. Gravity is the driving force behind this method. A recoater arm deposits the powder layer during the SLM process. It is not mainly influenced by gravity but rather by the shear forces induced during the recoating process. Other methods to determine the powder packing density are by measuring the apparent and tapped density. However, these powder densities do not accurately reflect the density of the powder deposited during the SLM process.

Jacob et al. [28] developed an *in situ* method to measure the PBD consisting of multiple layers deposited on a PBF machine build plate to build an AM part. The main idea behind the approach is to capture the metal powder spread across the build plate within an enclosure during the PBF process. The enclosure design ensures powder within the specimens cavity is protected during post-machining against climate conditions until the powder density is measured. It also allows specimens to be placed at various positions within the build plate to measure the consistency of the powder bed conditions. An uncertainty analysis associated with the measurement method was also performed, showing that the measurement fluid's most significant contributor to measurement uncertainty was the surface tension effects. The surface tension was reduced by using reverse osmosis (RO) water to fill the cavity, resulting in fewer air bubbles and a flatter meniscus. Conservative estimations of surface tension effects were made, and it was concluded that the PBD enclosure specimen was robust and a reliable *in situ* method to determine the PBD of a PBF machine build.

The powder shape, size, distribution and spreading mechanism governs this PBD. The PBD typically ranges between 50 % - 60 % for most available metal powders in SLM. In comparison, ceramic powders that are irregularly shaped, result in PBDs as low as 30 %. In the case of melting the powders, a higher PBD improves the bed thermal conductivity [14].

2.3.2.3 Powder layer thickness

Layer thickness (LT) in SLM is the distance between two successive melted layers. It is measured along the vertical axis (z-axis) of the part being manufactured. The layer thickness should be selected according to the PSD and the other processing parameters mentioned above. In SLM, one of the significant steps is spreading/depositing a layer of powder with a recoater arm across the build platform. A suitable layer thickness allows all particle sizes to be deposited uniformly

onto the build platform without agglomeration or scraping of large particles. A thick layer deposits all particle sizes onto the build platform; however, this could produce larger voids between particles, potentially leading to a lack-of-fusion porosity. As the laser beam interacts with the powder layer, the laser selectively melts solid metal particles with other molten particles to form the melt pool. The part forms as each successive melt pool solidifies layer by layer. The interaction between the solidified layer and the new deposited thin powder layer is essential to understand, as the SLM process is highly dependent on the interaction between the energy source and the powder particles deposited as a thin layer.

Metal powders may be ordered at varying PSD ranges from manufacturers. Typically, the set layer thickness should consider the upper threshold of the PSD ranges. When particles deposit onto the build plate at a fixed layer thickness, only particles that fall within the layer thickness height will deposit, whilst larger particles will scrape across the build area. Therefore, the layer thickness is a limiting factor when it comes to the upper threshold of PSD ranges [25]. Abd-Elghany et al. [29] investigated the effect of varying layer thickness in manufacturing SLM low-cost 304L powder and showed the relationship between layer thickness and the particles deposited on the build plate as shown in Figure 2-5. The results reported decreased part density, strength, and ductility as the layer thickness increased. This was due to the poor powder layer density due to an increasingly larger particle volume deposited in the powder layer and insufficient energy to fully melt the particles. The same results were found by Zhang et al., where an increased layer thickness resulted in decreased part density and fatigue life [30].

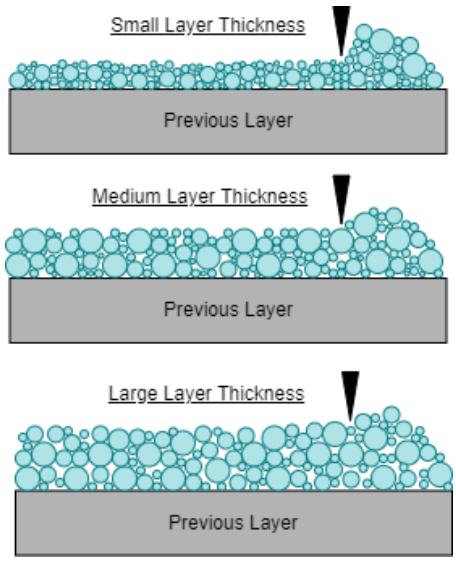

Figure 2-5: Effect of layer thickness on powder layer density. Adapted from Abd-Elghany et al. [29]

During the recoating process, the recoater arm deposits a fixed volume of powder onto the build platform to fill the gap between the previously solidified layer and the recoater as it rotates around. Since the solidification process caused the top layer of the powder to shrink or contract to a

greater relative density, the real powder layer thickness is greater than the incremental step made by the SLM machine when the build plate lowers. This real powder layer thickness is referred to as the effective layer thickness as shown in Figure 2-6:

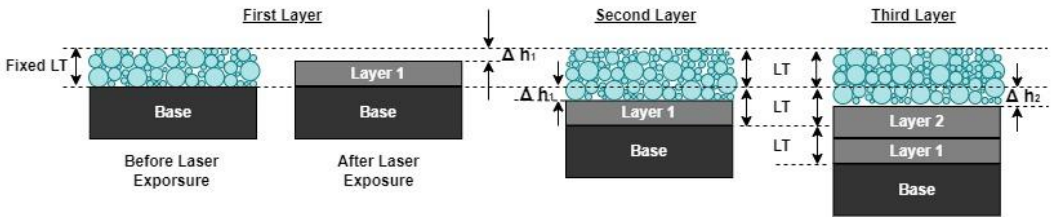

Figure 2-6: Illustration of effective layer thickness. Adapted from Wischeropp et al. [31]

Effective layer thickness is determined by calculating the shrinkage in the vertical direction during the solidification process [1]. The shrinkage is proportional to the powder layer density with respect to the manufactured part density. Jacob et al. [32] explain how the effective layer thickness is calculated through the following example, if the powder layer density is 60 % of the part density, for a 20 µm thick powder layer, the height of the shrinkage would be 8 µm. Therefore, the effective layer thickness for the successive layer will be 28 µm, assuming the powder layer density is approximately the same as the PBD. The following equation shows how the effective layer thickness is calculated after a certain amount of powder layers (*n*):

$$t_{eff\,(n)} = LT + t_{eff\,(n-1)} * \left(\frac{PD-PBD}{100}\right) \quad \text{Equation 2-1}$$

Where,

- $t_{eff\,(n)}$ is the effective layer thickness at *n* number of layers.
- LT is the incremental step predefined in the process parameters as the nominal layer thickness.
- PD is the relative part density of the manufactured AM part.
- PBD is the measured powder bed density.

Spierings et al. [1] calculated the effective layer thickness for selective laser melted SS316L components at varying layer thicknesses. Figure 2-7 shows the effective powder layer thickness development for scanned layer thicknesses of 30 µm and 45 µm at various powder layer densities. It can be seen that after building multiple layers, the real layer thickness of powder deposited stabilises.

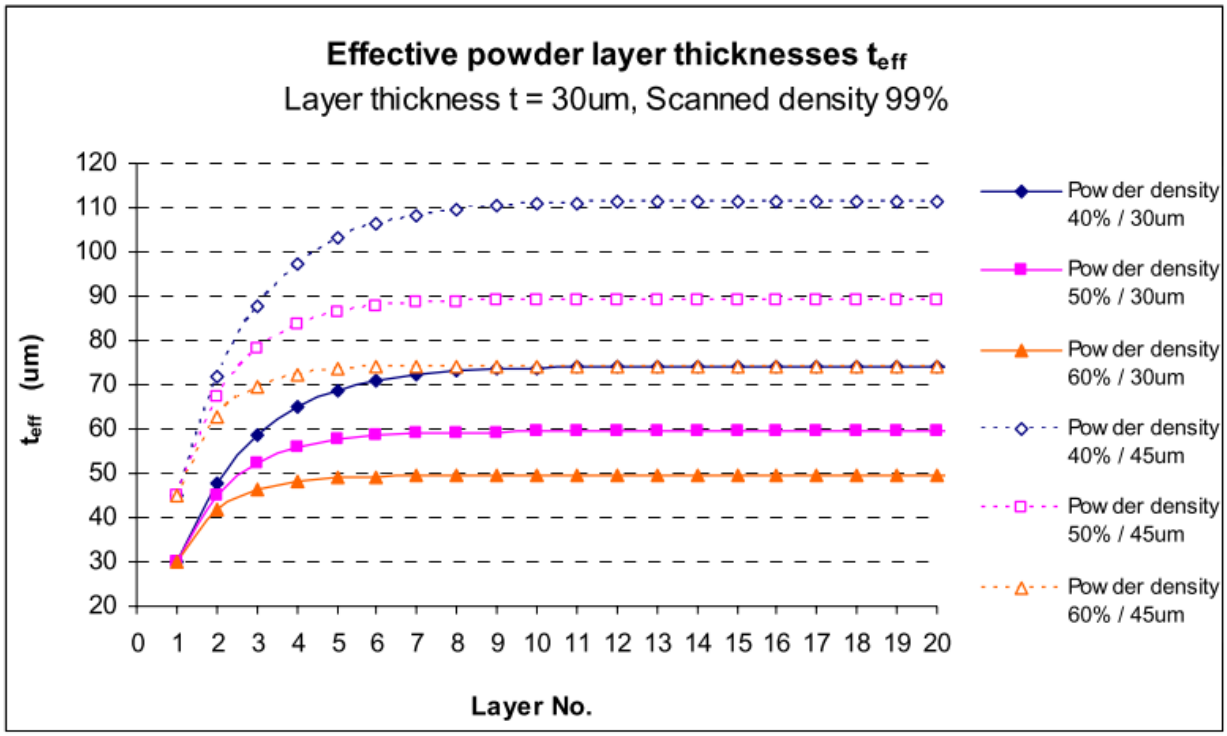

Figure 2-7: Effective powder layer thickness for scanned LT of 30um and 45um and various powder layer thicknesses developed by Spierings et al. [1]

2.4 Porosity of SLM components

Depending on the process parameters, selective laser melting is known to produce components with some degree of internal porosity [33]. Therefore, the most economical way to investigate and gather information on a material's mechanical parameters is to measure the density of the manufactured components. Changes in the part density affect the part's mechanical properties [34]. Therefore, the SLM processing parameters are usually optimised to minimize porosity to achieve the best possible mechanical properties of the specific material being used to manufacture components.

There are several ways to measure the density of a part, both destructive and non-destructive methods. The non-destructive methods are the Archimedes method, pycnometry and X-ray scanning or neutron imaging. The destructive method of cross-sectioning components and analysing the micrographs can also measure the relative density. However, this method is limited to the magnification and the selection of the cross-section to be analysed.

Spierings et al. [33] compared the different density measurement techniques on stainless steel 316L components manufactured by SLM. Based on the investigations, it was proposed that the Archimedes method be used to analyse relative part density since it is very easy to use, fast and economical. The following figure compares the three different analysis methods:

Table 2-2: Comparison of three different density measurement techniques by Spierings et al. [33]

	Archimedes method	Microscopy	Scanning
Non - destructive testing	●	◑	●
Geometrical dependency	◕	◑	●
Labour work/costs	●	◑	○
Repeat accuracy at high density level	●	◕	◑
Repeat accuracy at low density level	◑	◔	◑
Complexity of the procedure	◕	◑	◔
Accuracy of measurement	◕	◑	◑
Persuasibility of the result	◕	◔	◑ → choice of resolution
Usability for any geometry	●	◕	◕
Usability for any part size	●	◑	◔

Notes: ● fulfilled, good; ○ not fulfilled, bad

Since porosity influences mechanical properties, it is imperative to understand the porosity present in components. The shape and distribution of porosity play an essential role in understanding the cause of porosity. Strictly speaking, Sola et al. [35] describe pores as having a spherical shape, whereas voids are empty objects with irregular, non-spherical shapes. However, in literature, this distinction is rarely utilised. Therefore, the term “pore” can be generalised to small cavities formed within a single layer, between adjacent layers or on the external surface of a manufactured part. Sola et al. [35] reviewed porosity found in powder bed fusion components and characterized three different types:

1. *Microstructural pores:* unintentionally formed defects and residual voids in the microstructure of manufactured components. These pores should be minimized or avoided to achieve AM components' consistency and limit their adverse effects on mechanical properties.
2. *Functional pores:* interconnected pores that are open and generally caused by debinding. These pores are alleviated through HIP on infiltration with low-melting metals or polymers to obtain fully dense composite components.
3. *Structural pores:* Porosity that is intentional and arbitrarily introduced for specific purposes. This intentional porosity can be found in biomedical scaffolds to improve tissue growth.

Zhang et al. [36] reviewed defects and pores found in SLM and classified them into three groups namely: (a) porosities, which are generally spherical in shape and less than 100 µm in size; (b) melting related defects, which are irregular in shape and (c) cracks, which are a consequence of rapid cooling due to sharp thermal gradients and thermal stresses. Typical pores found in SLM can be seen in Figure 2-8.

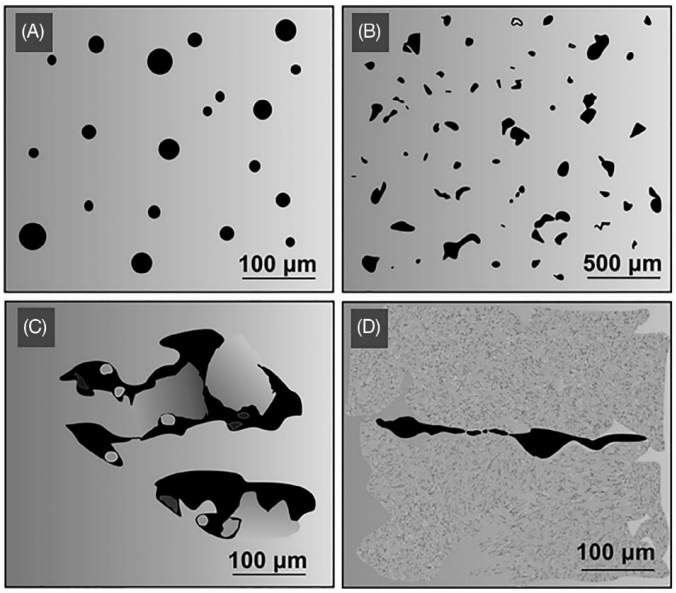

Figure 2-8: Types of pores found in SLM components: (A) entrapped gas porosity; (B) incomplete melting-induced porosity; (C) lack of fusion with unmelted particles and (D) cracks. [35]

From a technological point of view, defects such as porosity can be classified based on their origin, this helps to understand and mitigate the issue. Table 2-3 shows several causes and solutions in literature for porosity in PBF components.

Table 2-3: Common sources of porosity and potential solutions proposed in literature [35]

Source of Porosity	Detected Porosity	Solution	Literature		
			Material	Technique	Ref
Feedstock-related pores					
Pores entrapped in feedstock powder	Spherical or near-spherical pores. Small size of generally a few microns. Likely to grow larger during processing	Utilise high-quality powder feedstock. Hot isostatic pressing (HIP) of feedstock does not eliminate porosity but reduces the amount present.	AlSi10Mg	SLM	[36]
			316L	L-PBF	[37]
			316L	L-PBF	[38]
			Ti-6Al-4V	SLM	[39]
			CoCr	DMLS	[40]
			304L	L-PBF	[38]
The reaction between surface moisture and powder, typically with Aluminium powders	Pores that are spherical and typically smaller than 5 to 6 µm	External thermal pretreatment or internal laser pretreatment of powder	AlSi10Mg	SLM	[36]
			A357	SLM	[41]
			A357	SLM	[42]
Powder packing/PBD-related pores					
Voids present between powder particles that remain	Pores that are spherical and typically smaller than 5 to 6 µm	Better packing efficiency of powder particles, influenced by	Ti-6Al-4V	SLM	[43]
			Ti-6Al-4V	SLM	[44]
			Ti-6Al-4V	SLM	[45]

entrapped within the highly dynamic melt pool		PSD and powder morphology. Smaller layer thickness. Increase hatch overlap to promote remelting	AlSi10Mg	SLM	[46]
Manufacturing-induced pores					
Lack of fusion/incomplete melting	Large and irregularly shaped porosity with unmelted particles inside	Increase energy input to promote melting of particles Reduce porosity through HIP	CoCr 316L AlSi10Mg A357 Ti-6Al-4V [39] [47]	DMLS L-PBF SLM SLM SLM SLM SLM SLM	[40] [37] [46] [42] [45] [46] [22] [19]
Lack of fusion porosity through large hatch distance and insufficient overlap between adjacent melt pool tracks	Pores that are aligned along the direction of the scan track (Generally a grid-like dispersion)	Optimize the hatch distance to ensure adequate overlapping of adjacent melt pool tracks	316L AlSi10Mg A357 Ti-6Al-4V	L-PBF SLM SLM SLM	[37] [18] [42] [48]
Keyhole porosity due to excessive energy input/density. The energy input exceeds the threshold value or heat accumulation at the start/endpoints of the scan melt pool tracks is excessive	Pores that are spherical and usually near the bottom of the scan track. Typically larger than 10 to 20 μm.	Decrease energy input/density. Vary contour scan to change the laser direction at the edge of the core scan. Apply a mitigation strategy through normalized enthalpy control. [55]	316L 316L 316L 316L AlSi10Mg AlSi10Mg A357 IN718 Ti-6Al-4V [54] Ti-6Al-4V Ti-6Al-4V	L-PBF L-PBF L-PBF L-PBF SLM SLM SLM SLM SLM SLM SLM L-PBF	[37] [49] [50] [18] [51] [42] [52] [47] [53] [34] [21] [49]
Balling-related pores due to high scan speeds	Pores that are large and elongated located at the interlayer zone	Optimize the processing parameters focusing on reducing the scan speed	Ti-6Al-4V Ti-6Al-4V [56]	SLM SLM SLM	[39] [43] [11]
Spatter of particles caused by excessive energy input and the recoating process removing the large particles resulting in	Large pit-shaped cavity/porosity	Reduce the energy input/density	Ti-6Al-4V	SLM	[54]

cavities within the powder layer					
Powder denudation-related pores	Pores that are orientated along the scanning direction and generally large and elongated	Optimize the processing parameters focusing on the scan speed	Ti-6Al-4V	SLM	[48]

2.5 Mechanisms of spatter generation in SLM

Spattering is a phenomenon that occurs in SLM; due to the complex dynamics and heat transfer theory of the molten pool, it is difficult to accurately define the principles of spattering [57]. If the spatter is not removed from the air within the build chamber, spatter particles can fall onto the powder bed. Spatter particles present in the powder bed could be remelted and become inclusions within an SLMed part potentially affecting the final properties, including the density, microstructure, and mechanical properties. Large spatter particles could affect the powder recoating process resulting in an uneven powder recoating surface. Wang et al. [57] categorises spatter into three types: type-I metallic jet, type-II droplet spatter and type-III powder spatter as shown in Figure 2-9:

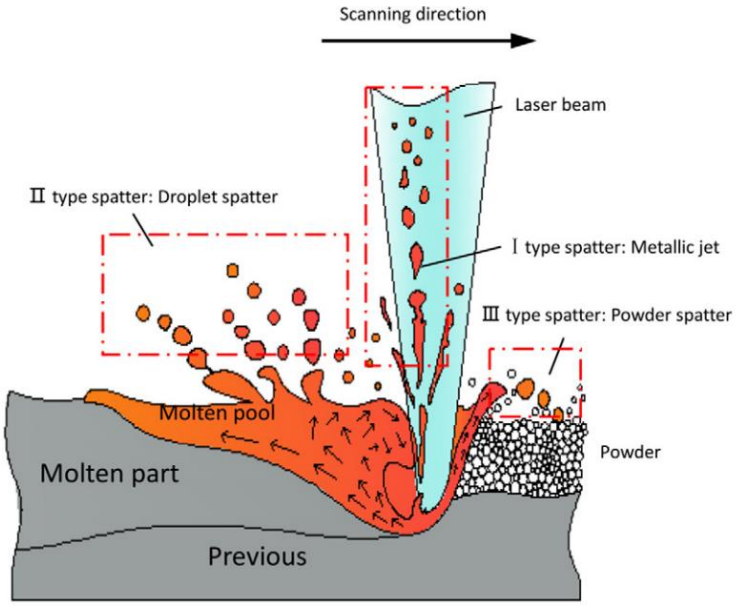

Figure 2-9: Formation mechanisms of spatter [57]

During the SLM process, when the laser is applied to the metal powders, the temperature within the light-energy region increases rapidly. During this rapid temperature increase, violent vaporisation of liquid metal occurs, and the gas trapped between the packed powder particles expands and causes recoil pressure. As seen in Figure 2-9, the surface of the molten pool deforms and becomes submerged under the vaporization pressure. The force of gravity causes

the molten pool of liquid metal at a high elevation to collapse instantly. The recoil pressure brought on by the highly rapid gas phase expansion produces a metal jet (Type-I spatter). Meanwhile, the marangoni effect causes the metal liquid to flow from the high-temperature bottom of the void/cavity to the low-temperature sidewall and edge at the back. Under recoil pressure, the low-viscidity metal liquid is jetted out. To reduce surface energy in the presence of surface tension, the jetted liquid metal stretches during flight and decomposes into small drops, resulting in droplet spatter (Type-II spatter). Furthermore, some liquid metal accumulates at the front of the optical spot during the scanning process. The blast wave squeezes the liquid metal, causing it to splash onto the front-end powder particles. At the same time, non-melted powder particles splash at the front of the molten pool and this generates irregular agglomerates of spatters adhered with many powder particles (Type-III spatter) [57]. Build-up of spatter particles on a powder bed can lead to powder recoating issues as shown in Figure 2-10:

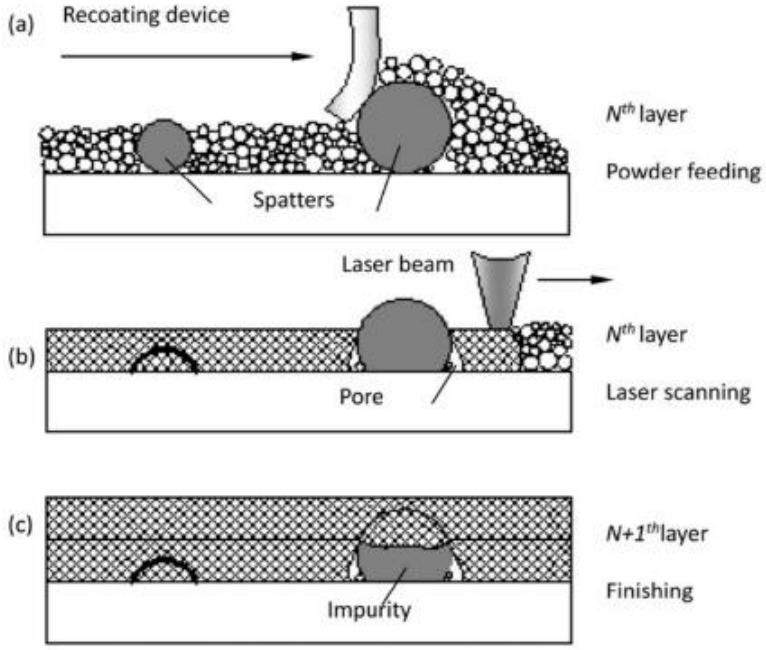

Figure 2-10: Effect of large spatter particles on powder recoating and internal defects [57]

If spatter particles are adhered to the surface of manufactured parts, new unmelted powder cannot efficiently distribute across the build plate causing larger voids in the powder bed as shown in Figure 2-10 b). Small spatter particles are completely melted by the laser; however, for spatter particles larger than the specified layer thickness, only some of them are melted by the laser. This impedes the laser from reaching regions near large spatters and additional gaps can be formed as seen in Figure 2-10 c).

Similar to spatter is the phenomenon called denudation. An overview of spatter and denudation is shown in Figure 2-11, Figure 2-12 showing how the denudation zone looks in actuality.

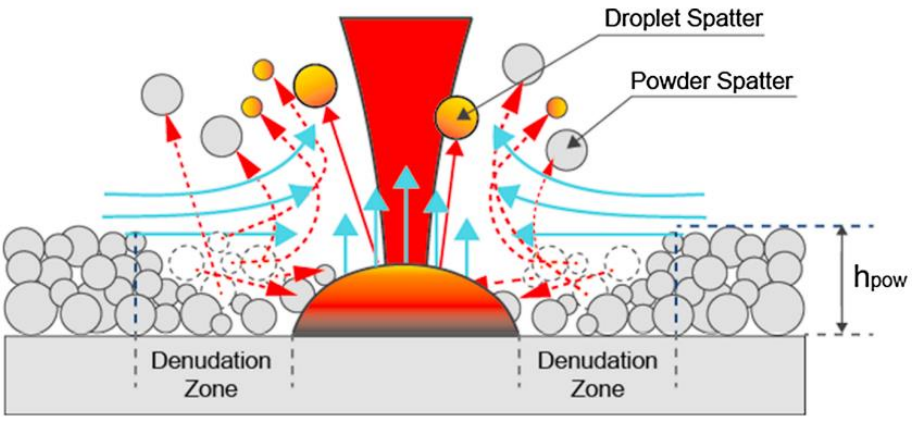

Figure 2-11: Overview of denudation zone and spatter [31]

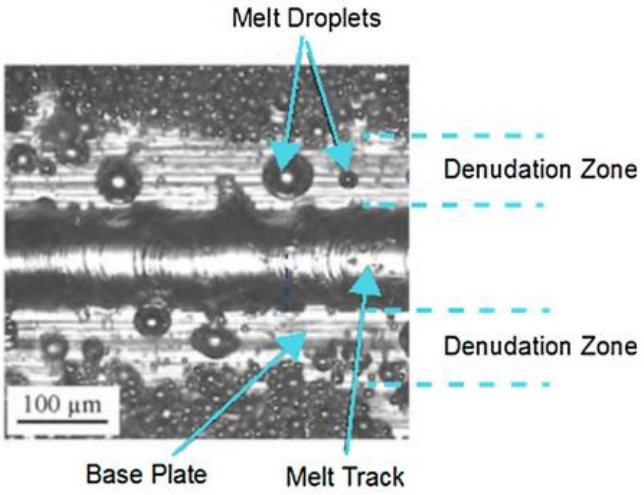

Figure 2-12: Denudation zone in SLM [31]

As shown in Figure 2-12, the denudation zone results in insufficient molten metal to fill the gap between the contour and hatching scan tracks. A lack of powder to absorb the energy results in remelting of the previous layer. This remelting could result in an unstable melt pool, causing keyhole porosity or lack of fusion porosity due to no powder to fill voids.

2.6 Effect of powder related parameters on SLM components

Studies have found that particle shape influences powders' flowability and, ultimately, effects the SLM process and the resulting components [25]. The flowability influences the SLM process as the powder deposits onto the build plate. Brika et al. [6] showed that more spherical particles increase flowability resulting in a higher particle packing efficiency and improved PBD. The influence of particle shape on SLM components has been reported in part density and mechanical properties. As reported by Brika et al. [6], increased PBD due to more spherical particles further increased the density of manufactured components. A representation of how the packing efficiency and shape of particles can influence melting is shown in Figure 2-13:

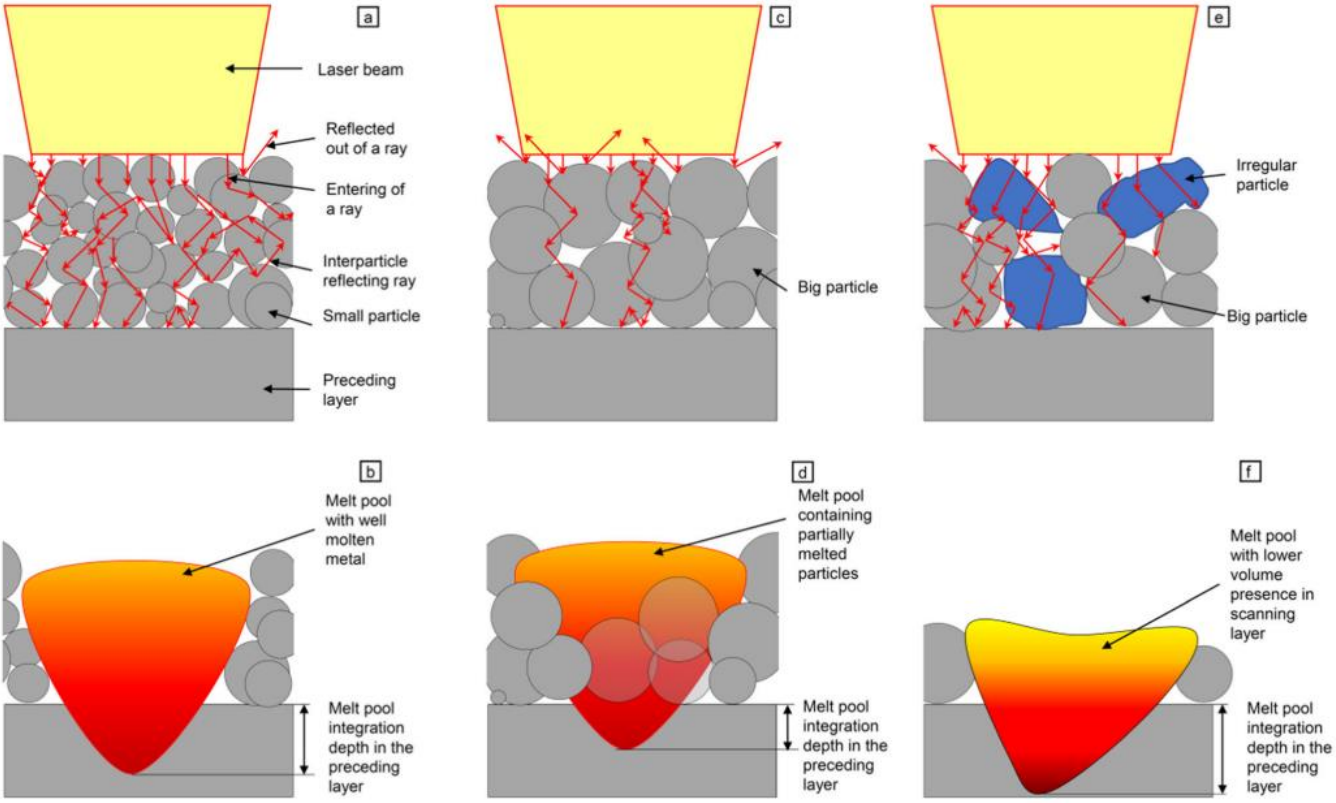

Figure 2-13: Schematic representation of meltpool formation dependent on packing efficiency and particle morphology [58]

Figure 2-13a) is a good representation of what occurs during a build with uniform compaction of the smaller more spherical powder particles, this allows for a steady penetration of the laser that results in an ideal meltpool shown in Figure 2-13 b). When larger particles are present in the powder, like when large spatter particles are deposited across the build plate, a higher proportion of the laser beam is reflected from the top surface of the layer, as can be seen in Figure 2-13 c). This phenomenon leads to insufficient absorption of thermal energy in the melt zone. Insufficient thermal energy can either not melt all the powder particles or creates a highly viscous melt pool. When a highly viscous melt pool is present, the viscous molten metal cannot flow into the unmelted zone to fill the pores, and large spatter particles easily obstruct this flow. In the case of large particles of irregular shapes, open spaces are created within the powder layer and reduces the packing efficiency, as seen in Figure 2-13 e). These large open spaces allow for a higher penetration depth of the laser and can lead to a rapid high heat build-up. The rapid high heat build-up causes a sudden expansion of the gas trapped between the particles, resulting in greater material spattering and the melt pool losing material.

Spierings et al. [33], [59] investigated the effects of PSD of metallic powders (SS 316L) on the density, mechanical properties and surface quality of SLM components. Two-layer thicknesses of 30 µm and 45 µm were investigated. The results showed that sufficient fine particles were required to fill the voids between larger particles; if insufficient fine particles were available to fill voids, a

lower scan speed was required to produce dense components. An increase in fine particles allows for easier melting and is beneficial for high part densities and surface quality. Furthermore, the mechanical strength can be expected to increase. In contrast, when larger particles are present, a higher elongation of components was found. As a result of the study, some guidelines were proposed for a suitable PSD selection guide:

- $\frac{T_{eff}}{D_{90}} \approx 1.5$ (Equation 2-2)

  This equation suggests that the effective powder layer thickness (T_{eff}) should be at least 50 % higher than the 90 % diameter of the particle size range. Thus, allowing for most of the particles to be deposited during the manufacturing process.

- $\frac{D_{90}}{D_{10}} \approx 5$ (Equation 2-3)

  This equation suggests that there be a suitable number of fine particles to larger/coarse particles to fill the voids between larger particles. When considering both guidelines, the D_{10} of the powder should be 7.5 times smaller than the T_{eff}.

Kuznetsov et al. [60] studied the effect of PSD on the mechanical properties of monolithic samples manufactured by laser-powder bed fusion (LPBF). The components were manufactured from 321 austenitic stainless steel, and the powder batch was divided into three different PSDs. The distributions were 0-20, 20-40, and 0-40 µm, respectively. The study found that hardness anisotropy was observed for the narrow powder distributions, whereas hardness anisotropy was absent in the wider powder distributions.

Riener et al. [61] investigated the influence of AlSi10Mg powder PSD and morphology on the resulting part density and mechanical properties of LPBF components. Three gas atomised powders and one plasma atomised powder were used during the study. Experiments were carried out at constant LPBF process parameters except for the hatch scanning speed. It was found that the manufacturing process of the powder had an influence on the results, with the powder morphology having the most significant impact on the part density and surface quality. The plasma atomised powder showed a minimal decrease in part density and mechanical properties due to higher scanning speeds. An increase in powder layer densities due to more spherical particles of plasma atomised powders resulted in higher part densities. When analysing the gas atomised powders, it was reported that smaller particles were more spherical with aspect ratios of close to 1. The Flowability of the powder was affected by both the particle shape and PSD, particularly the D_{10} value. A larger D_{10} and more spherical powders were shown to have an increased flowability. Moreover, the increased scanning speeds on the gas atomised powders resulted in decreasing part densities. Furthermore, finer PSDs consistently produced lower part densities. The varying scanning speeds and the resulting solidification rates affected the mechanical properties in terms

of yield strength (YS), ultimate tensile strength (UTS), and elongation. In terms of particle properties, the plasma atomised powder showed a slightly higher value for the UTS and elongation with a lower YS.

Bochuan et al. [34] investigated two sets of gas atomised metallic powders (SS 316L) from different manufacturers with similar chemical compositions and different PSDs. The study showed that powders with different PSDs behave differently during the SLM process, resulting in differences in powder bed distribution and built parts quality. Powder with a wide PSD increased PBD, relative part density and surface quality under low laser energy intensity. However, powders with a narrow PSD provided improved flowability resulting in components with higher UTS and hardness.

Hitzler et al. [62] evaluated the density and mechanical properties of two CoCr-based alloys manufactured by SLM. The relative density measured was 99.93 % for CoCrMo and 99.86 % for CoCrW, respectively. Relative densities were obtained using microsections, which generally result in higher percentages than the Archimedes method [33]. CoCrW represented better mechanical properties when compared to CoCrMo in terms of tensile strength, yield strength and modulus of elasticity. The author describes these differences in mechanical properties in terms of differences found in their respective microstructures.

Wang et al. [63] evaluated the mechanical properties of selective laser melted CoCrMo at various processing parameters. The yield strength and tensile strength were found to increase with an increase in the laser power and decrease with an increased scanning speed. The optimal SLM parameters were a laser power of 160 W, a scanning speed of 1100 mm/s and a hatch distance of 50 µm.

The effects of powder-related parameters are summarised in Table 2-4. The table focuses on the changes regarding powder-related parameters and the effect this has on the PBD, components density and mechanical properties.

Table 2-4: Influence of powder-related parameters on PBD, part density and mechanical properties

Property/Characteristic	Change	Effect	Reference
Powder Bed Density (PBD)	Widen the PSD through the addition of fine particles	Increase in PBD, apparent and tapped density	[64],[65],[66],[34]
	Narrow PSD	Increase in apparent and tapped density due to increase in flowability	[34]
	More spherical particles	An increase in particle packing efficiency and thus an increase in PBD	[6]
	Increase in fine particles	Decrease in PBD due to inter-particle friction	[6]
	A large proportion of particles with PSD D90 ≤ 10 µm	Negative effect on the usability of the powder and agglomerates on the build plate	[67]
	Bimodal PSD	Increase in PBD.	[8]
Component Density	Fine narrow PSD	Increase in part density with lower porosity	[60]
	Wide PSD with an increase in fine particles	Increase in part density	[34],[59]
	More spherical particles	Increase in part density due to increase in PBD	[6]
	Finer PSD	Produce consistently lower part density	[61]

	Increasing LT	Increase in Porosity, decreasing Part Density	[30]
Mechanical Properties	Fine narrow PSD	Increase in hardness anisotropy and overall lower hardness	[60]
	Wide PSD	Low hardness anisotropy	[60]
	Narrow PSD	Increase in ultimate tensile strength and hardness	[34]
	Larger, more coarse particles within PSD	Increase in elongation	[59]
	Highly spherical particles	Increase in UTS, Yield strength, elongation, and Youngs Modulus	[6],[61]
	Bimodal PSD	Decrease in surface roughness, increase in ultimate tensile strength, and yield strength. Decrease in elongation.	[8]
	Increasing LT	Decrease in fatigue life due to large pores developing cracks.	[30]
		Increase in elongation with a lower impact strength	[68]
	Smaller LT	Higher-strength properties and impact strength	[68]

2.7 Summary

In SLM manufacturing systems, powder related parameters are critical because they affect the final quality of manufactured components. Powders should be spherical and follow a suitable size distribution to facilitate a good packing efficiency that will contribute to manufacturing components with a high density and good mechanical properties. The powder should have a PSD that facilitates good flowability to ensure a consistent powder layer is deposited. An inconsistent powder layer can cause inconsistent melting and result in poor part density. Once a powder with an appropriate PSD, shape and flowability is established, the layer thickness should be selected based on the upper threshold of the PSD. If the layer thickness is too small, all powder particles above the layer thickness would not be deposited onto the build but rather be scraped away by the scraper arm. The scraping of particles across the build plate could result in decreased PBD and possible defects in the powder layer resulting in an inconsistent powder layer and thus poor melting. Therefore, the powder-related parameters depend on the SLM machine and the interaction between the powder and the processing parameters.

CHAPTER 3 – MATERIALS AND METHODS

The following chapter describes the methods and experimental setup used to evaluate the powder, the deposition of powder, and the density. Furthermore, the methods used for preparing and evaluating SLM manufactured components for porosity are described.

3.1 SLM feedstock materials

Two gas atomized CoCrMo metal powders were used in this study. The first was supplied by Praxair Surface Technologies (CO-538-1), the second supplied by Deloro Wear Solutions (Stellite F75) as shown in Figure 3-1.

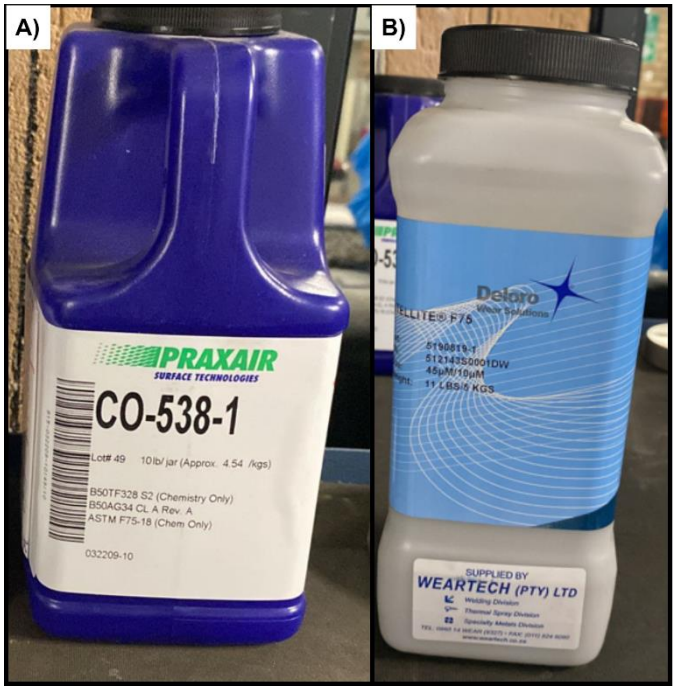

Figure 3-1: CoCrMo metal powders A) Praxair CO-538-1 and B) Deloro Stellite F75

3.1.1 Powder chemistry

According to ASTM F75, the chemical composition of CoCrMo powders used in AM should conform to the prescribed chemical composition. The two CoCrMo metal powders manufactured by different suppliers differed in terms of chemistry as reported by the suppliers. The ASTM F75 standards and the weight composition as reported by the suppliers are shown in Table 3-1:

Table 3-1: Weight % composition of powders as reported by the supplier vs ASTM F75 standards

		ASTM F75	Praxair CO-538-1	Deloro Stellite F75
Carbon	**C**	< 0,35	0,080	0,170
Sulphur	**S**	< 0,01	0,002	0,002
Cobalt	**Co**	Balance	Balance	Balance
Chromium	**Cr**	27,00 - 30,00	28,310	28,500
Iron	**Fe**	< 0,75	0,370	0,500
Manganese	**Mn**	< 1,00	0,140	0,300
Molybdenum	**Mo**	5,00 - 7,00	6,150	5,900
Nickel	**Ni**	< 0,50	0,170	0,200
Phosphorus	**P**	< 0,02	<0,005	0,000
Silicon	**Si**	< 1,00	0,250	0,500
Tungsten	**W**	< 0,20	0,060	0,000

3.1.2 Powder density

The true density of the powder was measured through helium pycnometry. The pycnometer determined the true density and volume by measuring the difference in pressure of helium within a controlled volume. The helium pycnometer used was the AccuPyc II 1340 Gas Pycnometer shown in Figure 3-2:

Figure 3-2: Helium Pycnometer - AccuPyc 1340 Pycnometer [69]

The helium pycnometry was performed in a 10 cm^3 controlled volume sample cell. A sample quantity of at least two-thirds of the controlled volume was used to ensure the accuracy of the results. The samples were initially dried at 120°C before the analysis. The dried samples were weighed using a digital balance accurate to 0.0001 mg and placed into the sample cell. A total of three cycles were performed, and the average of the three analysis results was taken as the true powder density.

3.1.3 Powder particle size distribution and morphology

Static automated imaging through a Malvern Morphologi G3 machine was used to measure the PSD and powder morphology. The dry powder particles were dispersed across a glass plate, and individual images of the particles were captured to determine the particle size, shape, and other physical properties. The automated imaging system consists of three main elements. The first is the sample presentation and dispersion element, where the powder particles were dispersed spatially across a flat glass surface. The second element is image capturing optics, where a CCD camera with appropriate magnification optics captured images of the individual particles. Lastly, the data analysis software recorded the range of morphological properties for each particle. From the static automated imaging process, morphological properties such as PSD, aspect ratio, circularity, elongation, and convexity were determined. The Malvern Morphologi G3 automated imaging machine used in this study is illustrated in Figure 3-3.

Figure 3-3: Static automated imaging – Malvern Morphologi G3 [70]

Static automated imaging simplified the complex 3D particles into 2D projections to make measurement and data analysis feasible. The particle shape parameters were calculated from the projection using simple geometrical calculations, which were also represented in Table 2-1. The complex particle projection is illustrated in Figure 3-4:

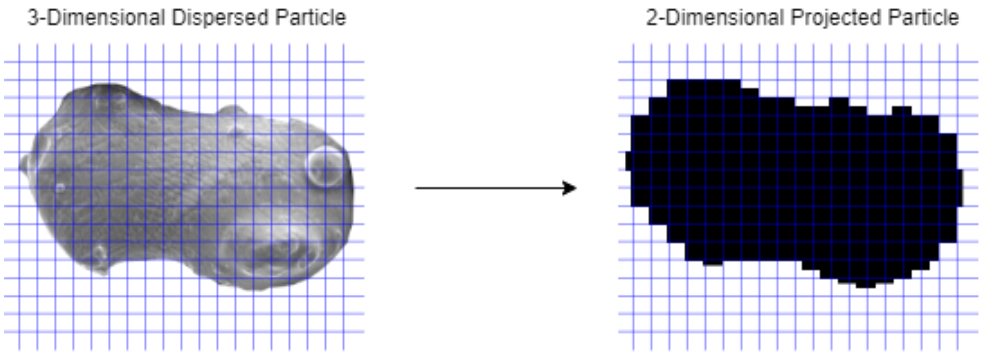

Figure 3-4: Conversion of a 3D particle to 2D binary projection in automated imaging

Images of the particle morphology were captured using a scanning electron microscope (SEM). The SEM images were captured using the FEI Quanta FEG 250 [71], shown in Figure 3-5.

Figure 3-5: FEI Quanta FEG 250 SEM Machine

3.2 Selective laser melting of samples

The SLM samples were manufactured using an OR LASER CREATOR SLM machine equipped with a 1070 nm Yb Fibre Laser with 250 W power. The different components of the SLM machine are represented in Figure 3-6:

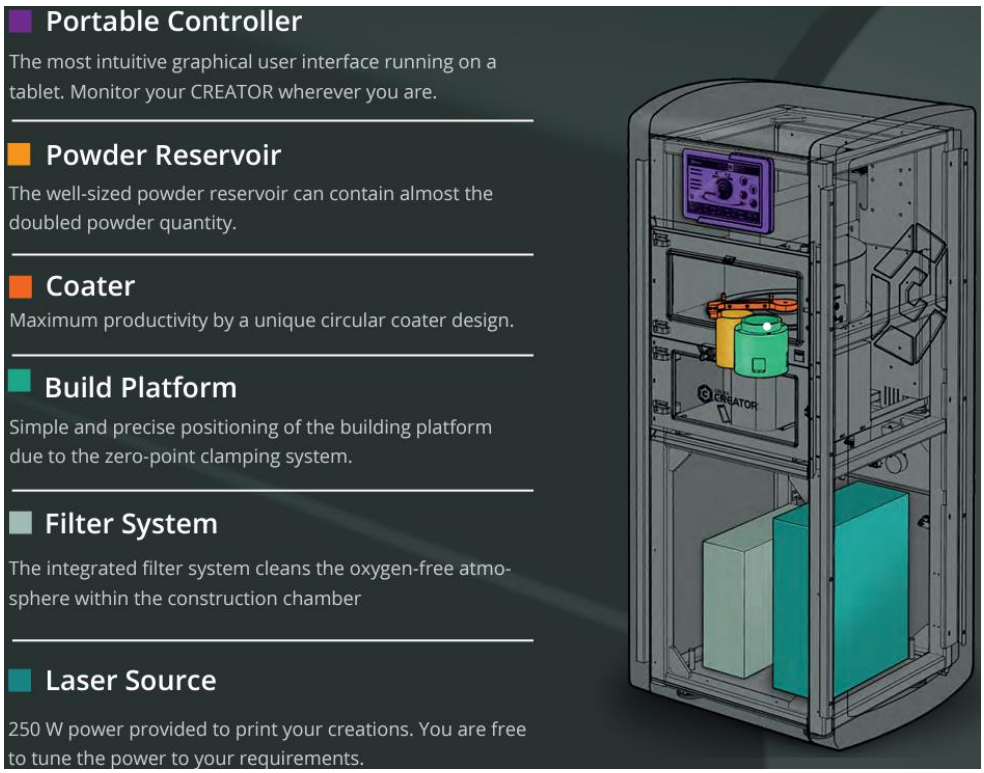

Figure 3-6: OR LASER CREATOR SLM machine architecture [72]

The system has a building volume of Ø100 mm x 100 mm and a powder reservoir volume of Ø110 mm x 200 mm. The powder layer was deposited by a rotational spreading arm (coater) from the powder reservoir, across the build platform and any excess powder was fed into the overflow chamber. Nitrogen was pumped into the system during manufacturing to purge the atmosphere within the build chamber to an oxygen content of below 0.1 %. A representation of the building chamber is shown in Figure 3-7:

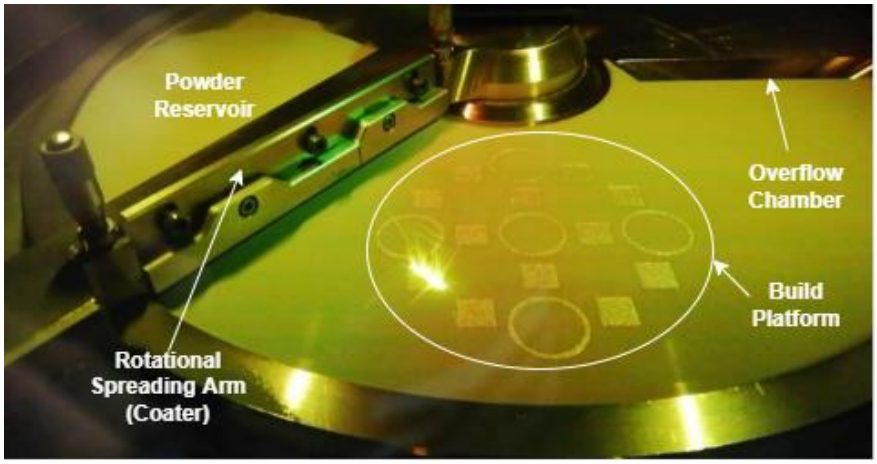

Figure 3-7: OR LASER CREATOR Build Chamber Architecture

All the samples were manufactured with the following printing parameters listed in Table 3-2.-The layer thickness was the only parameter that was changed, whilst the other parameters stayed constant. To summarise, two prints/builds per powder type and four prints in total were completed. The sample geometry and number of samples per print/build are outlined in sub-section 3.3. After manufacturing, the samples were sectioned from the build plate for characterization.

Table 3-2: SLM manufacturing parameters

SLM Manufacturing Parameters		
Layer Thickness	25 / 30	[µm]
Base Angle	45	[Deg]
Shift Angle	67	[Deg]
Contour Spot Size	40	[µm]
Contour Boundary Offset	40	[µm]
Contour Laser Power	140	[W]
Contour Mark Speed	250	[mm/s]
Hatch Spot Size	120	[µm]
Hatch Spot Overlap	50	[%]
Hatch Distance	60	[µm]
Hatch Boundary Offset	100	[µm]
Hatch Laser Power	125	[W]
Hatch Mark Speed	630	[mm/s]

The volumetric energy density (VED) was calculated using the following equation:

$$VED = \frac{LP}{HD * SS * LT}$$

Where, LP was the hatch laser power, HD, the hatch distance, SS, the hatch mark speed and LT, the respective layer thickness. Based on the listed manufacturing parameters, the VED at a layer thickness of 25 µm and 30 µm was 132.28 J/mm^3 and 110.23 J/mm^3, respectively.

3.3 Component density and powder bed density evaluation

The part density and PBD were evaluated by positioning twelve 10x10x11 mm cubes and five 6 cm^3 PBD capsules across the build plate, respectively. The positioning was done to measure the consistency in density, PBD and powder characteristics over the Ø100 mm build plate. This build plate configuration is illustrated in Figure 3-8 and Figure 3-9 shows the build plate configuration of manufactured test specimens within the OR LASER CREATOR build chamber during the removal process:

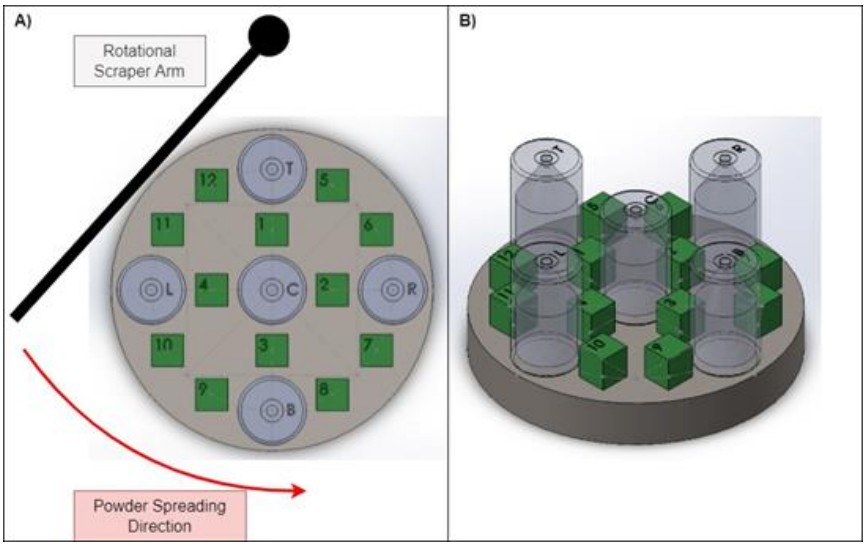

Figure 3-8: Build plate configuration

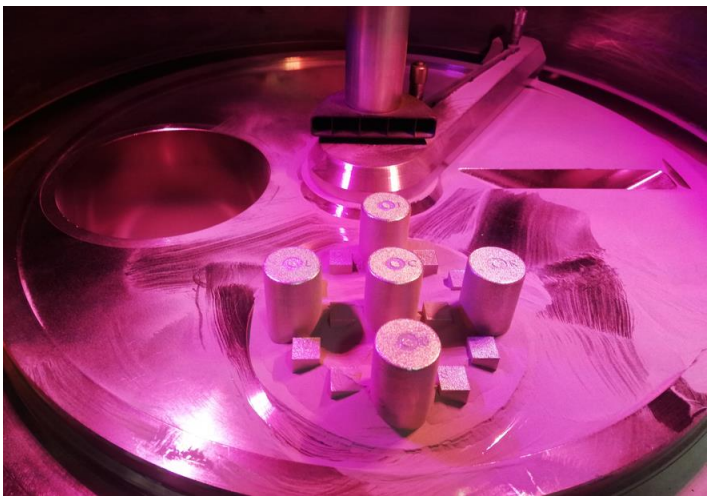

Figure 3-9: Removal of samples from SLM machine

The PBD specimen design was adapted from Jacob et al. [28] and was 35 mm tall, and had a combined nominal inner volume of 6 cm^3. The specimen design shown in Figure 3-10 allowed PBD to be measured and the captured powder to be analysed post-manufacturing for morphology and PSD changes.

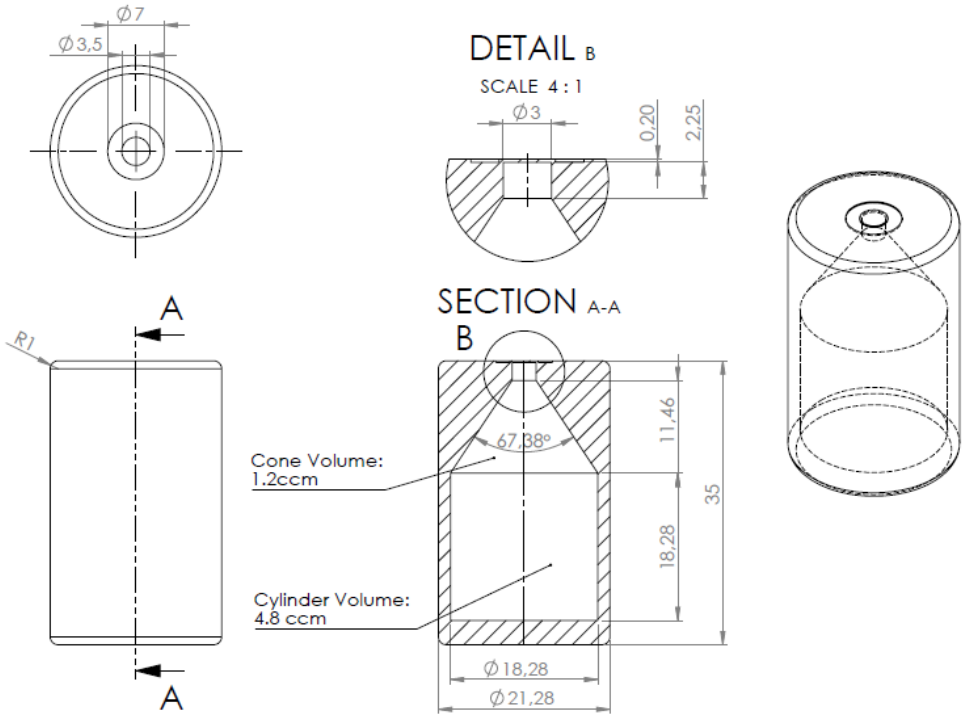

Figure 3-10: Design of PBD specimen (dimensions in millimetre except for volume in cubic centimetre (ccm))

After manufacturing, the samples were removed by wire-EDM at 1 mm from the build plate. This ensured the PBD specimens had a flat surface for when they were used in experiments, later discussed in section 3.5 below.

3.4 Density and porosity measurement

The relative density of the specimens was measured using the Archimedes principle, a non-destructive method [33]. A microscopic analysis of specimen cross-sections was used to identify porosity size and distribution.

3.4.1 Relative density of samples

The Archimedes principle was used to measure the relative density of cubic samples. The analytical balance used for the relative density measurements was the 250g Luna Analytical Balance equipped with a density measurement kit shown in Figure 3-11. The analytical balance has a readability of 0.0001g, which complies with ASTM B311-17 for acceptable balance readability for performing the Archimedes principle on specimens with a mass of less than 10g [73].

Figure 3-11: Luna Analytical Balance with equipped density apparatus

The experimental procedure for the Archimedes density measurements was followed according to the procedure laid out in ASTM B311-17 and can be summarised as follows:

1. The cubic test specimens were cleaned of any residue and placed in the same environment as the analytical balance and distilled water to allow for a uniform temperature when the weighing was performed.
2. Each specimen was weighed in air three times, and the mean values were expressed as the specimen mass in air.
3. Each specimen was suspended by the support basket and immersed in distilled water. The water level was at least 6 mm above any wire twists and the test specimen to minimise the effect of surface tension forces on the weighing.

4. The test specimens were weighed in distilled water three times, with the temperature of the water being measured to the nearest 0.1 °C to calculate the water density.
5. The density was calculated using equation 3-1:

$$\rho_{specimen} = \left(\frac{m_{air}}{m_{air} - m_{liquid}}\right) * \rho_{liquid} \qquad \text{(Equation 3-1)}$$

Where:

$\rho_{specimen}$ = Density of test specimen, g/cm3,
m_{air} = Mass of test specimen in air, g,
m_{Liquid} = Mass of test specimen immersed in liquid, g,
ρ_{liquid} = Density of distilled water at a specific temperature, g/cm^3

3.4.2 Porosity evaluation

The size and distribution of porosity within the cubic test specimens were analysed using cross-sections of the samples that were polished and viewed under an optical microscope. The cubic test specimens were sectioned parallel and perpendicular to the build direction as illustrated in Figure 3-12:

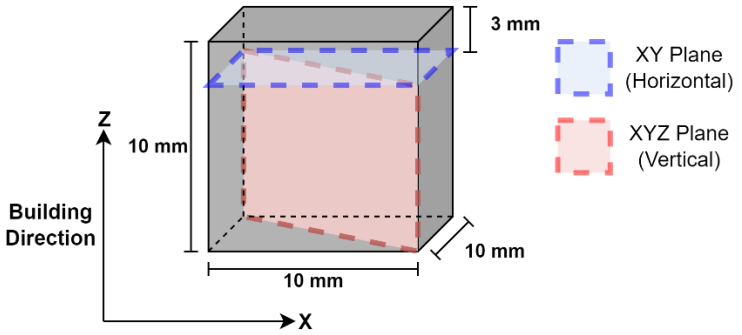

Figure 3-12: Cross-section of a cubic test specimen

The cubic specimens were cross-sectioned using a wire-EDM at 3 mm in height along the z-direction across the xy plane. The remaining specimen was sectioned diagonally across the xy-z plane. The remaining XY plane had a cross-sectional area of 100 mm^{2,} and the XYZ plane had a cross-sectional area of 99 mm^2. Once the specimens were successfully sectioned, they were hot-mounted in resin to allow for the metallographic procedure. The metallographic procedure was performed on a Struers Tegramin-20 as shown in Figure 3-13.

Figure 3-13: Struers Tegramin-20 for metallographic procedure

The metallographic process included grinding and polishing, and the used procedure was according to Akasel's surfaced hardened steel procedure [74]:

1. Plane grinding using Akasel Piatto 220 under water lubrication at a force of 35 N and 300 rpm until the surface is plane.
2. Fine grinding using Akasel Allegran 3 under 9 µm diamond-infused lubrication at a force of 35 N and 150 rpm for 2:30 minutes.
3. Polishing using Akasel Ramda under 3 µm diamond-infused lubrication at a force of 30 N and 150 rpm for 2:00 minutes.
4. Final polishing using Akasel Napal cloth under 1 µm diamond-infused lubrication at a force of 20 N and 150 rpm for 0:30 minutes.

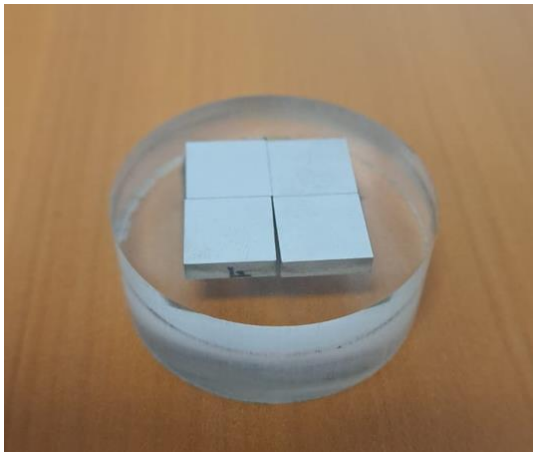

Figure 3-14: Hot-mounted final polished samples

3.5 Powder bed density measurement

The PBD specimens were measured according to the procedure determined by Jacob et al. [28]. Post-removal from the build plate, the specimens were weighed using the Luna analytical

balance, shown in Figure 3-11. The 0.2 mm thick lids of the specimens were opened by punching the hole using a chisel and hammer. The resulting opening used to drain the powder out of the sample is shown in Figure 3-15.

Figure 3-15: Opened hole of PBD specimen

Once the PBD specimen was opened, the powder inside was drained. The empty specimens were flushed with isopropanol to remove any remaining powder. After being flushed, the specimens were dried at 120°C for 30 minutes to remove any moisture and weighed. Thereafter, the actual inner volume of the specimen was determined because SLM printing parameters can cause deviations in the designed nominal volume. Therefore, the actual inner volume was measured using a method based on mass measurements of the empty PBD specimen and the specimen filled with distilled water of known density at a specific temperature. The temperature of the distilled water was measured using a digital multimeter accurate to 0.1 °C. The water-filled specimen was tapped gently to remove any bubbles trapped within the cavity and inspected for any water on the outer surface of the sample. The water-filled specimen was then weighed, and the volume of the inner cavity was calculated by equation (3-2):

$$\boldsymbol{V = \frac{m_w}{\rho_w}} \qquad \text{(Equation 3-2)}$$

Where,

V = Inner volume of the cavity, cm^3,

m_w = Mass of the water within the inner volume, g,

ρ_w = Density of the distilled water at a specified temperature, g/cm^3,

The powder mass can be determined from the difference between the mass of the full PBD specimen and the emptied specimen. Finally, from the measured inner volume and the mass of the powder, the PBD is calculated by equation (3-3):

$$\boldsymbol{PBD = \frac{m_p}{V}} \qquad \text{(Equation 3-3)}$$

CHAPTER 4 – EXPERIMENTAL RESULTS AND DISCUSSION

The following chapter presents the results of powder properties, powder bed distribution, and the consistency of selective laser melted specimens. The relation between results is discussed as they appear within the chapter.

4.1 Powder characterization

The powder properties presented resulted from the static automated imaging process and they include the PSD, circularity, elongation, and convexity of virgin Praxair and Deloro CoCrMo powders. The chemistry of the powders was not analysed, and the chemical composition as supplied by the manufacturers was represented in Table 3-1. From the static automated imaging process, the PSD distribution curves for both powders were obtained and are shown in Figure 4-1.

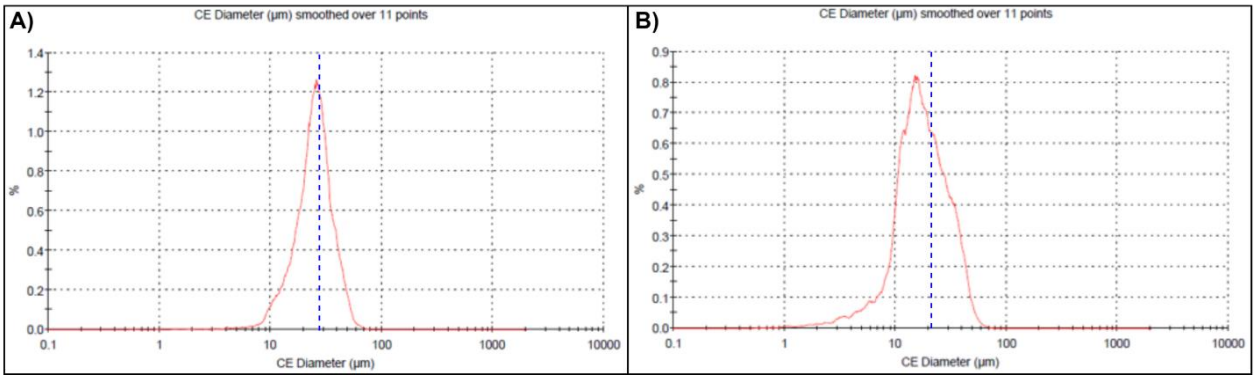

Figure 4-1: PSD of A) virgin Praxair CoCrMo powder and B) virgin Deloro CoCrMo powder

The PSD analysis of virgin powder for both powder grades showed that the Praxair powder followed a normal distribution whilst the Deloro powder followed a single peak positively skewed distribution. As can be seen in Figure 4-1, the Deloro powder has a wider distribution compared to the Praxair powder. The blue dashed line represents the mean particle size of each powder, from the Deloro powder, the distribution peak is on the left of the mean particle size (blue dashed line) indicating the powder has a positively skewed distribution. With the distribution being positively skewed, this indicates that the powder contained more fine particles compared to larger particles. The particle size characteristics are presented in Table 4-1.

Table 4-1: Powder size distribution of virgin Praxair and Deloro CoCrMo powders

Particle Size Distribution		Praxair	Deloro
Minimum	[µm]	0,59	0,54
Maximum	[µm]	83,29	85,18
Mean	[µm]	28,92	20,14
D10	[µm]	16,16	8,88
D50	[µm]	28,19	17,85
D90	[µm]	41,68	35,05
St. Dev	[µm]	10,36	10,64
RSD	[%]	36,01	52,53
Span	[-]	0,905	1,466

Both powders are similar in terms of minimum and maximum particle sizes, with the minimum particles around 0.57 µm in diameter and the maximum size particles around 84.24 µm. As can be seen from Table 4-1, the Deloro powder is finer than the Praxair powder, with a mean particle size of 20.14 µm compared to 28.92 µm, respectively. Overall, the Deloro powder has a D10 ,D50 and D90 all smaller than the Praxair powder, further supporting that it is a finer powder grade. As mentioned earlier, the Deloro powder had a wider distribution, the span is a representation of this, with the Praxair powder having a span of 0.905 compared to a span of 1.466 of the Deloro powder. The relative standard deviation (RSD) of the Deloro powder is larger than the Praxair powder, which supports the span of each powder as a higher RSD value indicates a wider distribution.

The powder morphology was measured simultaneously with the PSD during the static automated imaging process, and the results are presented in Table 4-2. Both powders showed some near perfectly spherical particles, with some having no satellites with circularity and convexity of 1.

Table 4-2 : Powder morphology of virgin Praxair and Deloro CoCrMo powders

Powder Shape Factors		Praxair	Deloro
Convexity	Minimum	0,580	0,507
	Maximum	1,000	1,000
	Mean	0,977	0,981
Circularity	Minimum	0,199	0,079
	Maximum	1,000	1,000
	Mean	0,893	0,905
Aspect Ratio	Minimum	0,211	0,158
	Maximum	1,000	1,000
	Mean	0,875	0,864

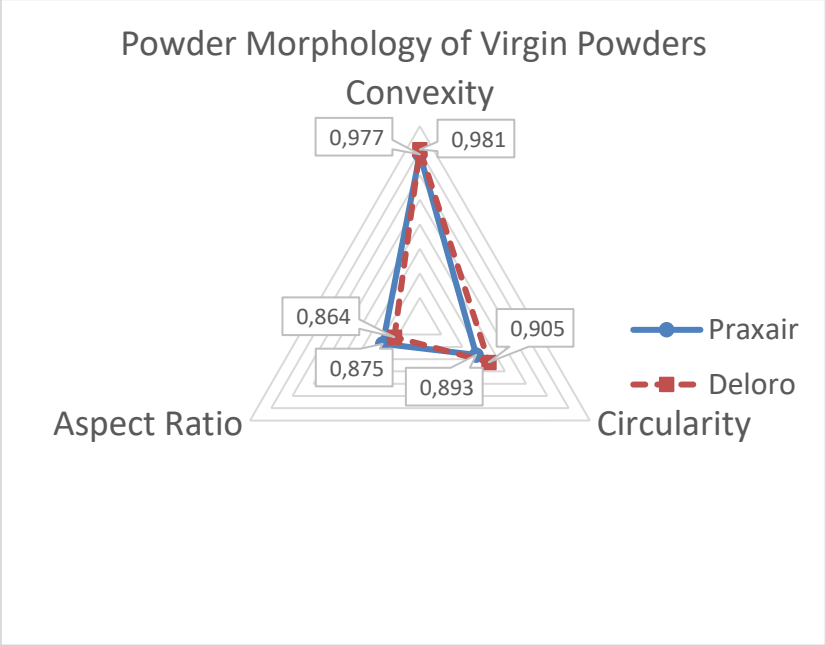

Figure 4-2: Radar comparison of virgin powder morphology

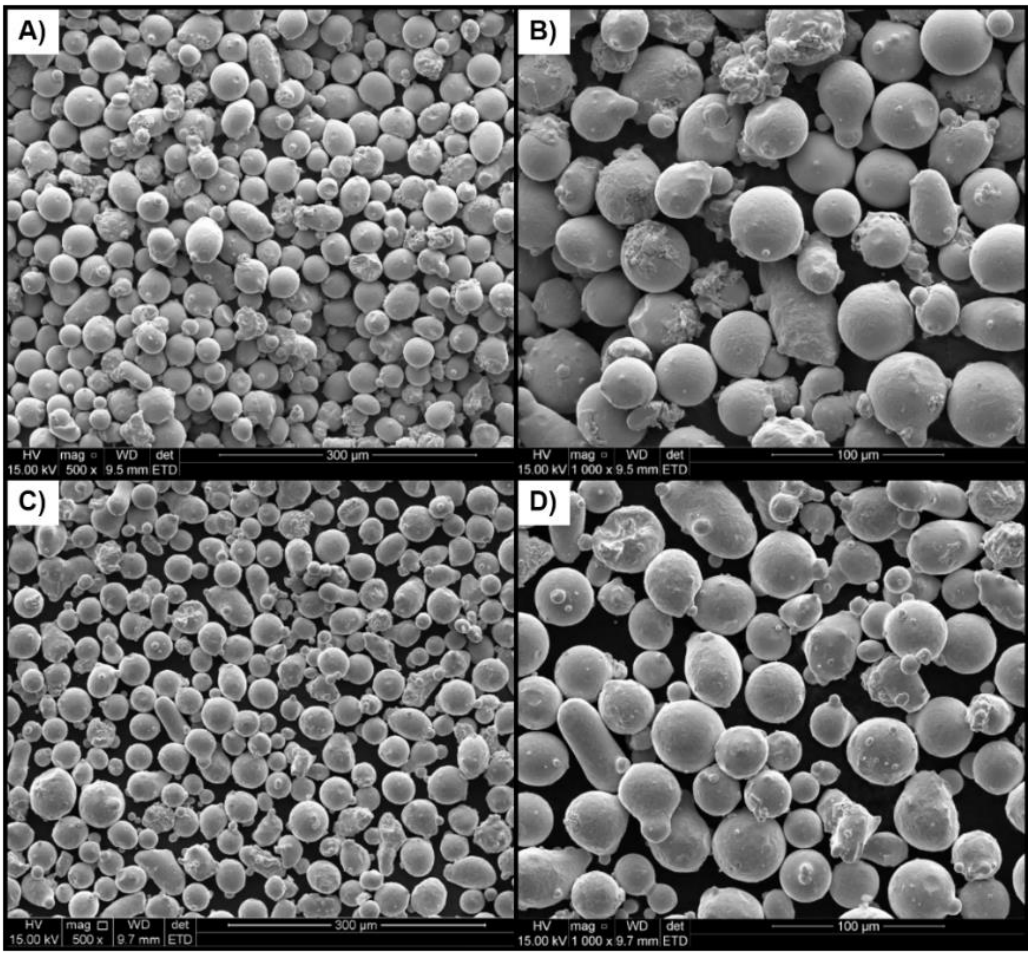

Figure 4-3 : SEM Images of virgin CoCrMo powder A,B) Praxair and C,D) Deloro

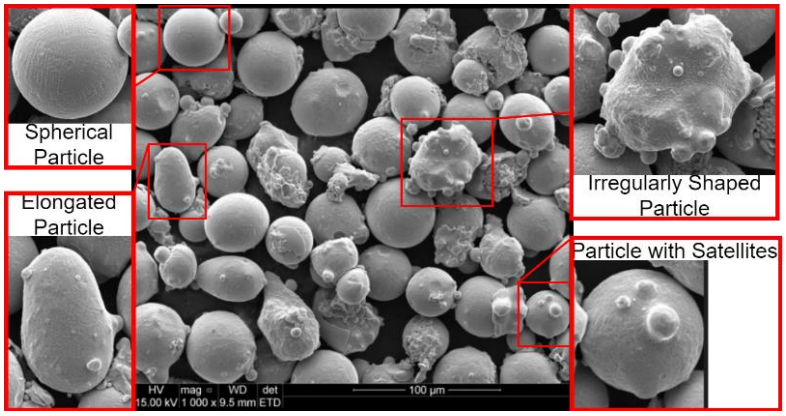

Figure 4-4: SEM image of particle imperfections of virgin Praxair CoCrMo powder

Both the Praxair and Deloro powders were gas atomised powders, and images of their morphology can be seen in Figure 4-3. Majority of the powder particles appear to be spherical which is typical of gas atomised powders. From the shape factors presented in Table 4-2 of both powders, particles with a poor convexity and circularity were measured, and this indicates irregularly shaped particles are present in both virgin powders. Irregularly shaped particles were in the form of elongated particles, non-spherical particles, and particles with satellites, as can be seen in Figure 4-4. Overall, similar particle morphologies were seen for both the virgin Praxair and Deloro powder.

The measured true density using He pycnometry of each powder was 8.364 g/cm3 and 8.329 g/cm3 for the Praxair and Deloro powders, respectively. Both powder densities were within 0.5 % of each other, with differences in the densities most likely due to the chemical composition variations and internal porosity. The internal porosity of the powder can be seen in Figure 4-5, highlighted by the red outlines.

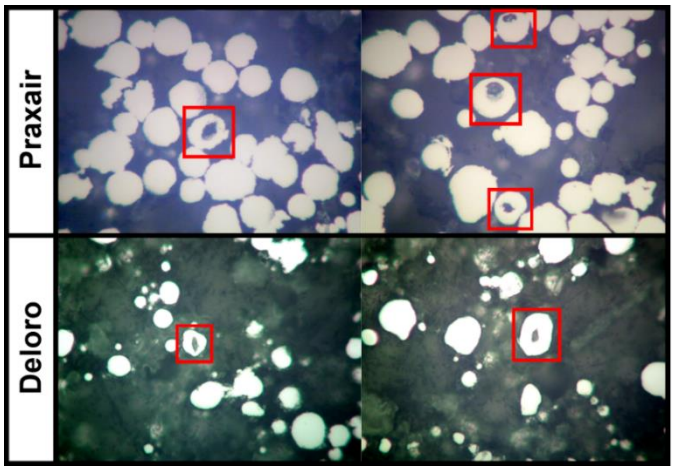

Figure 4-5: Micrographs of a cross section of both virgin Praxair and Deloro powders indicating internal porosity

Since the particles themselves have internal porosity and are inaccessible from the particle surface, the porosity was factored into the density determination of the powder. Therefore, with internal porosity present, it may be assumed that the measured true density of both powders is slightly lower than it should be. However, for this study, it was assumed that the powder particles were 100 % dense, and the measured true density was used for determining the relative density of manufactured components.

4.2 Powder bed density results

The PBD results indicated an inconsistent powder layer was deposited, resulting in variations in the powder packing efficiencies across the build plate. The Deloro powder represented a higher PBD than the Praxair powder across both respective layer thicknesses. PBD results measured at each position on the build plate for both powders at both layer thicknesses are represented in Table 4-3.

Table 4-3: PBD at each build plate location

Build Plate Location	Praxair		Deloro	
	25 µm	30 µm	25 µm	30 µm
	PBD	PBD	PBD	PBD
Top	59,90%	59,47%	61,92%	61,90%
Bottom	59,94%	59,78%	61,80%	61,95%
Centre	60,05%	59,83%	61,95%	62,04%
Left	60,21%	60,02%	62,11%	62,27%
Right	59,94%	59,97%	61,87%	61,89%
Average	60,01%	59,81%	61,93%	62,01%

From the PBD results, the Deloro results are higher by around 2 % for both layer thicknesses. This increase in average PBD can be related to powder PSD and morphology. From section 4.1, the Deloro powder has a wider PSD with a larger span which can be seen in Figure 4-1. The Deloro powder also has smaller powder particles, as represented in Table 4-1. Therefore, with a wider PSD and span, coupled with more fine particles, the packing efficiency is higher due to the particles filling the volume more efficiently and resulting in a higher PBD than the Praxair powder.

Looking individually at the consistency of the PBD across each build plate, the PBD variations were plotted in a heat map style graph in MATLAB. In order to compare the PBD variations for each build, a PBD variation distinction of minor to major was made, with variations less than 0.2 % being minor and larger than 0.5 % being major. This distinction is represented by Table 4-4.

Table 4-4: PBD variation distinction

PBD Variation	
< 0,2 %	Minor
> 0,2 % & < 0,5 %	Medium
> 0,5 %	Major

The PBD results were plotted in MATLAB according to a colour scale, with blue representing minor PBD variations and red presenting major variations, according to Table 4-4. The SLM machine utilised had a build plate of 100 mm in diameter. Due to the positioning of the PBD specimens, a diamond-shaped area was evaluated, covering most of the build plate as shown in Figure 4-6.

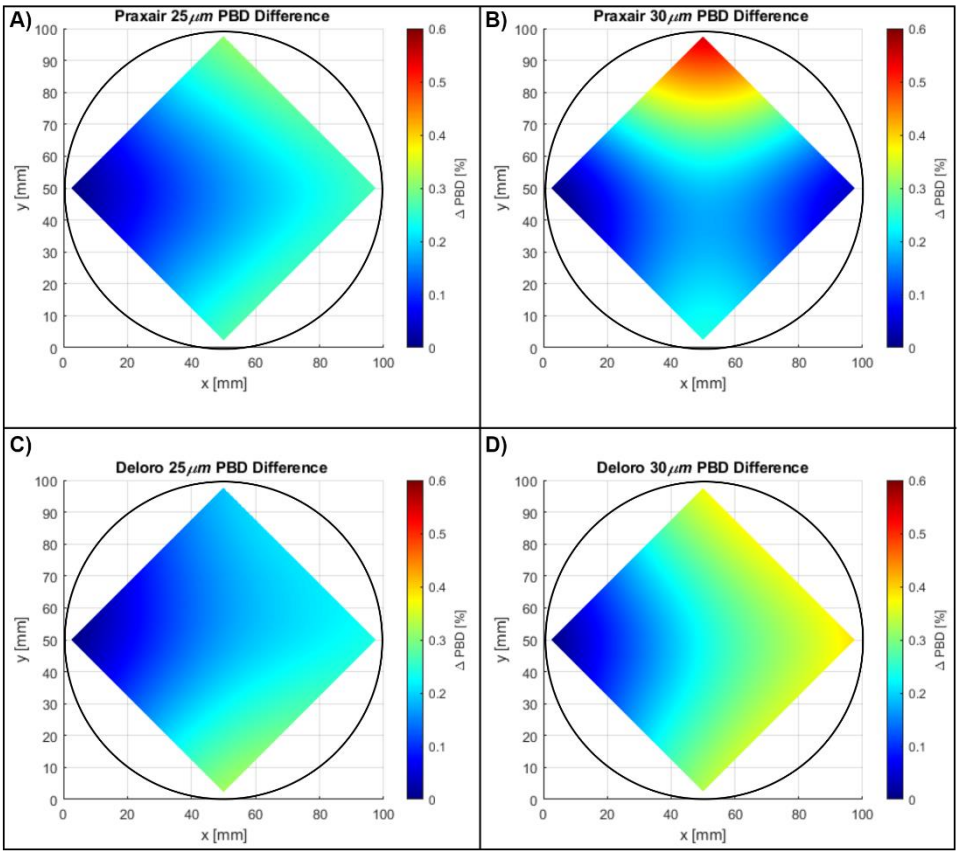

Figure 4-6: PBD build platform variation for Praxair A) and B), for Deloro C) and D) at each respective layer thickness

The PBD variations show fewer variations across the build plate for the 25 µm layer thickness of both powders. Only minor to medium PBD variations are experienced, with similar variation results seen in both Figures 4-6 A) and C). For both powders and both layer thicknesses, the highest PBD experienced across each build was seen on the left of the build plate nearest to the powder reservoir where the first powder is deposited.

For the 30 µm layer thicknesses, the PBD variations for both powders were more significant, with the Praxair powder showing larger variations of up to 0.54 % compared to the largest PBD variation of the Deloro build plate being 0.38 %. Overall, a more significant inconsistency in PBD for the 30 µm layer thickness compared to the 25 µm layer thickness was mainly due to more spatter experienced during the prints. With increased spatter, more undesirable powder particles are spread across the build plate resulting in poorer packing efficiencies. The increase in spatter can be caused by process parameters that were not suited for the layer thickness resulting in undesirable particles ejecting from the melt zone and spreading across the build plate.

4.3 Part density of SLM components

The following section presents the results of Archimedes' density measurements for SLM parts produced at each layer thickness from each CoCrMo powder type. The part density results are presented as relative density. The density distribution presents the consistency of relative part density across the build plate.

4.3.1 Density distribution across the build plate

Similar to the PBD results, the part density varied across the build plate and was inconsistent. Both powders with the same processing parameters produced highly dense parts, with the 30 µm layer thickness producing slightly less dense parts as shown in Table 4-5.

Table 4-5: Part density range

Part Density								
	25 µm Layer Thickness				30 µm Layer Thickness			
	Praxair		Deloro		Praxair		Deloro	
	[g/cm3]	[-]	[g/cm3]	[-]	[g/cm3]	[-]	[g/cm3]	[-]
Mean	8,359	99,93%	8,263	99,21%	8,295	99,17%	8,232	98,84%
Max	8,370	100,06%	8,272	99,32%	8,321	99,49%	8,254	99,09%
Min	8,334	99,64%	8,255	99,11%	8,255	98,70%	8,212	98,59%

The Praxair powder produced parts with a maximum density of up to 8.370 g/cm^3 compared to Deloro's maximum density of 8.272 g/cm^3. To compare the part densities, the relative part densities were calculated according to the measured true density of each powder. The relative part density of the Praxair powder manufactured parts were higher than the Deloro powder manufactured parts for both layer thicknesses. However, for the 25 µm layer thickness, both powders manufactured parts with a mean relative part density greater than 99 %, which is regarded as excellent for AM components. The mean relative part density for the 30 µm layer thickness was 99.21 % and 98.84 % for the Praxair and Deloro powders, respectively. Therefore, an increase in the layer thickness showed a decrease in relative part density.

It must be noted that the relative density is dependent on the true density of the powder/material since the density calculated from Archimede's principle is referenced to a material. From Figure 4- 5, the small internal porosity in the powders would influence the true density, and the measured true density is slightly lower than it should be. This is a possible reason why the maximum relative part density for the Praxair 25 µm layer thickness is 100.06 %, meaning the manufactured part has a higher density than the measured powder true density.

Comparing the density variations across the build platform at different build locations, the results indicated that the density distribution across the build plate was inconsistent, with the powder deposited across the build plate at these specific build locations having a significant influence. The build locations where the powder showed variations, is also where the part density showed variations relative to the rest of the build. To visualise these relative part density variations for each set of cubes manufactured, the relative density variation was labelled as minor if less than 0.1 % to major if greater than 0.5 %; this distinction is set out in Table 4-6.

Table 4-6 : Part density variation severity

Part Density Variation	
< 0,1 %	Minor
> 0,1 % & < 0,5 %	Medium
> 0,5 %	Major

The results of each density distribution were plotted in MATLAB according to a colour scale to represent the results as shown in Figure 4-7. Blue corresponds to minor density variation, whilst red corresponds to major density variation according to Table 4-6. The SLM machine's actual build area is 100 mm in diameter; however, due to the positioning of the cube specimens, an octagonal shape was evaluated, covering most of the build platform as shown in Figure 4-7.

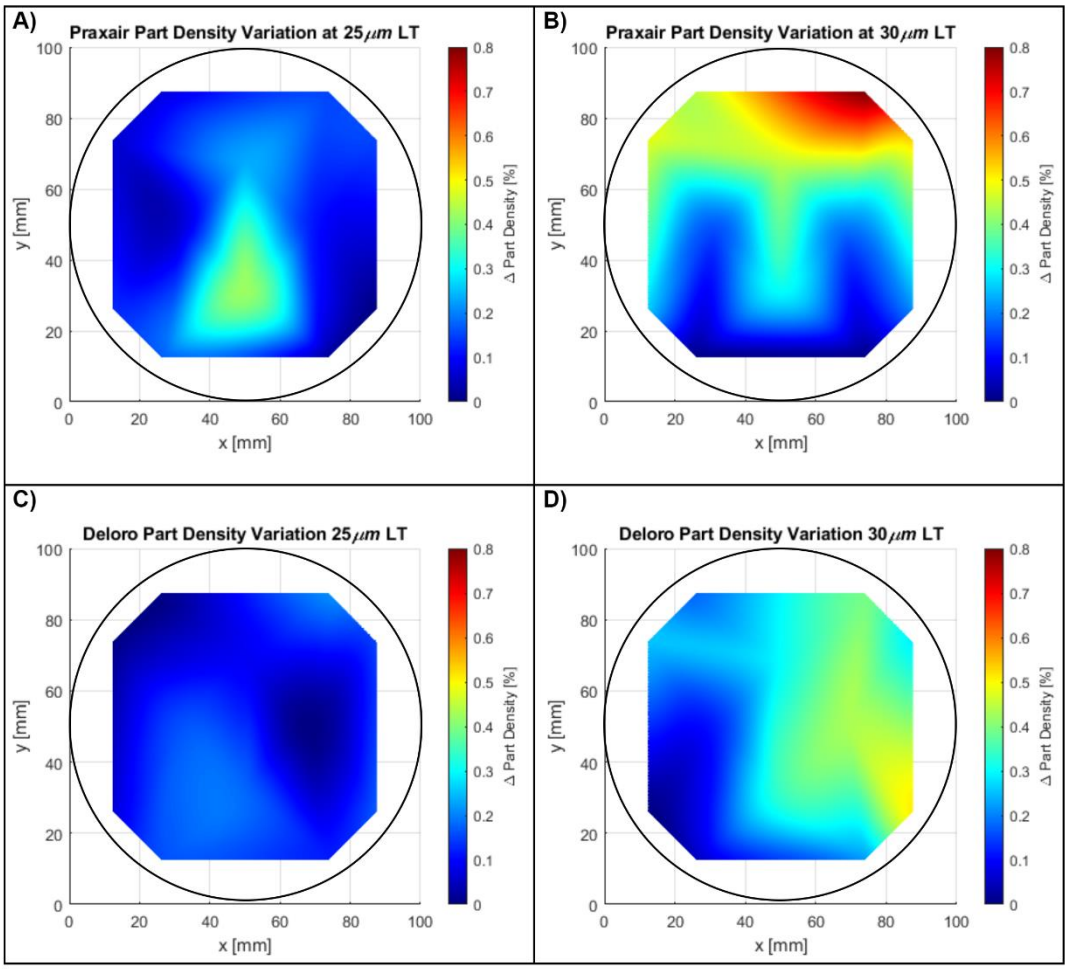

Figure 4-7: Part density variation Praxair A) and B), for Deloro C) and D) at each respective layer thickness

Figure 4-7 A) and C) shows that the part density is relatively consistent across the build plate at 25 µm with only minor to medium density variations experienced. The part density variation is the most consistent across the build plate for the Deloro 25 µm layer thickness, as seen in Figure 4- 7 C). At a layer thickness of 30 µm, the density variations increased with major density variations of up to 0.8 % for the Praxair powder seen in Figure 4-7 B).

4.4 Effective layer thickness

Since the general PBD and part density of each build was established, based on the densification of components from a powder bed during the build, the actual layer thickness during manufacturing could be calculated. The effective layer thickness (T_{eff}) was calculated according to equation 2-1 using the mean measured PBD and relative part densities for each build. The results are compared to the derived criteria of Spierings et al. [1], [58] shown in equations 2-2 and 2-3, which suggests the effective layer thickness to be 50 % greater than the D90 and D90 should be five times greater than D10 of the powder PSD. The calculated effective layer thickness of each powder during the 25 µm and 30 µm layer thicknesses are shown in Figure 4-8:

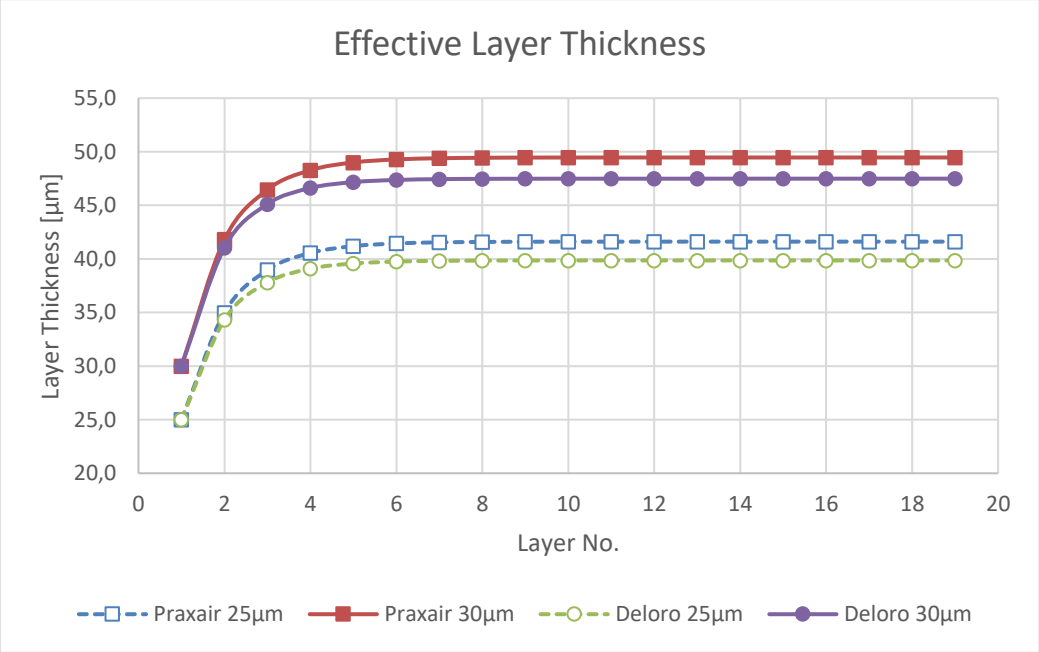

Figure 4-8: Calculated effective layer thickness for each powder and layer thickness

Figure 4-8 shows that after ten layers, the calculated T_{eff} reaches a constant value for both powders at both prescribed layer thicknesses. Therefore, any base plate inconsistencies such as an unlevel build plate were assumed negligible because after ten layers, the amount of powder deposited per layer was level and consistent. For the Deloro powder at each prescribed layer thickness, the T_{eff} is slightly higher due to the Deloro powder having a higher PBD. The calculated T_{eff} of each respective build is shown in Table 4-7:

Table 4-7: Calculated T_{eff} and ratio of T_{eff} with D_{90}

		Praxair		Deloro	
		25 µm	30 µm	25 µm	30 µm
T_{eff}	[µm]	41,613	49,466	39,859	47,488
T_{eff} / D_{90}	[-]	1,119	1,344	1,561	1,895
D_{90} / D_{10}	[-]	3,560	3,570	4,963	4,172

After measuring the PBD and relative densities for all builds, when the prescribed layer thicknes was increased from 25 µm to 30 µm, the effective layer thickness of the Praxair and Deloro powders increased by 7.853 µm and 7.629 µm respectively. Since the laser energy density was kept constant at both prescribed layer thicknesses, this resulted in the laser having to penetrate and melt 18.872 % and 19.14 % for the Praxair and Deloro powders respectively. The PSD values (D90 and D10) used to calculate the ratios were values determined from the powder captured within the PBD specimens. Based on the ratios, both powders at both prescribed layer thicknesses had a T_{eff}/D90 ratio of greater than 1, indicating that powder particles with a size of D90 were deposited during the recoating process of a new layer. Therefore, most of the particles

were deposited onto the build platform, given that they were smaller than the T_{eff}. According to Spierings et al. [1], [58], the ratio of D90/D10 should be around five; based on the calculated ratios in Table 4-7, the Deloro is closer to this criteria than the Praxair powder. Therefore, the Deloro powder has a more desirable ratio of fine to coarse particles allowing for better packing efficiency. This criterion is true as the Deloro powder produced a better PBD than the Praxair powder, indicating a better packing efficiency.

4.5 Influence of powder characteristics on PBD and part density

In the following section, the results of the powder analyses, PBD and part density for each powder at the specific layer thickness were compared to understand the reasons behind the part density variations and inconsistencies across the build plate. To further understand the variations in part density, cubes with the maximum and minimum part densities of each build were cross-sectioned and metallographically prepared to evaluate the porosity.

4.5.1 Praxair 25 µm layer thickness

It has been established that the part density varies across the build plate for the Praxair 25 µm layer thickness components. This variation is caused by an uneven powder distribution across the build plate. To evaluate the build plate, the mean, maximum and minimum values in terms of the part density and PBD, PSD and circularity of the powder were represented in Table 4-8.

Table 4-8: Praxair 25 µm layer thickness evaluation

Praxair 25um				
	Part Density	PBD	PSD average	Circularity
	[%]	[%]	[um]	[-]
Mean	99,93%	60,01%	23,69	0,9060
Max	100,06%	60,21%	26,25	0,9180
Min	99,64%	59,90%	22,1	0,8950

As can be seen in Table 4-8, the most significant relative part density variation is only 0.42 % which may be regarded as a medium variation according to Table 4-6's distinction. Medium variations for the PBD were also observed, with a maximum PBD variation of 0.31 %. The PSD and circularity of the powder also varied across the build plate, with a larger variation seen in the circularity of the powder as shown in Figure 4-9.

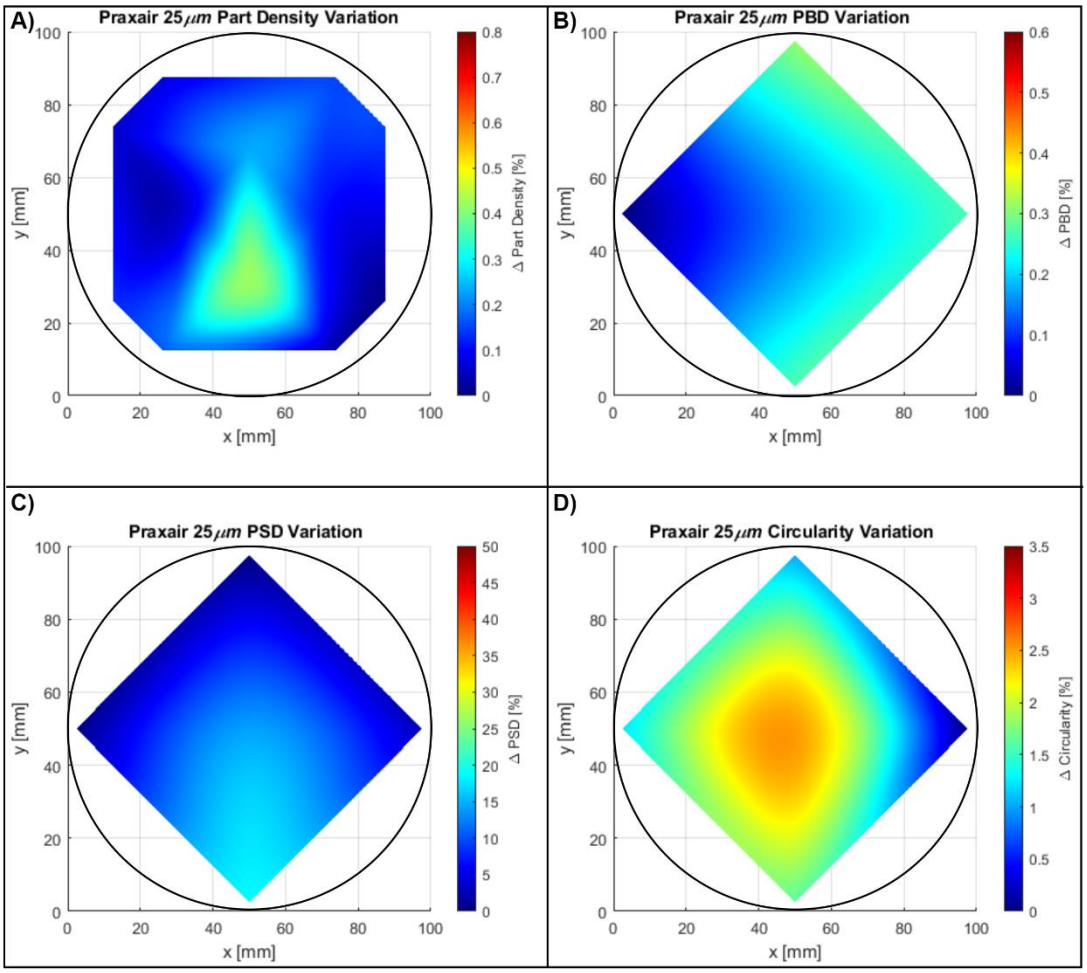

Figure 4-9: Praxair 25 µm layer thickness variations of A) Part density, B) PBD, C) PSD and D) Circularity

As can be seen from Figure 4-9 A), the largest part density variation is experienced near the centre and bottom of the build plate, where the lowest relative part density of 99.64 % was measured. At this region of the build plate, the PBD started to decrease, PSD started to increase, and powder particles showed a decrease in circularity. Larger and less spherical particles in this region create open spaces within the powder bed, resulting in a decrease in the PBD. These open spaces allow for higher penetration of the laser, rapidly heating up gas trapped between the particles and the sudden expansion of this gas results in spattering [75]. When spattering occurs, the melt pool loses material. As a result of differences in the amount of powder deposited across the build plate, a variation in the part density occurred.

The maximum relative part density was measured in cube 7 at 100.6 % dense, and the minimum relative part density was measured in cube 3 at 99.63 % dense. The cross sections of the cubes are shown in Figure 4-10.

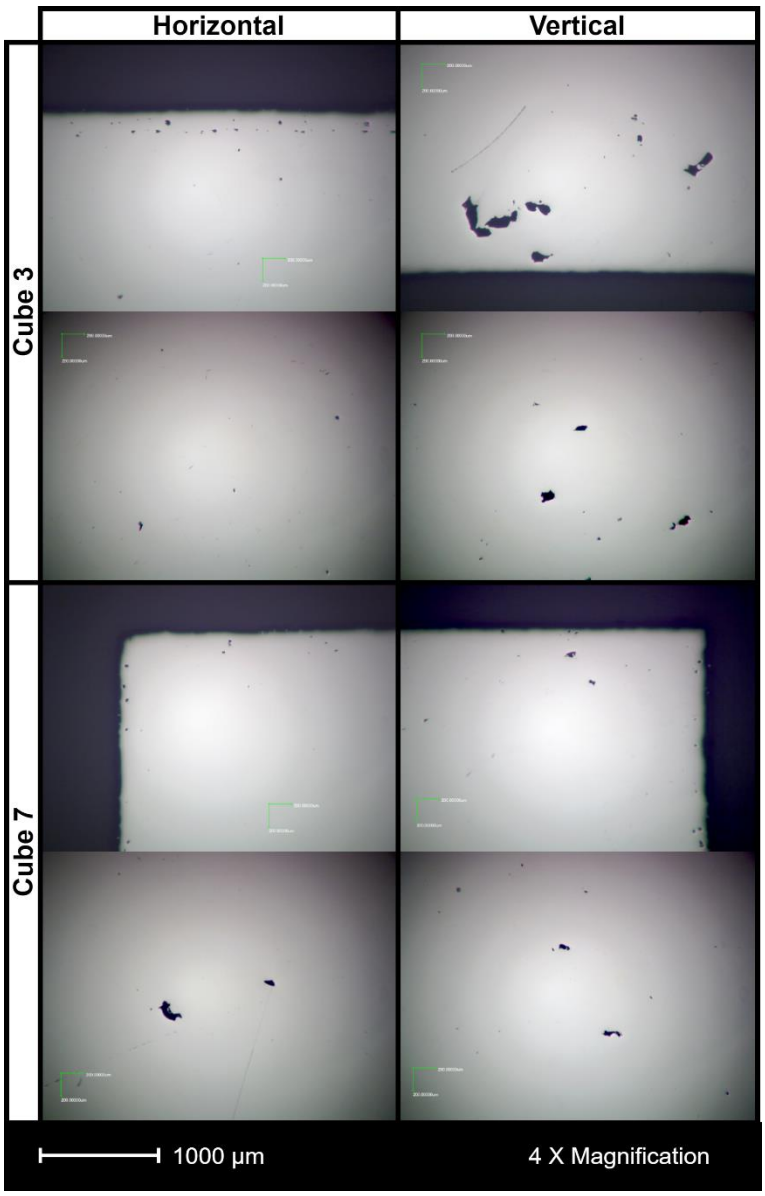

Figure 4-10: Micrographs of cross sections in the horizontal and vertical planes of cubes manufactured with Praxair Powder at a layer thickness of 25 µm

As can be seen in Figure 4-10, there is porosity within the cubes. The porosity is distributed across the cubes and visible in both the horizontal and vertical planes. Along the contours of the cubes in the horizontal plane, small pores are observed and are more circular in shape, indicating keyhole porosity. During the contour process of manufacturing, the laser power is increased, and the scan speed is decreased compared to laser processing parameters used during hatching (refer to Table 3-2). Therefore, the applied energy density is higher. This energy density increase allows could allow keyholing to occur and pores to generate as a result. The larger pores visible are irregularly shaped, which is a characteristic of lack of fusion porosity. Since the lack of fusion porosity is scattered across the planes of the cubes, the likely cause of the porosity could be inconsistent powder layers since differences of powder characteristics at various build locations were observed. An inconsistent powder layer caused the packing efficiency across the build plate to vary and leads to an inconsistent or unstable melt pool. Cube 3 was located in the bottom

central region of the build plate and in this region is where poor powder circularity was measured, which decreased the packing efficiency. The cause of inconsistent powder layers was likely due to spatter generated from the melt zone, the powder layer and spatter that occurred during the build is shown in Figure 4-11.

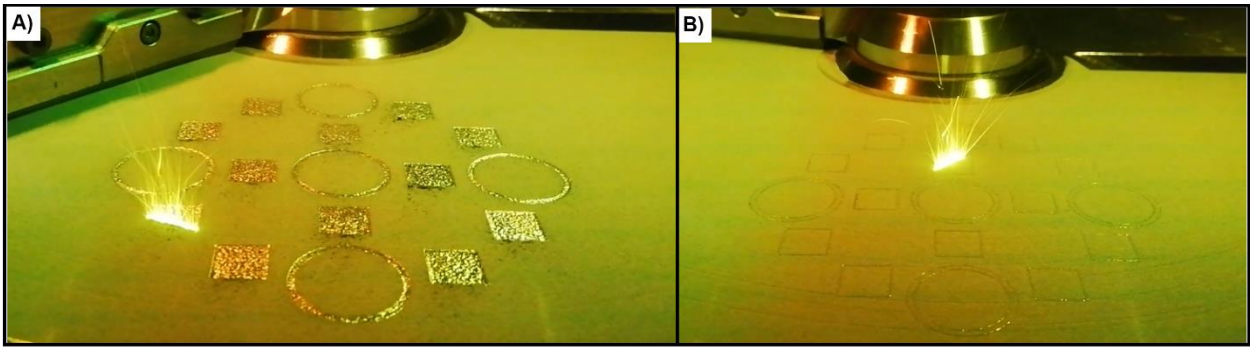

Figure 4-11: Spatter and powder spreading of Praxair powder at a 25 µm layer thickness

From observing Figure 4-11, it is evident that spatter occurs and from Figure 4-11 A), the spatter particles ejected from the melt zone can be seen across the build platform as small black speckles. Looking closer at Figure 4-11 A), the spatter appears to build up and agglomerate at the end of each hatching process. During the recoating process, this extensive build-up of spatter and agglomerated particles will be spread across the build platform and further influence the packing efficiency. When larger irregularly shaped spatter particles are present, larger voids are generated between particles; with larger particles and larger voids to fill, the energy applied to melt the particles needs to be higher to achieve complete melting.

4.5.2 Praxair 30 µm layer thickness

The Praxair 30 µm layer thickness build measured the most significant variations in relative part density, PBD, PSD and powder circularity. The range of these variations is provided in Table 4-9:

Table 4-9: Praxair 30 µm layer thickness evaluation

Praxair 30um				
	Part Density	PBD	PSD average	Circularity
	[%]	[%]	[um]	[-]
Mean	99,17%	59,81%	23,29	0,9120
Max	99,49%	60,02%	28,02	0,9257
Min	98,70%	59,47%	19,53	0,8963

From the results shown in Table 4-9, the largest relative part density variation measured was 0.79 % which is considered major according to the distinction made in Table 4-6. A major variation for the PBD was also observed with a maximum measured variation of 0.55 %. Variations in the PSD and powder circularity were also observed, with the circularity in regions varying by up to 3.18 % as shown in Figure 4-12.

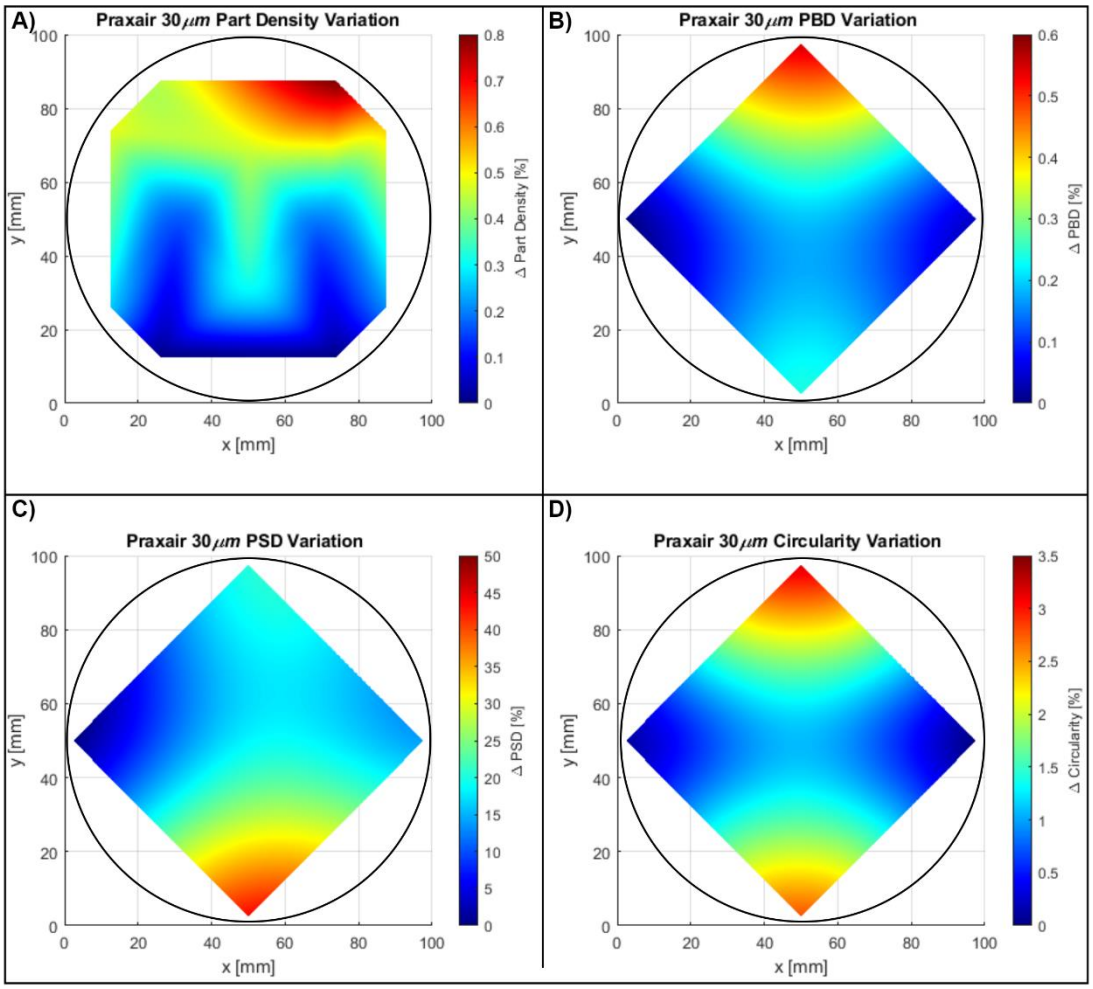

Figure 4-12: Praxair 30 µm layer thickness variations of A) Part density, B) PBD, C) PSD and D) Circularity

Figure 4-12 A) shows that the largest relative density variation is located at the top right of the build plate; the measured relative part density was 98.7 %. When looking further at the PBD and circularity in Figure 4-12 B) and D), it is the same region on the build plate where the largest variations were measured. Similar to the explanation provided for the relative part density variations across the Praxair 25 µm layer thickness in the previous sub-section, the same applies to the 30 µm layer thickness with a higher degree of severity. The more significant relative part density variations are due to more spatter generated negatively impacting the powder bed and melt pool characteristics. Since the laser parameters remained constant with only the layer thickness changing, a higher laser energy density would be required to fully melt all the particles like in the 25 µm layer thickness. With more spatter occurring, a more inconsistent powder bed

was present during manufacturing and coupled with insufficient energy to fully melt the powder particles, the part density variations were more significant across the build plate.

The maximum relative density was measured in cube 8 at 99.48 % dense, and the minimum relative density was measured in cube 5 at 98.68 % dense. The cross sections of the cubes are shown in Figure 4-13.

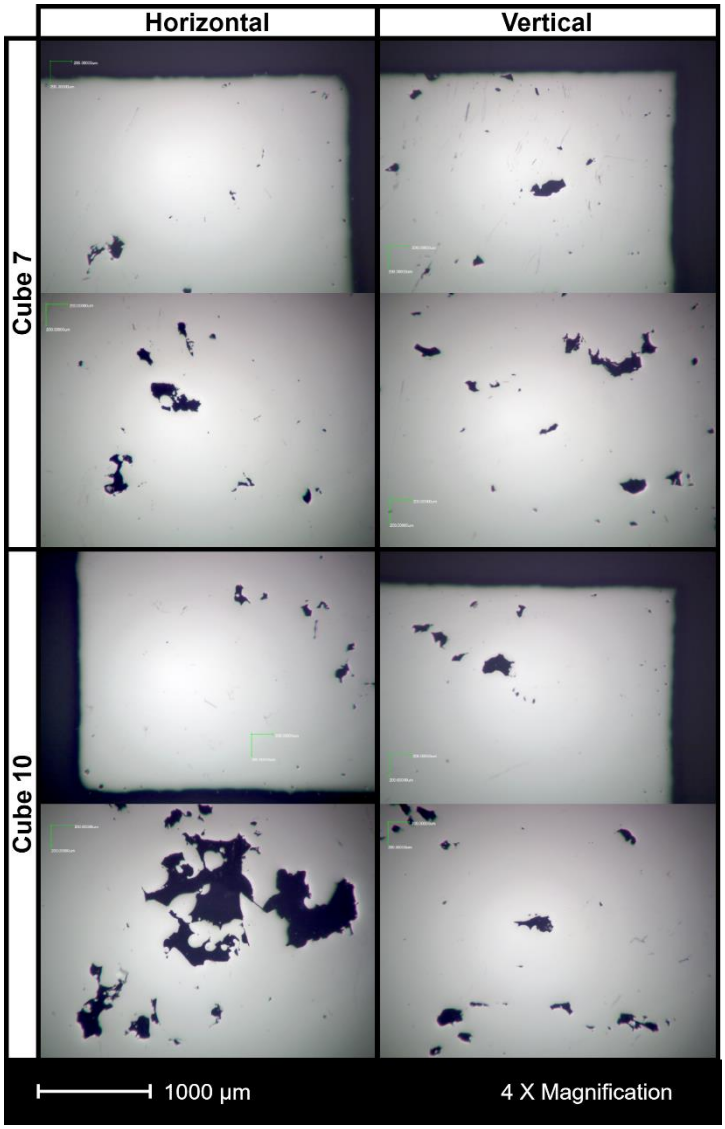

Figure 4-13: Micrographs of a cross section in the horizontal and vertical planes of cubes manufactured with Praxair Powder at a layer thickness of 30 µm

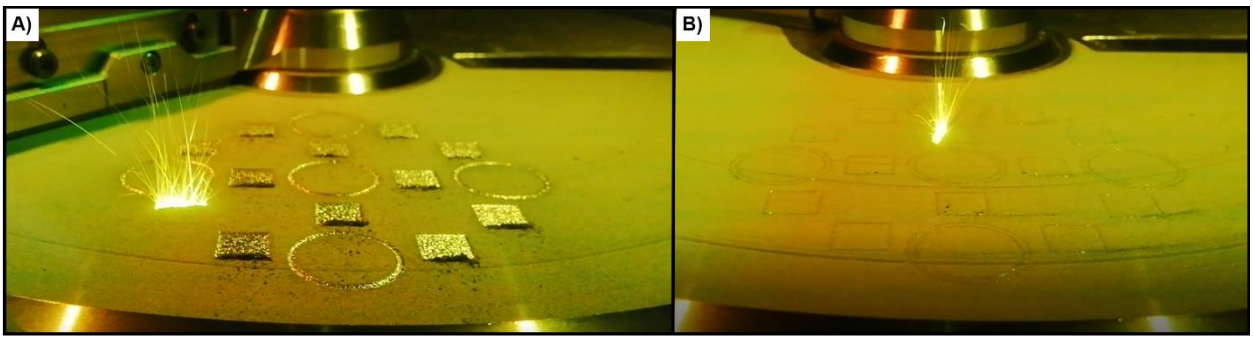

Figure 4-14: Spatter and powder spreading of Praxair powder at a 30 µm layer thickness

From Figure 4-13, it is clear that the main type of porosity is a lack-of-fusion porosity. The lack-of-fusion porosity formed due to spatter creating an inconsistent powder bed, as seen in Figure 4-14. Figure 4-14 A) shows how the spatter agglomerated at the end of the scanning pattern (hatching process) for each part. Looking further at the rest of the powder bed, more prominent black speckles can be seen scattered across the powder layer; these black speckles are the spatter particles that are ejected from the melt pool. With all the spatter generated during the melting of each layer, when the next layer is deposited and scraped across the build plate, these larger spatter particles cause inconsistencies in the subsequent powder layer, as seen in Figure 4-14 B). When larger irregularly shaped spatter particles are present, larger voids are generated between particles; with larger particles and larger voids to fill, the energy applied to melt the particles needs to be higher to achieve complete melting.

4.5.3 Deloro 25 µm layer thickness

The Deloro 25 µm layer thickness build measured the least significant variations in relative part density, PBD and powder circularity. The range of these variations is provided in Table 4-10:

Table 4-10: Deloro 25 µm layer thickness evaluation

Deloro 25µm				
	Part Density	PBD	PSD average	Circularity
	[%]	[%]	[um]	[-]
Mean	99,21%	61,93%	14,32	0,9330
Max	99,32%	62,11%	15,89	0,9403
Min	99,11%	61,80%	10,53	0,9253

Table 4-10 shows that the largest relative density variation was 0.21 %, which is classified as a medium variation according to the distinction made in Table 4-6. Looking at the PBD a medium variation of PBD was observed, with the maximum measured PBD variation being 0.31 %.

Variations in the PSD and circularity were also observed, with maximum variations across the build plate being 50.87 % and 1.6 %, respectively. These variations are displayed in Figure 4-15.

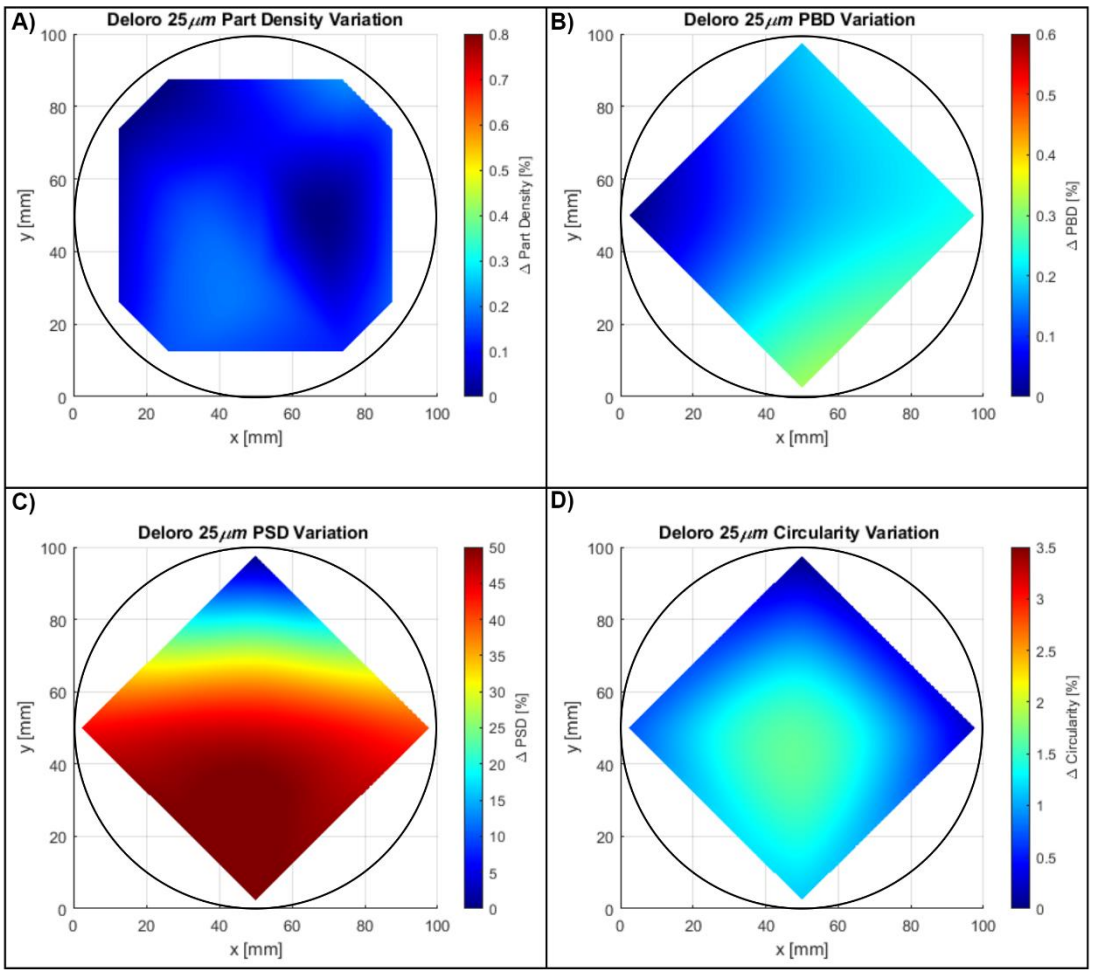

Figure 4-15: Deloro 25 µm layer thickness variations of A) Part density, B) PBD, C) PSD and D) Circularity

From Figure 4-15 A), it can be seen that minor relative densities were observed; however, when looking at the PSD variations, a significant variation was observed. The large variation is due to the fine particles measured at the top of the build plate, with the rest of the build plate being relatively consistent compared to each position. The mean PSD measured across the build plate at positions left, centre, right, and the bottom was 15.12, 15.35, 14.74 and 15.89 µm, respectively, compared to the top mean PSD of 10.53 µm. Since all the mean particle sizes were still in the finer range of particles for AM, it showed minimal influence on the part density. The PBD and powder circularity had minor to medium variations and had similar trends to what was observed for the Praxair 25 µm layer thickness, although no clear correlations to the part density for this build was observed.

The maximum measured relative density was in cube 11 at 99.31 %, and the minimum measured relative density was in cube 5 at 99.11 %. Cross sections of these cubes in the horizontal and vertical planes are displayed in Figure 4-16.

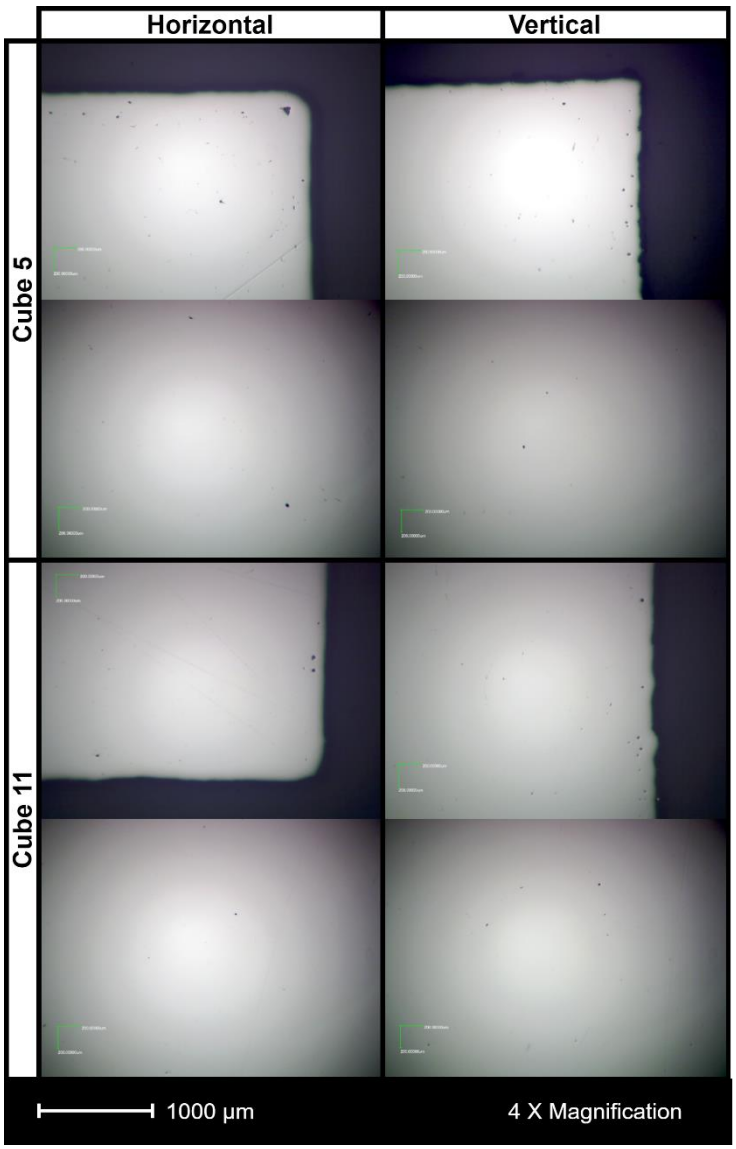

Figure 4-16: Micrographs of a cross section in the horizontal and vertical planes of cubes manufactured with Deloro Powder at a layer thickness of 25 µm

As can be seen in Figure 4-16, there is minimal porosity present within the manufactured parts. Most porosity found within the parts was along the contours, as seen in both cubes 5 and 11. The porosity along the contour is likely due to the increased laser power and decreased scan speed along the contour resulting in a higher energy density. This increase in energy density resulted in keyhole porosity since the pores observed are small and spherical, which is a characteristic of keyhole porosity.

During manufacturing, the spatter was minimal and consistent powder layers were observed. This can be seen in Figure 4-17.

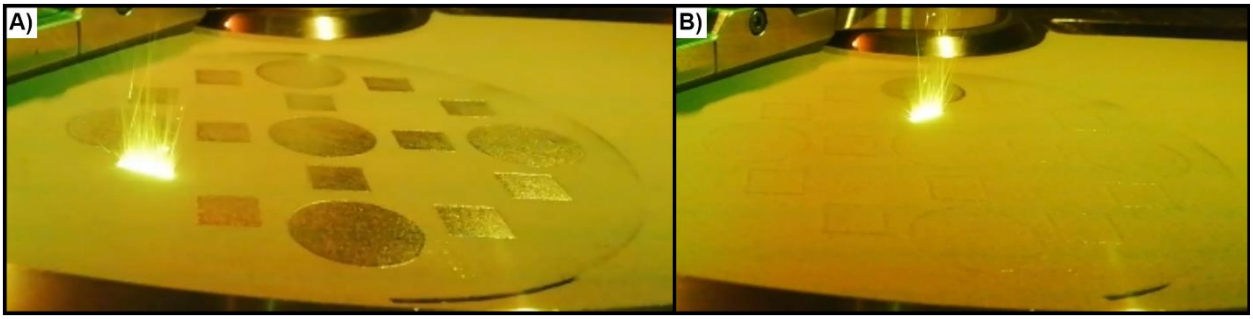

Figure 4-17: Spatter and powder spreading of Deloro powder at a 25 µm layer thickness

As shown in Figure 4-17 A), there is minimal spatter observed across the build plate, unlike what was observed for the Praxair powder builds. In Figure 4-17 B), a uniform and consistent powder layer can be observed, which is desirable for creating consistent components. It was seen above that this build manufactured the most consistent parts across the build plate in terms of relative density.

4.5.4 Deloro 30 µm layer thickness

The Deloro 30 µm layer thickness build measured variations in relative part density, PBD, PSD and powder circularity. The range of these variations is provided in Table 4-11:

Table 4-11: Deloro 30 µm layer thickness evaluation

Deloro 30 µm				
	Part Density	PBD	PSD average	Circularity
	[%]	[%]	[um]	[-]
Mean	98,84%	62,01%	14,89	0,9330
Max	99,09%	62,27%	16,52	0,9387
Min	98,59%	61,89%	13,32	0,9263

From Table 4-11, the most significant measured relative part density variation was 0.5 % which is classified as a medium to major variation according to the distinction made in Table 4-6. A medium variation of the PBD was observed, with the maximum PBD variation across the build plate being 0.38 %. Variations in the PSD and circularity were also observed, with 24.06 % and 1.31 % variations, respectively. These variations are displayed in Figure 4-18.

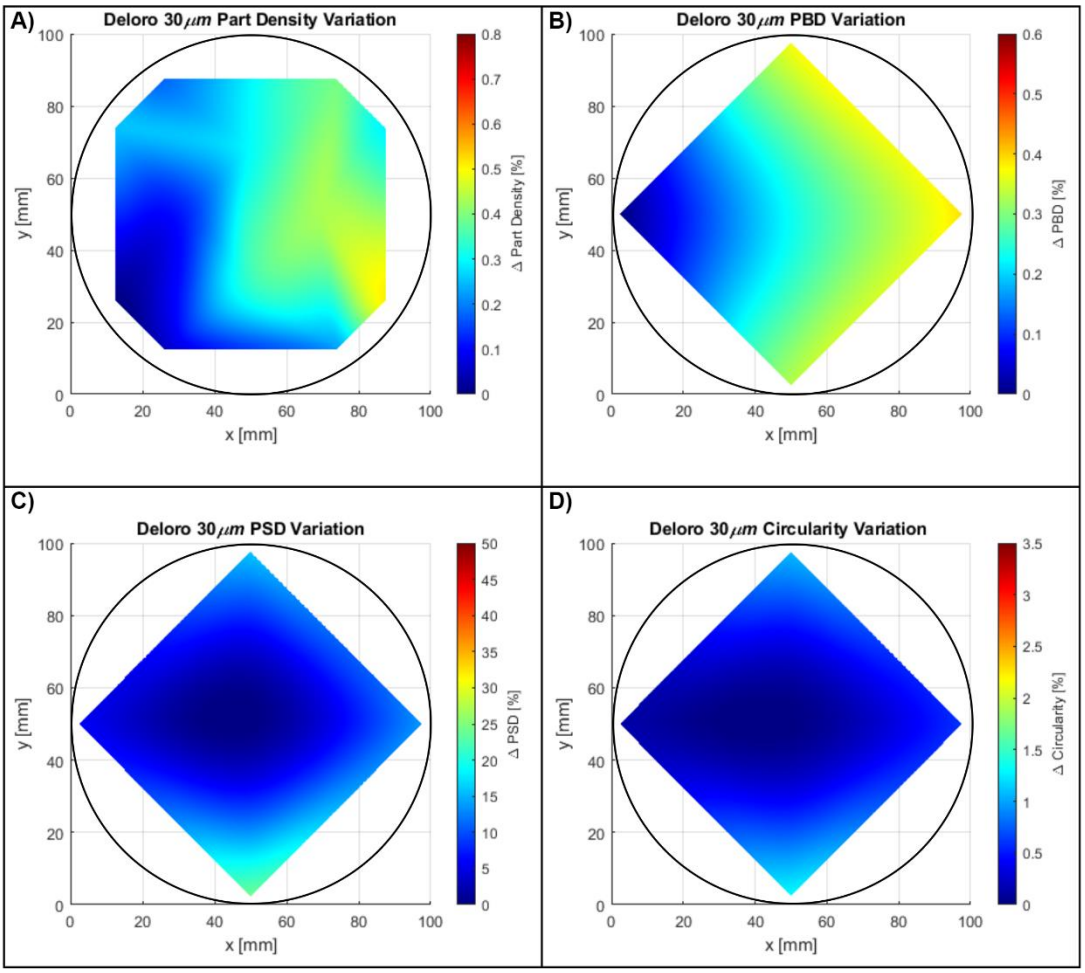

Figure 4-18: Deloro 30 µm layer thickness variations of A) Part density, B) PBD, C) PSD and D) Circularity

From Figure 4-18 A), it is seen that the relative part density varies across the build plate, with the highest part density recorded near the bottom left region of the build plate at 99.09 %. The part density appears to increase from the top-to-bottom centre line towards the right side of the build plate, with the lowest part density recorded at the bottom right region of the build plate at 98.59 %. When observing Figure 4-18 B), the PBD begins varying from the top-to-bottom centre line towards the right side of the build plate. Thus, a correlation between the part density and PBD variations is visible, and the likely contributor to the part density variations is the change in PBD. There was no correlation to the part density in terms of the PSD and circularity across the build plate.

The maximum measured relative density was in cube 10 at 99.09 %, and the minimum measured relative density was in cube 7 at 98.59 %. Cross sections of these cubes in the horizontal and vertical planes are displayed in Figure 4-19.

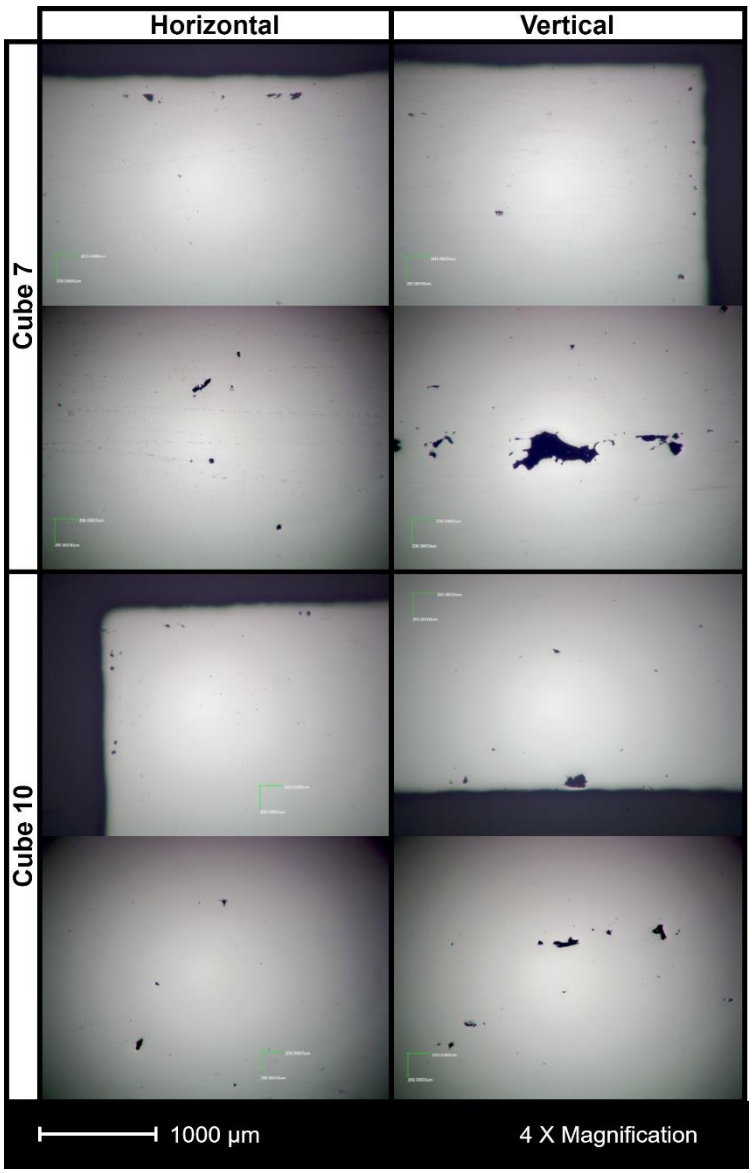

Figure 4-19: Micrographs of a cross section in the horizontal and vertical planes of cubes manufactured with Deloro Powder at a layer thickness of 30 µm

As seen in Figure 4-19, porosity is present in both cubes, with the type of porosity being a lack-of-fusion porosity. The porosity is irregularly shaped and varies in size and concentration in specific areas, which is characteristic of lack-of-fusion porosity. In the vertical plane cross-sections, elongated porosity is observed perpendicular to the build direction indicating the pores are aligned with the powder layers when building. Porosity found between layers is an indication of a poor powder layer that is inconsistent; therefore, with varying powder layers and insufficient energy applied to the region, lack-of-fusion porosity was possible. When observing the contours of the cubes in the horizontal plane, irregularly shaped pores are also evident, which is likely a lack of fusion porosity. These pores were likely caused by the manufacturing process where the contour is melted before the hatching commences. Therefore, spatter and denudation occur during the contouring process, resulting in powder particles being removed between the contour and the hatching area, resulting in insufficient powder to completely melt in that region, generating

lack-of-fusion pores. A representation of the spatter and powder layer during manufacturing can be seen in Figure 4-20.

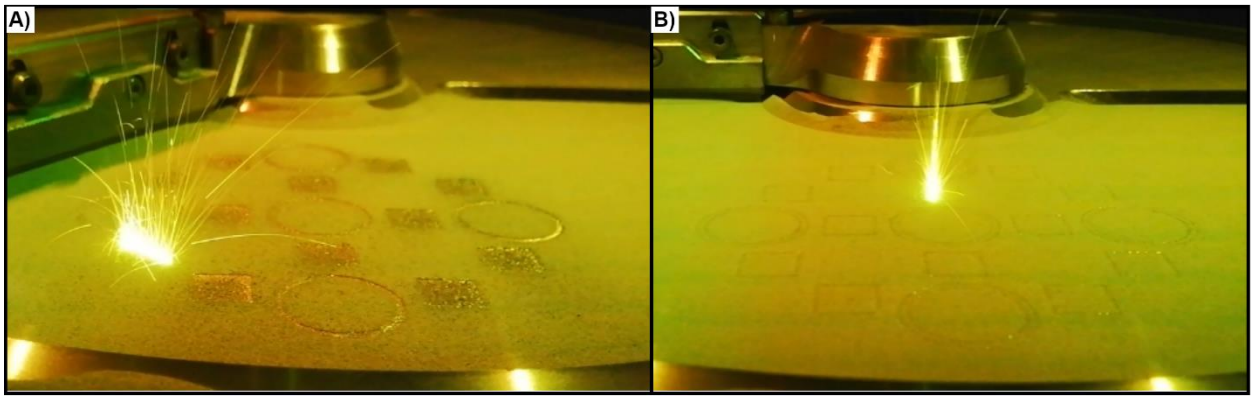

Figure 4-20: Spatter and powder spreading of Deloro powder at a 30 µm layer thickness

As seen in Figure 4-20, there is spatter that occurs, and if observed closely in Figure 4-20 A), the spatter spreads across the build platform and can be identified by small black speckles on the powder layer. The contouring process discussed above, generating spatter and denudation, can be seen in Figure 4-20 B) as the contours of each shape are observed. Adjacent to the contours, there is less powder available for melting due to denudation. Therefore, the spatter and denudation zones allow for inconsistent powder layers to be generated, thus decreasing the PBD and ultimately negatively affecting the part density.

4.6 Summary

Between the two CoCrMo powders, the Deloro powder was finer with a wider PSD and comprised of more spherical particles. The Deloro powder further exhibited a higher PBD than the Praxair powder at each respective layer thickness. For both powders, a similar trend in PBD was identified, where each powder experienced their highest PBD at the left most region of the build plate closest to the powder reservoir. At regions of the build plate where the powder characteristics varied, the resulting part densities varied, this was more prevalent for the Praxair powder with the Deloro powder producing more consistent part densities across the build plate. An increase in the layer thickness exaggerated the results found for both CoCrMo powders, with an increase resulting in a decrease in PBD and part density. The decreased part densities at larger layer thicknesses also presented wider part density ranges.

CHAPTER 5 – CONCLUSION

In the following chapter, the study's conclusions are provided, along with recommendations for future work also presented.

5.1 Conclusion

This study investigated the effect of extrinsic powder characteristics and layer thickness on part density of selective laser melted CoCrMo parts. Two CoCrMo alloys were investigated across two-layer thicknesses with the same laser energy densities. In order to evaluate the effect of extrinsic powder characteristics on part density, the powder was analysed post-manufacturing using PBD samples that encapsulate powder during the manufacturing process; a real representation of the powder quality across the build platform was established in terms of packing efficiency, particle size, distribution, and circularity. Archimedes' principle was used to evaluate the part density as the concept measures porosity in the entire part; furthermore, the porosity was then evaluated through optical micrography of cross-sectional areas and used as additional validation of the part density results.

The Deloro powder had a finer, wider PSD with more spherical particles of the two powder grades. This resulted in improved powder packing efficiencies, with similar results found by [32], [34], [64]–[66]. The powder characteristics showed to have an influence on the PBD, a trend between both powders at both layer thicknesses was found where the highest PBD recorded was at the left-most region of the build plate closest to the powder reservoir. Jacob et al [32] found similar results for an IN625 powder that decreased in PBD along the recoater direction. For a layer thickness of 25 µm, PBD across the build plate was more consistent compared to the 30 µm layer thickness. It was found that particle size and shape had less of an influence on the PBD at 25 µm compared to 30 µm layer thickness. A contributing factor to this was found to be due to less spatter occurring during the smaller layer thickness resulting in more consistent powder layers. At 30 µm layer thickness, the Praxair powder exhibited the largest PBD variations, with the largest variation shown to be caused mainly by a decrease in particle circularity resulting in poorer packing efficiencies.

From the results, a trend was found where the part density varied in regions of the build plate where the powder characteristics varied. However, between the two powders, the Deloro powder exhibited less part density variations across the build plate. When the layer thickness was increased, these results were exaggerated for both powders, and more porosity was present. Zhang et al. [30] found similar results as an increase in layer thickness resulted in increased porosity formation. There was a correlation between the PBD and the part density variations, and where a decrease in powder packing efficiency was measured, a decrease in part density was

measured. A significant contributor to the decreased packing efficiency was spatter mechanisms, as during manufacturing under a larger layer thickness; the spatter increased and caused greater powder variations across the build plate. The increase in spatter created inconsistent powder particle deposits across the build plate, resulting in varying packing efficiencies. For the smaller 25 µm layer thickness, less part density variation was experienced. This is due to sufficient energy being applied to the powder layer to completely melt the current layer to the previous layer as could be seen in the cross-sections of the cuboid specimens where minimal porosity was observed. With improved powder packing efficiency and sufficient energy, less spatter was generated, and part density was more consistent across the build plate.

Manufacturing with a larger layer thickness results in less manufacturing time; however, lack-of-fusion porosity was observed in the larger 30 µm layer thickness parts. Since the laser energy densities were more compatible to the 25 µm layer thickness where minimal porosity was observed, an increase of the powder volume per layer increased porosity formation.

5.2 Future work and Recommendations

The material investigated was CoCrMo; repeating the work with different materials would increase the understanding of laser-material interaction, and comparison studies could be performed. The SLM machine used in this research had a build platform diameter of 100 mm; further studies could be performed on machines with larger build platforms to investigate if the results are similar or exaggerated due to the build platform area.

This study did not consider the influence of the recoater scraper arm on the powder distribution. It was not considered; however, various SLM machines employ linear recoater systems with different recoater blades. A study should be considered where different powder recoater systems in terms of operating mechanics are considered, and their influence on the powder packing efficiency is investigated.

One of the main reasons for porosity in manufactured parts was spatter; within the SLM machine, the gas flow is responsible for removing by-products of the melting process. For this study, the gas flow was kept constant; therefore, future studies should be performed on the dynamics of how gas flow removes spatter and other by-products from the build platform and how the part consistency across the build plate is influenced.

Since spatter is prevalent in the builds and large spatter agglomerates are sometimes formed, it is recommended that the powder be sieved post-manufacturing to ensure the reusability of the powder is not influenced by irregularly large particles. This study investigated how the part density varied across the build platform; therefore, the build platform area was filled with parts to evaluate the consistency. By filling the build area, the spatter was increased due to an increase in the part

volume being manufactured; thus, if less of the build area is occupied, the effects of spatter are expected to be less, and more repeatable parts are expected.

REFERENCES

[1] G. Spierings, A.B. & Levy, “Comparison of density of stainless steel 316L parts produced with selective laser melting using different powder grades,” *Institue rapid Prod. Dev. irpd, inspire AG*, pp. 342–353, 2009.

[2] L. Haferkamp, A. Spierings, M. Rusch, D. Jermann, M. A. Spurek, and K. Wegener, “Effect of Particle size of monomodal 316L powder on powder layer density in powder bed fusion,” *Prog. Addit. Manuf.*, no. 0123456789, 2020, doi: 10.1007/s40964-020-00152-4.

[3] H. G. Coe and S. Pasebani, “Use of bimodal particle size distribution in selective laser melting of 316L stainless steel,” *J. Manuf. Mater. Process.*, vol. 4, no. 1, 2020, doi: 10.3390/jmmp4010008.

[4] J. P. Choi *et al.*, “Evaluation of powder layer density for the selective laser melting (SLM) process,” *Mater. Trans.*, vol. 58, no. 2, pp. 294–297, 2017, doi: 10.2320/matertrans.M2016364.

[5] A. Averardi, C. Cola, S. E. Zeltmann, and N. Gupta, “Effect of particle size distribution on the packing of powder beds: A critical discussion relevant to additive manufacturing,” *Mater. Today Commun.*, vol. 24, no. January, p. 100964, 2020, doi: 10.1016/j.mtcomm.2020.100964.

[6] S. E. Brika, M. Letenneur, C. A. Dion, and V. Brailovski, “Influence of particle morphology and size distribution on the powder flowability and laser powder bed fusion manufacturability of Ti-6Al-4V alloy,” *Addit. Manuf.*, vol. 31, no. November 2019, p. 100929, 2020, doi: 10.1016/j.addma.2019.100929.

[7] A. Y. M. Alfaify, “The Effect of Changing Particle Size Distribution and Layer Thickness on the Density of Parts Manufactured Using the Laser Powder Bed Fusion Process,” The University of Sheffield, 2019.

[8] S. A. Farzadfar, M. J. Murtagh, and N. Venugopal, “Impact of IN718 bimodal powder size distribution on the performance and productivity of laser powder bed fusion additive manufacturing process,” *Powder Technol.*, vol. 375, pp. 60–80, 2020, doi: 10.1016/j.powtec.2020.07.092.

[9] S. Vock, B. Klöden, A. Kirchner, T. Weißgärber, and B. Kieback, “Powders for powder bed fusion: a review,” *Prog. Addit. Manuf.*, vol. 4, no. 4, pp. 383–397, 2019, doi: 10.1007/s40964-019-00078-6.

[10] S. A. Adekanye, R. M. Mahamood, E. T. Akinlabi, and M. G. Owolabi, “Additive manufacturing: The future of manufacturing: Dodajalna (3D) Tehnologija: Prihodnost Proizvajanja,” *Mater. Tehnol.*, vol. 51, no. 5, pp. 709–715, 2017, doi: 10.17222/mit.2016.261.

[11] T. Pereira, J. V. Kennedy, and J. Potgieter, “A comparison of traditional manufacturing vs additive manufacturing, the best method for the job,” *Procedia Manuf.*, vol. 30, pp. 11–18, 2019, doi: 10.1016/j.promfg.2019.02.003.

[12] J. Scott and P. Leader, “Additive Manufacturing : Status and Opportunities Additive Manufacturing : Status and Opportunities,” no. January 2012, 2017, [Online]. Available: https://www.researchgate.net/publication/312153354.

[13] D. Dev Singh, T. Mahender, and A. Raji Reddy, “Powder bed fusion process: A brief review,” *Mater. Today Proc.*, vol. 46, pp. 350–355, 2021, doi: 10.1016/j.matpr.2020.08.415.

[14] I. Gibson, D. Rosen, and B. Stucker, “Powder bed fusion processes,” in *Additive manufacturing technologies*, Springer, 2015, pp. 107–145.

[15] K. Monroy, J. Delgado, and J. Ciurana, “Study of the pore formation on CoCrMo alloys by selective laser melting manufacturing process,” *Procedia Eng.*, vol. 63, pp. 361–369, 2013, doi: 10.1016/j.proeng.2013.08.227.

[16] P. Wang, L. Deng, K. G. Prashanth, S. Pauly, J. Eckert, and S. Scudino, “Microstructure and mechanical properties of Al-Cu alloys fabricated by selective laser melting of powder mixtures,” *J. Alloys Compd.*, vol. 735, pp. 2263–2266, 2018.

[17] M. Revilla-León, M. Sadeghpour, and M. Özcan, “A Review of the Applications of Additive Manufacturing Technologies Used to Fabricate Metals in Implant Dentistry,” *J. Prosthodont.*, vol. 29, no. 7, pp. 579–593, 2020, doi: 10.1111/jopr.13212.

[18] N. T. Aboulkhair, N. M. Everitt, I. Ashcroft, and C. Tuck, “Reducing porosity in AlSi10Mg parts processed by selective laser melting,” *Addit. Manuf.*, vol. 1, pp. 77–86, 2014, doi: 10.1016/j.addma.2014.08.001.
[19] D. Herzog, V. Seyda, E. Wycisk, and C. Emmelmann, “Additive manufacturing of metals,” *Acta Mater.*, vol. 117, pp. 371–392, 2016, doi: 10.1016/j.actamat.2016.07.019.
[20] C. Y. Yap *et al.*, “Review of selective laser melting: Materials and applications,” *Appl. Phys. Rev.*, vol. 2, no. 4, 2015, doi: 10.1063/1.4935926.
[21] E. Cox, “A Method of Assigning Numerical and Percentage Values to the degree of Roundness of Sand Grains,” *J. Paleontol.*, vol. 1, no. 3, pp. 179–183, 1927, [Online]. Available: https://www.jstor.org/stable/1298056.
[22] P. Schneiderhöhn, “Eine vergleichende Studie über Methoden zur quantitativen Bestimmung von Abrundung und Form an Sandkörnern (Im Hinblick auf die Verwendbarkeit an Dünnschliffen.),” *Heidelberger Beiträge zur Mineral. und Petrogr.*, vol. 4, no. 1, pp. 172–191, 1954.
[23] V. Mikli, P. Kulu, H. Käerdi, and M. Besterci, “Characterization of Powder Particle Morphology,” *Proc. Est. Acad. Sci. Eng.*, vol. 7, no. 1, pp. 22–34, 2001, doi: 10.3176/eng.2001.1.03.
[24] C. Wentworth, “Method of Measuring and Plotting the Shapes of Pebbles,” *U.S. Geol. Surv. Bull.*, vol. 39, pp. 91–114, 1922, [Online]. Available: http://pubs.usgs.gov/bul/0730c/report.pdf.
[25] A. T. Sutton, C. S. Kriewall, M. C. Leu, and J. W. Newkirk, “Powder characterisation techniques and effects of powder characteristics on part properties in powder-bed fusion processes,” *Virtual Phys. Prototyp.*, vol. 12, no. 1, pp. 3–29, 2017, doi: 10.1080/17452759.2016.1250605.
[26] J. H. Tan, W. L. E. Wong, and K. W. Dalgarno, “An overview of powder granulometry on feedstock and part performance in the selective laser melting process,” *Addit. Manuf.*, vol. 18, pp. 228–255, 2017, doi: 10.1016/j.addma.2017.10.011.
[27] P. Karapatis, “A sub-process approach of selective laser sintering,” EPFL, 2002.
[28] G. Jacob, A. Donmez, J. Slotwinski, and S. Moylan, “Measurement of powder bed density in powder bed fusion additive manufacturing processes,” *Meas. Sci. Technol.*, vol. 27, no. 11, 2016, doi: 10.1088/0957-0233/27/11/115601.
[29] K. Abd-Elghany and D. L. Bourell, “Property evaluation of 304L stainless steel fabricated by selective laser melting,” *Rapid Prototyp. J.*, vol. 18, no. 5, pp. 420–428, 2012, doi: 10.1108/13552541211250418.
[30] M. Zhang *et al.*, “Competing influence of porosity and microstructure on the fatigue property of laser powder bed fusion stainless steel 316L,” *Solid Free. Fabr. 2017 Proc. 28th Annu. Int. Solid Free. Fabr. Symp. - An Addit. Manuf. Conf. SFF 2017*, pp. 365–376, 2020.
[31] T. M. Wischeropp, C. Emmelmann, M. Brandt, and A. Pateras, “Measurement of actual powder layer height and packing density in a single layer in selective laser melting,” *Addit. Manuf.*, vol. 28, no. March, pp. 176–183, 2019, doi: 10.1016/j.addma.2019.04.019.
[32] G. Jacob, C. U. Brown, and A. Donmez, “The Influence of Spreading Metal Powders with Different Particle Size Distributions on the Powder Bed Density in Laser-Based Powder Bed Fusion Processes,” *NIST Adv. Manuf. Ser. 100-17*, 2018, [Online]. Available: https://doi.org/10.6028/NIST.AMS.100-17.
[33] A. B. Spierings, M. Schneider, and R. Eggenberger, “Comparison of density measurement techniques for additive manufactured metallic parts,” *Rapid Prototyp. J.*, vol. 17, no. 5, pp. 380–386, 2011, doi: 10.1108/13552541111156504.
[34] R. H. Bochuan Liu, Ricky Wildman, Christopher Tuck, Ian Ashcroft, “Investigation the Effect of Particle Size Distribution on Processing Parameters Optimisation in Selective Laser Melting Process,” *Addit. Manuf. Res. group, Loughbrgh. Univ.*, no. mm, pp. 227--238, 2011.
[35] A. Sola and A. Nouri, “Microstructural porosity in additive manufacturing: The formation and detection of pores in metal parts fabricated by powder bed fusion,” *J. Adv. Manuf. Process.*, vol. 1, no. 3, pp. 1–21, 2019, doi: 10.1002/amp2.10021.
[36] C. Weingarten, D. Buchbinder, N. Pirch, W. Meiners, K. Wissenbach, and R. Poprawe, “Formation and reduction of hydrogen porosity during selective laser melting of AlSi10Mg,” *J. Mater. Process. Technol.*, vol. 221, pp. 112–120, 2015, doi:

10.1016/j.jmatprotec.2015.02.013.
[37] H. Choo *et al.*, “Effect of laser power on defect, texture, and microstructure of a laser powder bed fusion processed 316L stainless steel,” *Mater. Des.*, vol. 164, p. 107534, 2019, doi: 10.1016/j.matdes.2018.12.006.
[38] B. M. Morrow *et al.*, “Impact of Defects in Powder Feedstock Materials on Microstructure of 304L and 316L Stainless Steel Produced by Additive Manufacturing,” *Metall. Mater. Trans. A Phys. Metall. Mater. Sci.*, vol. 49, no. 8, pp. 3637–3650, 2018, doi: 10.1007/s11661-018-4661-9.
[39] M. Iebba *et al.*, “Influence of Powder Characteristics on Formation of Porosity in Additive Manufacturing of Ti-6Al-4V Components,” *J. Mater. Eng. Perform.*, vol. 26, no. 8, pp. 4138–4147, 2017, doi: 10.1007/s11665-017-2796-2.
[40] F. H. Kim, S. P. Moylan, E. J. Garboczi, and J. A. Slotwinski, “Investigation of pore structure in cobalt chrome additively manufactured parts using X-ray computed tomography and three-dimensional image analysis,” *Addit. Manuf.*, vol. 17, pp. 23–38, 2017, doi: 10.1016/j.addma.2017.06.011.
[41] K. V. Yang, P. Rometsch, C. H. J. Davies, A. Huang, and X. Wu, “Effect of heat treatment on the microstructure and anisotropy in mechanical properties of A357 alloy produced by selective laser melting,” *Mater. Des.*, vol. 154, pp. 275–290, 2018, doi: 10.1016/j.matdes.2018.05.026.
[42] K. V. Yang *et al.*, “Porosity formation mechanisms and fatigue response in Al-Si-Mg alloys made by selective laser melting,” *Mater. Sci. Eng. A*, vol. 712, no. September 2017, pp. 166–174, 2018, doi: 10.1016/j.msea.2017.11.078.
[43] C. Qiu, C. Panwisawas, M. Ward, H. C. Basoalto, J. W. Brooks, and M. M. Attallah, “On the role of melt flow into the surface structure and porosity development during selective laser melting,” *Acta Mater.*, vol. 96, pp. 72–79, 2015, doi: 10.1016/j.actamat.2015.06.004.
[44] T. Voisin *et al.*, “Defects-dictated tensile properties of selective laser melted Ti-6Al-4V,” *Mater. Des.*, vol. 158, pp. 113–126, 2018, doi: 10.1016/j.matdes.2018.08.004.
[45] T. Vilaro, C. Colin, and J.-D. Bartout, “As-fabricated and heat-treated microstructures of the Ti-6Al-4V alloy processed by selective laser melting,” *Metall. Mater. Trans. A*, vol. 42, no. 10, pp. 3190–3199, 2011.
[46] J. N. Domfang Ngnekou, Y. Nadot, G. Henaff, J. Nicolai, and L. Ridosz, “Influence of defect size on the fatigue resistance of AlSi10Mg alloy elaborated by selective laser melting (SLM),” *Procedia Struct. Integr.*, vol. 7, pp. 75–83, 2017, doi: 10.1016/j.prostr.2017.11.063.
[47] H. Gong, K. Rafi, H. Gu, G. D. Janaki Ram, T. Starr, and B. Stucker, “Influence of defects on mechanical properties of Ti-6Al-4V components produced by selective laser melting and electron beam melting,” *Mater. Des.*, vol. 86, pp. 545–554, 2015, doi: 10.1016/j.matdes.2015.07.147.
[48] L. Thijs, F. Verhaeghe, T. Craeghs, J. Van Humbeeck, and J.-P. Kruth, “A study of the microstructural evolution during selective laser melting of Ti–6Al–4V,” *Acta Mater.*, vol. 58, no. 9, pp. 3303–3312, 2010.
[49] S. A. Khairallah, A. T. Anderson, A. Rubenchik, and W. E. King, “Laser powder-bed fusion additive manufacturing: Physics of complex melt flow and formation mechanisms of pores, spatter, and denudation zones,” *Acta Mater.*, vol. 108, pp. 36–45, 2016, doi: 10.1016/j.actamat.2016.02.014.
[50] W. E. King *et al.*, “Observation of keyhole-mode laser melting in laser powder-bed fusion additive manufacturing,” *J. Mater. Process. Technol.*, vol. 214, no. 12, pp. 2915–2925, 2014, doi: 10.1016/j.jmatprotec.2014.06.005.
[51] L. Thijs, K. Kempen, J. P. Kruth, and J. Van Humbeeck, “Fine-structured aluminium products with controllable texture by selective laser melting of pre-alloyed AlSi10Mg powder,” *Acta Mater.*, vol. 61, no. 5, pp. 1809–1819, 2013, doi: 10.1016/j.actamat.2012.11.052.
[52] L. Sheridan, O. E. Scott-Emuakpor, T. George, and J. E. Gockel, “Relating porosity to fatigue failure in additively manufactured alloy 718,” *Mater. Sci. Eng. A*, vol. 727, no. March, pp. 170–176, 2018, doi: 10.1016/j.msea.2018.04.075.
[53] S. Shrestha, T. Starr, and K. Chou, “Porosity analysis in metal additive manufacturing by micro-ct,” in *Asme international mechanical engineering congress and exposition*, 2018,

vol. 52019, pp. 89–95.
[54] H. Gong, K. Rafi, H. Gu, T. Starr, and B. Stucker, “Analysis of defect generation in Ti-6Al-4V parts made using powder bed fusion additive manufacturing processes,” *Addit. Manuf.*, vol. 1, pp. 87–98, 2014, doi: 10.1016/j.addma.2014.08.002.
[55] A. A. Martin *et al.*, “Dynamics of pore formation during laser powder bed fusion additive manufacturing,” *Nat. Commun.*, vol. 10, no. 1, pp. 1–10, 2019, doi: 10.1038/s41467-019-10009-2.
[56] D. Gu *et al.*, “Densification behavior, microstructure evolution, and wear performance of selective laser melting processed commercially pure titanium,” *Acta Mater.*, vol. 60, no. 9, pp. 3849–3860, 2012, doi: 10.1016/j.actamat.2012.04.006.
[57] D. Wang *et al.*, “Mechanisms and characteristics of spatter generation in SLM processing and its effect on the properties,” *Mater. Des.*, vol. 117, pp. 121–130, 2017, doi: 10.1016/j.matdes.2016.12.060.
[58] S. Pal *et al.*, “The effects of locations on the build tray on the quality of specimens in powder bed additive manufacturing,” *Int. J. Adv. Manuf. Technol.*, vol. 112, no. 3–4, pp. 1159–1170, 2021, doi: 10.1007/s00170-020-06563-5.
[59] A. B. Spierings, N. Herres, and G. Levy, “Influence of the particle size distribution on surface quality and mechanical properties in AM steel parts,” *Rapid Prototyp. J.*, vol. 17, no. 3, pp. 195–202, 2011, doi: 10.1108/13552541111124770.
[60] P. A. Kuznetsov, I. V. Shakirov, A. S. Zukov, V. V. Bobyr’, and M. V. Starytsin, “Effect of particle size distribution on the structure and mechanical properties in the process of laser powder bed fusion,” *J. Phys. Conf. Ser.*, vol. 1758, no. 1, 2021, doi: 10.1088/1742-6596/1758/1/012021.
[61] K. Riener *et al.*, “Influence of particle size distribution and morphology on the properties of the powder feedstock as well as of AlSi10Mg parts produced by laser powder bed fusion (LPBF),” *Addit. Manuf.*, vol. 34, no. February, p. 101286, 2020, doi: 10.1016/j.addma.2020.101286.
[62] L. Hitzler *et al.*, “Additive manufacturing of cobalt-based dental alloys: Analysis of microstructure and physicomechanical properties,” *Adv. Mater. Sci. Eng.*, vol. 2018, 2018, doi: 10.1155/2018/8213023.
[63] J. H. Wang, J. Ren, W. Liu, X. Y. Wu, M. X. Gao, and P. K. Bai, “Effect of selective laser melting process parameters on microstructure and properties of co-cr alloy,” *Materials (Basel).*, vol. 11, no. 9, 2018, doi: 10.3390/ma11091546.
[64] D. Geldart, E. C. Abdullah, A. Hassanpour, L. C. Nwoke, and I. Wouters, “CHARACTERIZATION OF POWDER FLOWABILITY USING MEASUREMENT OF ANGLE OF REPOSE,” vol. 4, no. 1990, pp. 104–107, 2006.
[65] B. Vrancken, L. Thijs, J. Kruth, and J. Van Humbeeck, “ScienceDirect Microstructure and mechanical properties of a novel b titanium metallic composite by selective laser melting,” *Acta Mater.*, vol. 68, pp. 150–158, 2014, doi: 10.1016/j.actamat.2014.01.018.
[66] M. Boisvert, D. Christopherson, P. Beaulieu, and G. L. Espérance, “Treatment of ferrous melts for the improvement of the sphericity of water atomized powders,” *Mater. Des.*, vol. 116, pp. 644–655, 2017, doi: 10.1016/j.matdes.2016.12.059.
[67] C. Pleass and S. Jothi, “Influence of powder characteristics and additive manufacturing process parameters on the microstructure and mechanical behaviour of Inconel 625 fabricated by Selective Laser Melting,” *Addit. Manuf.*, vol. 24, no. September, pp. 419–431, 2018, doi: 10.1016/j.addma.2018.09.023.
[68] V. S. Sufiiarov, A. A. Popovich, E. V. Borisov, I. A. Polozov, D. V. Masaylo, and A. V. Orlov, “The Effect of Layer Thickness at Selective Laser Melting,” *Procedia Eng.*, vol. 174, pp. 126–134, 2017, doi: 10.1016/j.proeng.2017.01.179.
[69] Micrometrics Instrument Corporation, “AccuPyc II 1340,” no. July. Micrometrics Instrument Corporation, 2007, [Online]. Available: https://www.micromeritics.com/Repository/Files/AccuPyc_II_1340_Operator_Manual_Keypad_Version_V1.03.pdf.
[70] Malvern Panalytical, “Morphologi G3 User Guide,” *Morphologi G3 User Guide*, 2021. https://www.malvernpanalytical.com/en/learn/knowledge-center/user-manuals/MAN0493EN.

[71] FEI, “FEI Quanta 250 FEG,” 2009. https://www.biotech.iastate.edu/wp_single/wp-content/uploads/2012/01/quanta.pdf (accessed Aug. 22, 2022).
[72] Coherent ORLASER, “3D Metal Printing of Tomorrow - OR LASER CREATOR.” https://www.google.com/url?sa=i&url=https%3A%2F%2Ff.nordiskemedier.dk%2F2tyi3f0yctp30g3a.pdf&psig=AOvVaw2wxyoomQ9GfL4WKN4Az9Uu&ust=1654155593182000&source=images&cd=vfe&ved=0CA4Q3YkBahcKEwjYy4r934v4AhUAAAAAHQAAAAAQDg (accessed Jun. 01, 2022).
[73] ASTM B311-17., “Standard Test Method for Density of Powder Metallurgy (PM) Materials Containing Less Than Two Percent Porosity,” *ASTM Int.*, vol. i, pp. 1–5, 2017, doi: 10.1520/B0311-17.2.
[74] AKASEL, “Aka-Brief # 18 Surface Hardened Steel.” AKASEL, 2021.
[75] H. Gu *et al.*, “Effects of powder variation on the microstructure and tensile strength of Ti6Al4V parts fabricated by selective laser melting,” *25th Annu. Int. Solid Free. Fabr. Symp. &#65533; An Addit. Manuf. Conf. SFF 2014*, pp. 470–483, 2014.

APPENDIX A – RESULTANT RELATIVE DENSITY FOR THE BUILDS USED TO EVALUATE DENSITY VARIATIONS ACROSS THE BUILD PLATE

The tables used in the following sections show the results of the Archimedes density tests used to measure the relative density and evaluate the part density variations across the build plate.

Table A-1: Part density results of each cuboid specimen for Praxair 25 µm layer thickness

Density Cube	Measurement Media	Test #			Avg. Mass	St. Dev	Density	Relative Density
		1	2	3	[g]	[-]	[g/ cm^3]	[%]
1	Air	7,710	7,710	7,709	7,709	9,43E-05	8,350	99,83%
	Water	6,788	6,788	6,788	6,788	4,71E-05		
2	Air	7,766	7,766	7,767	7,766	1,25E-04	8,360	99,95%
	Water	6,839	6,839	6,839	6,839	4,71E-05		
3	Air	7,897	7,897	7,897	7,897	4,71E-05	8,334	99,64%
	Water	6,951	6,951	6,951	6,951	4,71E-05		
4	Air	7,838	7,838	7,838	7,838	4,71E-05	8,364	100,00%
	Water	6,902	6,902	6,902	6,902	1,25E-04		
5	Air	7,700	7,700	7,700	7,700	1,25E-04	8,357	99,92%
	Water	6,781	6,781	6,780	6,781	1,25E-04		
6	Air	7,721	7,721	7,721	7,721	4,71E-05	8,357	99,91%
	Water	6,799	6,799	6,799	6,799	1,41E-04		
7	Air	7,902	7,902	7,902	7,902	4,71E-05	8,370	100,06%
	Water	6,960	6,960	6,960	6,960	4,71E-05		
8	Air	8,021	8,021	8,021	8,021	4,71E-05	8,368	100,04%
	Water	7,064	7,064	7,064	7,064	1,25E-04		
9	Air	8,119	8,119	8,119	8,119	4,71E-05	8,356	99,90%
	Water	7,149	7,149	7,149	7,149	9,43E-05		
10	Air	8,055	8,055	8,055	8,055	4,71E-05	8,359	99,93%
	Water	7,093	7,093	7,093	7,093	4,71E-05		
11	Air	7,914	7,914	7,914	7,914	4,71E-05	8,365	100,00%
	Water	6,970	6,970	6,970	6,970	8,16E-05		
12	Air	7,869	7,868	7,868	7,868	4,71E-05	8,363	99,99%
	Water	6,929	6,929	6,929	6,929	9,43E-05		

Table A-2: Part density results of each cuboid specimen for Praxair 30 µm layer thickness

Density Cube	Measurement Media	Test #			Avg. Mass	St. Dev	Density	Relative Density
		1	2	3	[g]	[-]	[g/ cm^3]	[%]
1	Air	7,792	7,792	7,792	7,792	8,88E-16	8,283	99,03%
	Water	6,853	6,853	6,853	6,853	1,70E-04		
2	Air	7,636	7,636	7,636	7,636	4,71E-05	8,305	99,29%
	Water	6,718	6,718	6,718	6,718	8,16E-05		
3	Air	7,648	7,649	7,649	7,648	4,71E-05	8,296	99,19%
	Water	6,728	6,728	6,728	6,728	9,43E-05		
4	Air	7,829	7,829	7,829	7,829	4,71E-05	8,307	99,31%
	Water	6,888	6,888	6,888	6,888	8,16E-05		
5	Air	7,776	7,776	7,776	7,776	4,71E-05	8,255	98,70%
	Water	6,836	6,836	6,836	6,836	0,00E+00		
6	Air	7,678	7,678	7,678	7,678	8,16E-05	8,277	98,96%
	Water	6,752	6,752	6,752	6,752	4,71E-05		
7	Air	7,548	7,548	7,548	7,548	4,71E-05	8,304	99,28%
	Water	6,641	6,641	6,641	6,641	0,00E+00		
8	Air	7,603	7,603	7,603	7,603	0,00E+00	8,321	99,49%
	Water	6,691	6,691	6,691	6,691	1,25E-04		
9	Air	7,830	7,830	7,830	7,830	4,71E-05	8,321	99,49%
	Water	6,891	6,891	6,890	6,890	4,71E-05		
10	Air	7,901	7,901	7,901	7,901	8,16E-05	8,300	99,22%
	Water	6,951	6,951	6,951	6,951	4,71E-05		
11	Air	8,104	8,104	8,104	8,104	4,71E-05	8,281	99,01%
	Water	7,127	7,127	7,127	7,127	9,43E-05		
12	Air	8,094	8,094	8,094	8,094	4,71E-05	8,284	99,04%
	Water	7,118	7,118	7,118	7,118	4,71E-05		

Table A-3: Part density results of each cuboid specimen for Deloro 25 µm layer thickness

Density Cube	Measurement Media	Test #			Avg. Mass	St. Dev	Density	Relative Density
		1	2	3	[g]	[-]	[g/ cm³]	[%]
1	Air	8,244	8,244	8,244	8,244	4,71E-05	8,265	99,22%
	Water	7,247	7,248	7,248	7,248	2,16E-04		
2	Air	8,082	8,082	8,082	8,082	4,71E-05	8,272	99,31%
	Water	7,106	7,107	7,106	7,106	2,16E-04		
3	Air	8,113	8,113	8,113	8,113	8,16E-05	8,257	99,14%
	Water	7,132	7,132	7,132	7,132	9,43E-05		
4	Air	8,257	8,257	8,256	8,256	1,89E-04	8,260	99,16%
	Water	7,258	7,259	7,258	7,258	1,70E-04		
5	Air	8,266	8,266	8,266	8,266	8,16E-05	8,255	99,11%
	Water	7,266	7,266	7,266	7,266	1,70E-04		
6	Air	8,156	8,156	8,156	8,156	8,16E-05	8,260	99,17%
	Water	7,170	7,170	7,170	7,170	8,16E-05		
7	Air	8,059	8,059	8,059	8,059	4,71E-05	8,259	99,15%
	Water	7,085	7,085	7,085	7,085	4,71E-05		
8	Air	8,110	8,110	8,110	8,110	4,71E-05	8,262	99,19%
	Water	7,130	7,129	7,130	7,130	1,25E-04		
9	Air	8,286	8,286	8,286	8,286	4,71E-05	8,259	99,16%
	Water	7,285	7,284	7,284	7,284	9,43E-05		
10	Air	8,390	8,390	8,390	8,390	4,71E-05	8,267	99,25%
	Water	7,377	7,376	7,376	7,376	8,16E-05		
11	Air	8,548	8,548	8,548	8,548	8,16E-05	8,272	99,31%
	Water	7,516	7,516	7,516	7,516	1,70E-04		
12	Air	8,521	8,521	8,521	8,521	4,71E-05	8,272	99,32%
	Water	7,493	7,493	7,493	7,493	1,89E-04		

Table A-4: Part density results of each cuboid specimen for Deloro 30 µm layer thickness

Density Cube	Measurement Media	Test #			Avg. Mass	St. Dev	Density	Relative Density
		1	2	3	[g]	[-]	[g/ cm^3]	[%]
1	Air	7,839	7,839	7,839	7,839	8,88E-16	8,229	98,79%
	Water	6,888	6,888	6,888	6,888	4,71E-05		
2	Air	7,998	7,998	7,998	7,998	4,71E-05	8,218	98,67%
	Water	7,026	7,027	7,027	7,027	1,70E-04		
3	Air	7,579	7,579	7,579	7,579	0,00E+00	8,225	98,75%
	Water	6,659	6,659	6,659	6,659	8,16E-05		
4	Air	7,689	7,689	7,689	7,689	8,16E-05	8,244	98,97%
	Water	6,758	6,758	6,758	6,758	1,63E-04		
5	Air	8,046	8,046	8,046	8,046	1,25E-04	8,221	98,70%
	Water	7,069	7,069	7,069	7,069	2,05E-04		
6	Air	8,115	8,115	8,115	8,115	1,25E-04	8,230	98,80%
	Water	7,130	7,130	7,131	7,131	2,16E-04		
7	Air	8,191	8,191	8,191	8,191	8,16E-05	8,212	98,59%
	Water	7,195	7,196	7,195	7,195	1,63E-04		
8	Air	8,223	8,223	8,223	8,223	1,25E-04	8,236	98,87%
	Water	7,226	7,226	7,226	7,226	1,25E-04		
9	Air	7,592	7,593	7,593	7,592	1,89E-04	8,250	99,04%
	Water	6,673	6,674	6,674	6,674	1,25E-04		
10	Air	7,684	7,684	7,684	7,684	9,43E-05	8,254	99,09%
	Water	6,755	6,755	6,755	6,755	1,25E-04		
11	Air	7,998	7,998	7,998	7,998	9,43E-05	8,233	98,84%
	Water	7,028	7,028	7,028	7,028	1,41E-04		
12	Air	8,096	8,096	8,096	8,096	0,00E+00	8,239	98,91%
	Water	7,115	7,115	7,115	7,115	8,16E-05		

APPENDIX B – RESULTANT PBD FOR THE BUILDS USED TO EVALUATE PBD VARIATIONS ACROSS THE BUILD PLATE

The tables used in the following sections show the results of the PBD tests used to measure the PBD and evaluate the part density variations across the build plate.

Table A-5: PBD results of each capsule specimen for Praxair 25 µm layer thickness

		Full	Empty	Mass Powder	Mass Container with Water	Mass water	Volume	PBD	
		[g]	[g]	[g]	[g]	[g]	[cm^3]	[g/ cm^3]	[%]
TOP	#1	79,688	50,167	29,521	56,050	5,883	5,892	5,010	59,90%
	#2	79,688	50,168	29,520	56,050	5,883	5,892	5,010	
	#3	79,688	50,167	29,520	56,050	5,883	5,892	5,010	
	Avg.	79,688	50,167	29,520	56,050	5,883	5,892	5,010	
	St. Dev	1,00E-04	1,00E-04	1,73E-04	5,77E-05	1,15E-04	1,16E-04	6,89E-05	
BOTTOM	#1	79,567	50,524	29,043	56,307	5,783	5,792	5,014	59,94%
	#2	79,567	50,524	29,043	56,307	5,783	5,792	5,014	
	#3	79,567	50,523	29,043	56,307	5,783	5,793	5,014	
	Avg.	79,567	50,524	29,043	56,307	5,783	5,792	5,014	
	St. Dev	5,77E-05	1,00E-04	1,53E-04	5,77E-05	1,53E-04	1,53E-04	1,06E-04	
CENTRE	#1	78,033	49,435	28,598	55,120	5,685	5,694	5,022	60,05%
	#2	78,033	49,435	28,598	55,120	5,685	5,694	5,022	
	#3	78,033	49,435	28,598	55,120	5,685	5,694	5,023	
	Avg.	78,033	49,435	28,598	55,120	5,685	5,694	5,023	
	St. Dev	5,77E-05	5,77E-05	4,35E-15	1,00E-04	5,77E-05	5,78E-05	5,10E-05	
LEFT	#1	80,360	50,736	29,624	56,609	5,873	5,882	5,036	60,21%
	#2	80,360	50,736	29,624	56,609	5,873	5,882	5,036	
	#3	80,360	50,736	29,624	56,609	5,873	5,882	5,036	
	Avg.	80,360	50,736	29,624	56,609	5,873	5,882	5,036	
	St. Dev	0,00E+00	0,00E+00	0,00E+00	5,77E-05	5,77E-05	5,78E-05	4,95E-05	
RIGHT	#1	79,239	49,888	29,351	55,733	5,845	5,854	5,014	59,94%
	#2	79,239	49,888	29,351	55,732	5,845	5,854	5,014	
	#3	79,239	49,888	29,351	55,732	5,845	5,854	5,014	
	Avg.	79,239	49,888	29,351	55,732	5,845	5,854	5,014	
	St. Dev	1,15E-04	1,00E-04	5,77E-05	5,77E-05	5,77E-05	5,78E-05	4,54E-05	

Table A-6: PBD results of each capsule specimen for Praxair 30 µm layer thickness

		Full	Empty	Mass Powder	Mass Container with Water	Mass water	Volume	PBD	
		[g]	[g]	[g]	[g]	[g]	[cm³]	[g/ cm³]	[%]
TOP	#1	79,893	50,590	29,303	56,472	5,881	5,891	4,974	59,47%
	#2	79,893	50,590	29,303	56,472	5,881	5,891	4,974	
	#3	79,893	50,590	29,303	56,471	5,881	5,890	4,975	
	Avg.	79,893	50,590	29,303	56,471	5,881	5,891	4,974	
	St. Dev	1,00E-04	1,15E-04	1,53E-04	1,15E-04	2,00E-04	2,00E-04	1,63E-04	
BOTTOM	#1	77,799	48,894	28,905	54,666	5,772	5,781	5,000	59,78%
	#2	77,799	48,894	28,904	54,666	5,771	5,781	5,000	
	#3	77,799	48,894	28,904	54,666	5,771	5,781	5,000	
	Avg.	77,799	48,894	28,904	54,666	5,771	5,781	5,000	
	St. Dev	5,77E-05	1,15E-04	1,00E-04	5,77E-05	1,73E-04	1,73E-04	1,35E-04	
CENTRE	#1	77,331	48,875	28,456	54,552	5,677	5,686	5,004	59,83%
	#2	77,331	48,875	28,456	54,552	5,677	5,686	5,004	
	#3	77,331	48,875	28,456	54,552	5,677	5,686	5,004	
	Avg.	77,331	48,875	28,456	54,552	5,677	5,686	5,004	
	St. Dev	5,77E-05	5,77E-05	5,77E-05	1,00E-04	5,77E-05	5,78E-05	4,67E-05	
LEFT	#1	79,995	50,507	29,489	56,372	5,865	5,874	5,020	60,02%
	#2	79,995	50,507	29,489	56,372	5,865	5,874	5,020	
	#3	79,995	50,507	29,489	56,372	5,865	5,874	5,020	
	Avg.	79,995	50,507	29,489	56,372	5,865	5,874	5,020	
	St. Dev	0,00E+00	5,77E-05	5,77E-05	0,00E+00	5,77E-05	5,78E-05	3,96E-05	
RIGHT	#1	78,111	48,770	29,341	54,610	5,840	5,849	5,016	59,97%
	#2	78,111	48,770	29,341	54,610	5,840	5,849	5,016	
	#3	78,111	48,770	29,341	54,610	5,840	5,849	5,016	
	Avg.	78,111	48,770	29,341	54,610	5,840	5,849	5,016	
	St. Dev	1,00E-04	5,77E-05	5,77E-05	5,77E-05	4,12E-15	4,12E-15	9,87E-06	

Table A-7: PBD results of each capsule specimen for Deloro 25 µm layer thickness

		Full	Empty	Mass Powder	Mass Container with Water	Mass water	Volume	PBD	
		[g]	[g]	[g]	[g]	[g]	[cm^3]	[g/ cm^3]	[%]
TOP	#1	82,545	52,258	30,287	58,122	5,863	5,872	5,158	61,92%
	#2	82,545	52,258	30,287	58,121	5,863	5,872	5,158	
	#3	82,545	52,258	30,287	58,121	5,863	5,872	5,158	
	Avg.	82,545	52,258	30,287	58,121	5,863	5,872	5,158	
	St. Dev	5,77E-05	1,53E-04	1,53E-04	5,77E-05	1,15E-04	1,16E-04	8,37E-05	
BOTTOM	#1	80,776	51,110	29,666	56,864	5,755	5,763	5,147	61,80%
	#2	80,776	51,109	29,666	56,864	5,755	5,763	5,147	
	#3	80,776	51,110	29,666	56,864	5,755	5,763	5,147	
	Avg.	80,776	51,109	29,666	56,864	5,755	5,763	5,147	
	St. Dev	1,15E-04	5,77E-05	1,00E-04	5,77E-05	5,77E-05	5,78E-05	3,76E-05	
CENTRE	#1	80,031	50,817	29,213	56,471	5,653	5,662	5,160	61,95%
	#2	80,031	50,817	29,213	56,471	5,653	5,662	5,160	
	#3	80,031	50,817	29,213	56,471	5,653	5,662	5,160	
	Avg.	80,031	50,817	29,213	56,471	5,653	5,662	5,160	
	St. Dev	5,77E-05	5,77E-05	1,00E-04	0,00E+00	5,77E-05	5,78E-05	3,84E-05	
LEFT	#1	82,893	52,642	30,251	58,481	5,839	5,848	5,173	62,11%
	#2	82,893	52,642	30,251	58,481	5,839	5,848	5,173	
	#3	82,893	52,642	30,251	58,481	5,839	5,848	5,173	
	Avg.	82,893	52,642	30,251	58,481	5,839	5,848	5,173	
	St. Dev	5,77E-05	5,77E-05	5,77E-05	1,15E-04	1,00E-04	1,00E-04	8,02E-05	
RIGHT	#1	81,037	51,026	30,011	56,840	5,815	5,823	5,154	61,87%
	#2	81,037	51,026	30,011	56,840	5,815	5,823	5,154	
	#3	81,037	51,026	30,011	56,840	5,815	5,823	5,154	
	Avg.	81,037	51,026	30,011	56,840	5,815	5,823	5,154	
	St. Dev	1,15E-04	5,77E-05	1,53E-04	1,15E-04	5,77E-05	5,78E-05	7,30E-05	

Table A-8: PBD results of each capsule specimen for Deloro 30 µm layer thickness

		Full	Empty	Mass Powder	Mass Container with Water	Mass water	Volume	PBD	
		[g]	[g]	[g]	[g]	[g]	[cm^3]	[g/cm^3]	[%]
TOP	#1	81,462	51,126	30,336	57,001	5,874	5,883	5,156	61,90%
	#2	81,462	51,127	30,336	57,000	5,874	5,883	5,156	
	#3	81,462	51,126	30,336	57,000	5,874	5,883	5,156	
	Avg.	81,462	51,126	30,336	57,000	5,874	5,883	5,156	
	St. Dev	5,77E-05	5,77E-05	5,77E-05	5,77E-05	1,00E-04	1,00E-04	7,94E-05	
BOTTOM	#1	78,589	48,725	29,863	54,504	5,779	5,788	5,160	61,95%
	#2	78,589	48,725	29,863	54,504	5,779	5,788	5,160	
	#3	78,589	48,725	29,864	54,504	5,779	5,788	5,160	
	Avg.	78,589	48,725	29,863	54,504	5,779	5,788	5,160	
	St. Dev	5,77E-05	1,00E-04	5,77E-05	5,77E-05	1,53E-04	1,53E-04	1,27E-04	
CENTRE	#1	78,286	48,930	29,356	54,601	5,672	5,681	5,168	62,04%
	#2	78,286	48,929	29,356	54,601	5,672	5,681	5,168	
	#3	78,286	48,929	29,357	54,601	5,672	5,681	5,168	
	Avg.	78,286	48,929	29,356	54,601	5,672	5,681	5,168	
	St. Dev	5,77E-05	1,00E-04	1,15E-04	5,77E-05	5,77E-05	5,78E-05	3,23E-05	
LEFT	#1	80,552	50,080	30,472	55,946	5,865	5,875	5,187	62,27%
	#2	80,552	50,080	30,472	55,946	5,865	5,875	5,187	
	#3	80,552	50,080	30,472	55,946	5,865	5,875	5,187	
	Avg.	80,552	50,080	30,472	55,946	5,865	5,875	5,187	
	St. Dev	0,00E+00	5,77E-05	5,77E-05	5,77E-05	1,15E-04	1,16E-04	9,23E-05	
RIGHT	#1	81,332	51,226	30,106	57,057	5,831	5,840	5,155	61,89%
	#2	81,332	51,226	30,107	57,057	5,831	5,840	5,155	
	#3	81,332	51,226	30,107	57,057	5,831	5,840	5,155	
	Avg.	81,332	51,226	30,106	57,057	5,831	5,840	5,155	
	St. Dev	5,77E-05	1,00E-04	1,15E-04	1,15E-04	5,77E-05	5,78E-05	6,33E-05	

APPENDIX C – POWDER SIZE AND SHAPE RESULTS

The following tables show the static automated imaging results for the powder samples gathered from the PBD samples in each build for each powder type.

Table A-9: Powder size and shape results for Praxair 25 µm layer thickness

Praxair 25µm Layer Thickness								
Position	PSD [µm]				Circularity	Aspect Ratio	Elongation	Convexity
	D10	D50	D90	Mean	Mean	Mean	Mean	Mean
Top	6,740	22,473	36,200	22,103	0,909	0,862	0,138	0,986
Centre	13,517	24,373	38,080	25,203	0,895	0,853	0,147	0,980
Bottom	12,537	25,817	39,067	26,247	0,903	0,857	0,143	0,983
Left	8,937	21,090	35,323	22,197	0,907	0,862	0,138	0,985
Right	10,493	21,510	37,240	22,707	0,918	0,871	0,129	0,987
Average	10,445	23,053	37,182	23,691	0,906	0,861	0,139	0,984

Table A-10: Powder size and shape results for Praxair 30 µm layer thickness

Praxair 30 µm Layer Thickness								
Position	PSD [µm]				Circularity	Aspect Ratio	Elongation	Convexity
	D10	D50	D90	Mean	Mean	Mean	Mean	Mean
Top	8,350	22,980	38,970	23,510	0,896	0,849	0,151	0,985
Centre	11,443	22,470	35,713	23,127	0,916	0,870	0,130	0,987
Bottom	15,233	26,747	41,933	28,023	0,900	0,844	0,144	0,982
Left	4,413	18,490	33,390	19,533	0,925	0,873	0,127	0,990
Right	12,097	21,180	33,997	22,263	0,926	0,877	0,123	0,989
Average	10,307	22,373	36,801	23,291	0,912	0,863	0,135	0,987

Table A-11: Powder size and shape results for Deloro 25 µm layer thickness

Deloro 25 µm Layer Thickness								
Position	PSD [µm]				Circularity	Aspect Ratio	Elongation	Convexity
	D10	D50	D90	Mean	Mean	Mean	Mean	Mean
Top	1,037	9,770	22,357	10,530	0,940	0,893	0,107	0,993
Centre	4,540	13,163	27,927	15,350	0,925	0,878	0,122	0,988
Bottom	6,147	14,000	26,870	15,887	0,930	0,878	0,122	0,989
Left	6,690	13,097	25,893	15,117	0,934	0,885	0,115	0,990
Right	7,313	12,930	24,630	14,737	0,938	0,888	0,112	0,991
Average	5,145	12,592	25,535	14,324	0,933	0,885	0,115	0,990

Table A-12: Powder size and shape results for Deloro 30 µm layer thickness

Deloro 30 µm Layer Thickness								
Position	PSD [µm]				Circularity	Aspect Ratio	Elongation	Convexity
	D10	D50	D90	Mean	Mean	Mean	Mean	Mean
Top	6,273	13,527	26,297	15,420	0,929	0,879	0,121	0,989
Centre	3,953	12,073	22,237	13,317	0,939	0,891	0,109	0,991
Bottom	5,723	14,660	29,110	16,520	0,926	0,878	0,122	0,988
Left	7,670	12,583	22,203	14,093	0,937	0,887	0,113	0,990
Right	6,423	13,333	25,480	15,123	0,933	0,884	0,116	0,990
Average	6,009	13,235	25,065	14,895	0,933	0,884	0,116	0,990

APPENDIX D – EFFECTIVE LAYER THICKNESS

The effective layer thickness results calculated per layer were based on the mean relative density and PBD for each build. The layer thickness was calculated for 30 layers to show how the layer stabilises to reach the effective layer thickness as shown in Figure 4-8 based on results from

Table A-13: Development of effective layer thickness

Effective Layer Thickness				
Layer No.	Praxair		Deloro	
	25 µm	30 µm	25 µm	30 µm
1	25	30	25	30
2	34,9805	41,8057	34,31955	41,04772
3	38,96492	46,45151	37,79371	45,11612
4	40,55558	48,27975	39,08882	46,61434
5	41,1906	48,9992	39,57161	47,16607
6	41,44412	49,28232	39,75159	47,36925
7	41,54533	49,39373	39,81868	47,44407
8	41,58573	49,43758	39,84369	47,47162
9	41,60186	49,45483	39,85301	47,48177
10	41,6083	49,46162	39,85649	47,48551
11	41,61087	49,46429	39,85779	47,48688
12	41,6119	49,46535	39,85827	47,48739
13	41,61231	49,46576	39,85845	47,48758
14	41,61247	49,46592	39,85852	47,48765
15	41,61254	49,46599	39,85854	47,48767
16	41,61256	49,46601	39,85855	47,48768
17	41,61257	49,46602	39,85855	47,48768
18	41,61258	49,46603	39,85856	47,48769
19	41,61258	49,46603	39,85856	47,48769
20	41,61258	49,46603	39,85856	47,48769
21	41,61258	49,46603	39,85856	47,48769
22	41,61258	49,46603	39,85856	47,48769
23	41,61258	49,46603	39,85856	47,48769
24	41,61258	49,46603	39,85856	47,48769
25	41,61258	49,46603	39,85856	47,48769
26	41,61258	49,46603	39,85856	47,48769
27	41,61258	49,46603	39,85856	47,48769
28	41,61258	49,46603	39,85856	47,48769
29	41,61258	49,46603	39,85856	47,48769
30	41,61258	49,46603	39,85856	47,48769

APPENDIX E – MATLAB CODE USED TO GENERATE COLOUR MAPS

The MATLAB code shown below was used for plotting the colour maps presented in the results Chapter 4. For the code shown below, values E1 - E12 represented the relative part density difference in cuboid specimens for the Praxair 25 µm layer thickness. The same code was used for all plots with the only difference being the input values.

```
% Density Difference Plot for Praxair 25um LT


[xq, yq] = meshgrid (0:0.1:100,0:0.1:100);


E1 = 0.23
E2 = 0.12
E3 = 0.42
E4 = 0.06
E5 = 0.15
E6 = 0.15
E7 = 0
E8 = 0.02
E9 = 0.17
E10 = 0.13
E11 = 0.06
E12 = 0.07


tiledlayout(1,1)
nexttile
vq_7 =
griddata(DD25_Praxair(:,2),DD25_Praxair(:,3),DD25_Praxair(:,4),xq,yq,"cubic");
DD_25_Praxair = meshc(xq,yq,vq_7);
title ("Density Difference {25\it\mum}")
zlabel ('Change in Density [%]')
ylabel ('y [mm]')
xlabel ('x [mm]')


lighting 'phong'
colormap jet
caxis manual
caxis([0 1]);
c = colorbar;
c.Label.String = '\Delta Density [%]';
legend ('Relative Density','Contour')
hold off
```